Assembly of highly-ordered structures for nanosphere lithography

Master Thesis in Nanobiotechnology

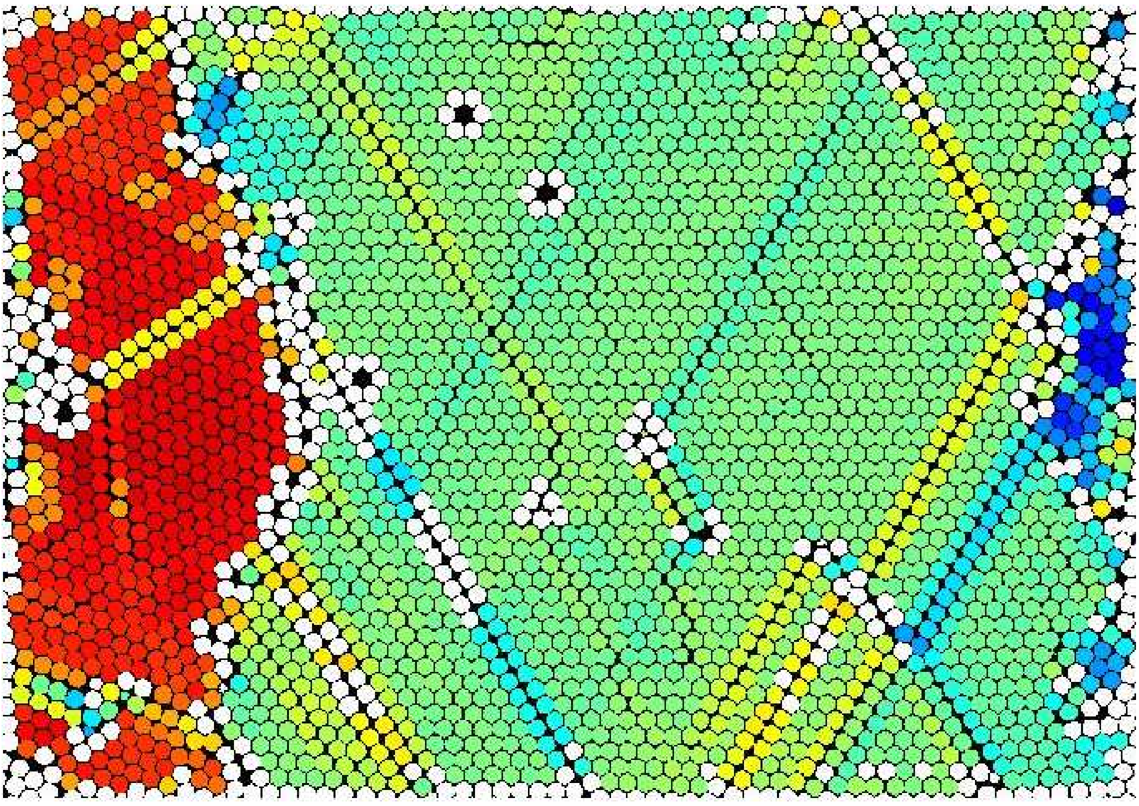

Sergio Fernández Martínez
Aalborg University
July 2016

AALBORG UNIVERSITY
STUDENT REPORT

Institute of Physics and Nanotechnology
Skjernvej 4A, 9220 Aalborg Ost, Denmark
Phone +45 99 40 92 15, Fax +45 99 40 92 35
http://www.nano.aau.dk/

Title:

Assembly of highly-ordered structures for nanosphere lithography

Project period:

September 15th 2015 to
January 15th 2016

Author:

Sergio Fernández Martínez

Supervisors:

Leonid Gurevich
Peter Fojan

Circulation: 3

Number of pages: 133 (141)

Completed: July 15th 2016

Abstract:

Nanosphere lithography has attracted the attention of researches as an alternative for the high equipment costs of conventional lithography by the combination of bottom-up and bottom-down approaches. The high throughput and large-area fabrication depend on the self-assembled monolayer which acts as a colloidal mask. For this reason, the aim of this thesis is to explore different methods for preparation of a colloidal crystal monolayer made of nano-and microspheres.

Self-assembled monolayers of silica nanospheres via Droplet evaporation were not successfully formed in neither hydrophobic nor hydrophilic substrates. The aggregation forces were dominant during the arrangement process with an insufficient lateral capillary force to enhance order.

On the contrary, polystyrene particles via Droplet method displayed large areas of hexagonal close-packing together with vacancies and defect lines. Dip-coating method also provided highly-ordered monolayers regarding the arrangement extension with a strong influence in the suspension concentration, solvents and withdrawal speed indicating that coating conditions could be further optimized. The monolayers formed at the air/water interface via Langmuir-Blodgett method resulted in better order for micro-polystyrene particles with domains of hexagonal packing as well as line defects. The main drawbacks were the compression stability during monolayer transfer and the material loss into the subphase influenced by the dispersion solvent and the hydrophilicity of the poly(acrylic acid) grafted on the polystyrene surface.

Preface

This report is written by a nanobiotechnology student at Aalborg University, during the fourth semester of master in nanobiotechnology period running from September 15th of 2015 to January 15th of 2016. The experimental work has been performed in the Department of Physics and Nanotechnology.

The report is divided in chapters and sections. The first chapter is the Introduction where the theoretical part provides a global insight of the concepts developed throughout the report. The second chapter describes the material and methods used for the experiments and assays while the third chapter presents the results obtained from the experimental work. The fourth chapter discusses and analyzes the results obtained connecting them with the theoretical expectations and with the previous work done on the subject. The last chapter is the conclusion arrived at in the project.

References to sources within the text are written as follow: [1], where the number refers to the specific source in the bibliography. Each source listed in the bibliography includes the authors, the title, and other information of interest depending on whether the source is a book, article or webpage. The reference placed in a specific section immediately after a paragraph applies to all of the text above and when placed after a sentence applies to all of the text above including the sentence itself. References to figures, tables and equations are written such as: figure 1.1, where figure, table or equation refers to the type, the first digit refers to the chapter where the figure, table or equation is shown and the second digit refers to the counting number used to identified successive figures, tables or equations within a specific chapter. Figures and tables are clarified by a descriptive caption together with a reference when necessary. A PDF version of the report including all figures is found on the attached DVD.

Abbreviations

AFM = Atomic Force Microscopy
DL PPA = Double layer periodic particle array
DLVO = Derjaguin-Landau-Verwey-Overbeek
fcc = face-centered cubic
hcp = hexagonal close-packed
LB = Langmuir-Blodgett
NTA = Nanoparticle Tracking Analysis
PAA = poly(acrylic acid)
PS_2 = Polystyrene particles with diameter of ~2µm
PS_{350} = Polystyrene particles with diameter of ~350nm
SAM = Self-Assembled Monolayer
SEM = Scanning Electron Microscopy
SL PPA = Single layer periodic particle array cubic
vdW = van der Waals
2D = Two-dimensional space

Contents

1 Introduction 1

1 Introduction

Nanoscience and nanoengineering has led to the fabrication of nanostructures in a continuous miniaturization process as a result of increased comprehension and advanced control of fundamental constituent blocks from bulk materials. The ability of manipulating particles at nanometric scale and to assemble them into a well-ordered array for employing in devices, has allowed the use of physical singularities of molecular nano-scale into structural and functional materials in order to modify the mechanical, electronic, optical, or catalytic functions among others [1]. In this way, the endless demand of down-scaling nanofabrication, has been based on the unique properties at the nanometer-size regime, where dimensionality and interparticle interactions are particularly distinct in comparison with big length scales as previously mentioned, and therefore encouraging the reduction of characteristic size in many working areas such as nanoelectromechanical systems, nanochemicals, bio and nano-optical sensors, catalysis and nanofluidic devices [2].

The organization of manometer-size particles in ordered arrangements due to minimization of free energy provides materials with exceptional properties in one-two- and three-dimensional structures through self-assembly processes. The highly-ordered arrangement is a fundamental requirement to attribute the special properties pursued and it must be controlled during formation and growth stages. The intricacy of continual improving towards more ordered conformation over these processes has been addressed and stimulated by biomimetic techniques with peptide constituent blocks or by inorganic templates for mesoporous materials, what in general provides a broad range of applications such as photonic, memory or single-electron microelectronic devices [1].

Nanofabrication for a wide variety of devices and its subsequent design and pattern onto substrates has been approached lithographically via different techniques encompassed in two major categories depending on the approaching scale.

1.1 Top-down

The first route is the “Top-down” approach where ordered nanostructures are fabricated scaling down bulk materials through successive subtractive and additive transfers [3]. Optical lithography is the classic method for transferring a geometric pattern to a light-sensitive material. However, the smallest characteristic of a nanodevice is approximately equivalent to the exposure wavelength. Consequently, for continuous minimization, either shorter wavelength of light should be employed or novel concepts to be developed for increasing the numerical aperture of the lens system and eventually overcome the resolution limitation of optical lithography determined by Rayleigh's equation [4]. Nevertheless, traditional lithography reaches a highest resolution of 100nm and its progress has been constrained due to the impossibility of additional reduction in micro-and nanodevices fabrication. In order to persist in miniaturization of devices, other technologies have been developed for the fabrication of structures with sizes lower than 100 nm.

Immersion lithography is an improved technology of traditional lithography where the resolution limit is reduced to 10 nm range. The numerical aperture of the lens is enlarged by placing a liquid between the lens and the wafer to exploit the larger refracting index of liquid than air. Another method developed to overcome the restrictions of optical light is E-beam lithography. Whereas the convectional lithography is designed for patterns from micrometer to sub-100nm range, electron beam lithography reaches a resolution of sub-20nm and even sub-10nm under ideal conditions. The method is based in the use of a beam of electrons that diminishes the diffraction limit in comparison with photolithography. A variation of E-beam lithography is called ion beam lithography where ions are used rather than electrons [5].

All the different methods described above, are industrially employed, with enough resolution for the current fabrication processes and specially developed and optimized for microelectronics industry. However, the cost of the equipment, the small throughput and mostly the impossibility of employing them to solve unconventional fabrication process such as curve surfaces or coatings, restrict their application in fields other than semiconductor technology [5].

The disadvantages previously mentioned have been addressed for many researches in order to overcome the limitations of top-down fabrication methods. Thereby, the conception of soft lithography was originated as a patterning technique to create and reproduce structures by a patterned elastomer utilized as a mask, stamp or mold [3]. The mutual characteristic shared with all microfabrication processes included in soft lithography is the use of polydimethylsiloxane (PDMS) elastomer instead of a rigid photomask. The patterned elastomer design starts with the preparation of a master via convectional lithography where the elastomer is poured in liquid state, cured and released with a particular structure on its surface. The main advantage compared to other conventional methods is the elastic property which helps to preserve the structural conformation of the pattern when compressing the surface; even if some undesirable particles of dust are located in between, the pattern will be more efficiently replicated than in photolithography where an undesirable flaw would be reproduced. The PDMS also provides true patterns on curved surfaces, path to quasi-three-dimensional structures and excellent chemical stability preventing molecules to react or get stuck irreversibly on the surface. On the contrary, the elastomer presents some problems such as, swelling problem while curing or flexibility weakness in contact with organic solvents limiting the aspect ratio before introducing distortions in the pattern [6].

Soft lithography is generally well suited for producing nanostructures in a broad extension of materials but however, is not optimal for nanoelectronics in which an accurate succession of piled layers comprises the integrated circuits. The PDMS softness may introduce little defects on the patterned material with a subsequent disorder between layers and misalign the whole pattern in the integrated circuit. In order to provide solutions for this drawback, different approaches have been investigated for the economic viability in the manufacture industry of nanoelectronics devices. Some of those are step and flash imprint lithography which uses a rigid stamp to avoid the imperfections introduced by the soft one. The rigid stamp is etched photolithographically in quartz, a transparent material to ultraviolet and visible light whose stiffness provides less deformation and more reliability to local features. The rigid mold pattern is then replicated via pressing it against the thin film to fill all the topographically features and the resulting photocurable thin film prepolymer solution is exposed to UV light for cross-linking and hardening the precursor. The final rigid stamp inversely reproduced from the original patterned is obtained after mold removal [7]. Another almost analogous technique is called nanoimprint lithography, which consists in transferring a pattern from a rigid mold (usually silicon) by using a thermoplastic polymer film. The polymer film is heated above the glass-transition temperature to facilitate the embossing process and then cooled down to remove the mold after pattern transfer. The method reaches features sizes up to 5 nm and the shortcomings are the heating and cooling cycles at high pressure that difficult the alignment of consecutive layer deposition and the small life time of the rigid mold of around 50 imprints [7].

Scanning probes techniques are also prominent instruments for nanometer modification. The sharp tip is used as a tool for surface modification by single or combination of different interactions e.g., electrical, mechanical, magnetic or chemical. This approach modifies and positions building blocks from macroscopic features till atomic scale to fabricate non-volatile computer memories by polymer deformation, surface modification by tip plowing or quantum devices by selective oxidation among others. In any case, this approach will be rather sorted in the bottom-up classification [8].

1.2 Bottom-up

“Bottom-up” approach is an alternative route of generating regular patterns based on self-assembly of atoms, molecules or nanoparticles into large area periodic nanostructures. Compared with top-down approach, bottom-up is a chemical and biomimetic procedure consisting in the organization of fundamental elements defined as building blocks that constitute the final patterned nanostructure. The target of bottom-up approach specifically carried out in this project is the self-organization of colloidal nanoparticles into more complex and ordered structures, ranging from film arrays to one-to three-dimensional formations. Therefore, at this point, it is indispensable to stress and clarify the distinction between self-organization and self-assembly which frequently are used interchangeably leading to an often misunderstanding in the literature, and so it will be further discussed in the following section.

During bottom-up fabrication process, self-assembly of building blocks into well-defined structures can be either spontaneous or assisted by a template. Fabrication processes carried out through nontemplated self-assembly to obtain highly-ordered structures by just combining the components are the most appealing technique since it favors the simplicity and efficiency. However, nontemplated self-assembly is not broadly used. Although energy and material consumption are both reduced in comparison with conventional lithography, this method tends to produce defects in the periodic structure and therefore to reduce the well-ordered areas to micrometer sizes. Lastly, one more drawback is the short amount of possible arrangements of self-assembled particles and consequently, the limited variety of functional structures [7]. Structural perturbations introduced during pattern formation hindering the scaling-up process can be addressed by different techniques encompassed in a more general method named Templated self-assembly. Templates are used to increase order in the self-assembled structure and consequently different interactions can be utilized to drive nucleation and self-assembly, e.g., electromagnetic fields or shear forces. An Initial technique was the utilization of patterned monolayers to lead colloidal particles on top of the substrate surface. Templated self-assembly is usually assisted by conventional lithography or top-down methods to design a template upon which the bottom-up process is driven. This templated technique has been widely employed with polystyrene and silica spheres to provide different geometrical structures with nanometer-scale arrangements and areas of micrometer or larger order without domain defects and high efficiency [9].

Structures fabricated using the bottom-up approach cover the self-assembly of monolayers and the self-assembly of more complex structures from block copolymers. Nanofabrication with block copolymers yields large-areas of ordered structures and nanosized patterns with features of tens of nanometers. However, sometimes it is required to modify the characteristics of the regular periodic structure, such as the spatial separation between domains. Therefore, Block-copolymer technique can be employed together with prepatterned substrates via top-down lithographic techniques and then self-assembly on the substrate following the designed path [10]. Another bottom-up application for practical nanostructures is self-assembled magnetic nanoparticles. Large-areas of self-assemblies of magnetic nanocrystals have attracted a lot of interest because of the enormous potential applications in biology, electronics or transport and store of extensive amount of information [11].

1.3 Coherent clarification between self-organization and self-assembly

Self-organization is a process in which increasing degree of order requires an external source of energy and therefore, the system is driven away from equilibrium by dissipating energy. Thermodynamically, self-organization is considered as an open system where transfer of matter is allowed in contrast to closed systems where heat and work but no mass are only allowed to be transferred. This condition agrees with the second law of thermodynamics in which closed systems in equilibrium are stated not to be spontaneously ordered. Consequently, self-organized structures depend on the continuous input of energy to the system and once the input energy stops, the ordering ceases. This non-equilibrium condition is the fundamental property that distinguishes self-organization from self-assembly and explicitly clarifies the usual misconception among them [12].

A definition of self-organization proposed by Scott Camazine et al., [13] is: "*Self-organization is a process in which pattern at the global level of a system emerges solely from numerous interactions among the lower level components of the system. Moreover, the rules specifying interactions among the system's components are executed using only local information, without reference to the global pattern. In short, the pattern is an emergent property of the system, rather than a property imposed on the system by an external ordering influence.*" However, this definition requires a series of specifications. Firstly, self-assembly is also described by local interactions in absence of global information. Secondly, self-organization is not only subjected to lower-level components since the system is thermodynamically open and subordinated to its unchangeable environment. Consequently, both local interactions and preexisting order in local environment influence the self-organized arrangement. Lastly, although self-organization is not considered to have a centralized guiding template, the ordering is restricted by the external interactions, they can trigger a pattern or change it, and accordingly they can be seen as external templates [12].

Taking into consideration the aforementioned, J.D. Halley and D.A. Winkler [12] have proposed a more accurate definition: "*Self-organization is a dissipative nonequilibrium order at macroscopic levels, because of collective, nonlinear interactions between multiple microscopic components. This order is induced by interplay between intrinsic and extrinsic factors, and decays upon removal of the energy source. In this context, microscopic and macroscopic are relative.*"

Self-assembly has been traditionally defined as an energy minimization process that generates well-define structures close-to-thermodynamic equilibrium. A more exhaustive definition is given by John A. Palesko [14]: "*a spontaneous formation of organized structures through a stochastic process that involves pre-existing components, which is reversible and may be controlled by proper design of the components, the environment and the driving force*". This definition stresses the non-dissipative character and the process spontaneity, once the constituent parts are integrated in the final composition, the global energy of the structure configuration is lower than the total local energy of unassembled components.

The self-assembly system is comprised of similar or different building-blocks that interact with one another via a balance of repulsive and attractive interactions [15]. This equilibrium between interactions is essential to avoid irreversibility of molecular aggregation when the particles collide and form disordered glass instead of ordered crystal structures. The character of such interactions is responsible of the reversibility and adjustability of the ordered structure, so the system is in thermodynamic equilibrium with ability of reconfiguration to local changes. Only no-covalent bonds or weak covalent interactions such as hydrophobic, Coulomb, van der Waals and hydrogen bonds provide this capability [16]. Thermal motion is responsible for mass transport and molecular interaction at molecular scale. However, in -meso- or macroscopic order, interactions such as gravity, capillarity or electromagnetic fields gain relevance in detriment of thermal motion. This need for components mobility makes the system to be generally dispersed in fluid phases or in smooth surfaces, and therefore strengthens the environment influence in molecular interactions, the energy supply for thermal agitation and course of self-assembly process. [16]

Self-assembly is divided into two main types: Static and dynamic self-assembly. Static self-assembly includes systems that approach global or local equilibrium without dissipating energy, i.e., minimization of Gibbs free energy in a closed system, such as globular proteins or molecular crystals. On the contrary, Dynamic self-assembly generates structures or patterns if the system dissipates energy. Examples of dynamic self-assembly are cell replication/assemble in the course of mitosis and bacteria swarm [16]. Consequently, since dynamic self-assembly plays a crucial role in life, concepts of dynamic self-assembly and life are necessarily related. Cells require an input of energy to survive, thus dynamic self-assembly can be considered as a self-organization process.

Besides the thermodynamic difference between self-assembly and self-organization, there are other divergences that differentiate them as processes of patterning structures. For self-assembly, basic units carry specific information of the global structure. Some constitutional parts of these primary elements interact with other components in a precise and directional route to construct the final structure in contrast with self-organization where initial encoding is not necessary. Another difference refers to the number of elemental units required to start the ordering process. Whereas in self-assembly a certain minimum of units to commence the process does not seem to be needed, in self-organizing there is a threshold of number of units below which collective order do not take place [12].

Finally, it is necessary to highlight that in many examples and phenomena it is complicated to place a boundary between self-assembly and self-organization, in many cases, they appear to overlap. Many natural phenomena comprise self-assembly and self-organization working together. In biological systems, self-assembly and dissipative process complement each other to bring about more complex and hierarchy structures. Moreover, although self-assembly is close to equilibrium process, it takes place in environments with non equilibrium conditions in the presence of heat flows and chemical reactions. In consequence, self-assembly assisted by self-organization and vice versa is a potential concept to design hierarchic order in nanodevices as well as a tool to better understand biological complexity [17].

1.4 Top-down, Bottom-up

According with the considerations previously described regarding Top-down and Bottom-up approaches, the general nanofabrication process is dependent on the particular characteristics of each technique and hence a series of conclusions drawn. The conventional lithography as described before is limited by the wavelength of light which restricts the feature sizes of the nanostructure. This constrain has motivated the introduction of alternative techniques as soft-lithography or improved conventional techniques such as electron-beam or scanning-probe lithography. Some of these methods can reach a minimum feature size of units or tens of nanometers as well as to be controlled by software. The computer assistance allows designing and fabricating nanostructures without periodic pattern or on the contrary, almost perfect arrays with long-range order. However, these techniques are serial, i.e., the desired pattern is generated pixel-by-pixel and voxel-by-voxel and therefore, extremely time consuming. Due to those reasons together with the complexity of preparation process, expensive equipment, low-throughput and small areas range, a lot of researches find the forementioned techniques not propitious for many applications [18].

Bottom-up method is a pattern generation process differentiated from Top-down in the driving force which is self-assembly and consequently a parallel process, i.e., the whole ordered arrays is created simultaneously and in consequence a more interesting ordering process. This method is also more economical and efficient, but most of the techniques encompassed in Bottom-up demand the assistance of conventional lithography. For example, soft lithography, if regarded as bottom-up technique, requires a mold fabricated via top-down technique for the mask preparation. Other disadvantages are the low production capacity of scanning probes technique or the periodicity and repeatability of self-assembly technique that difficult the shape and density control on the patterned nanostructure [19].

In any case, the feature size that can be achieved by any of those methods is around similar order as can be comparatively regarded in Figure 1.1. Both methods are not selective, indeed new hybrid methods between them are been combined for the development of nanostructured devices with reproducible results.

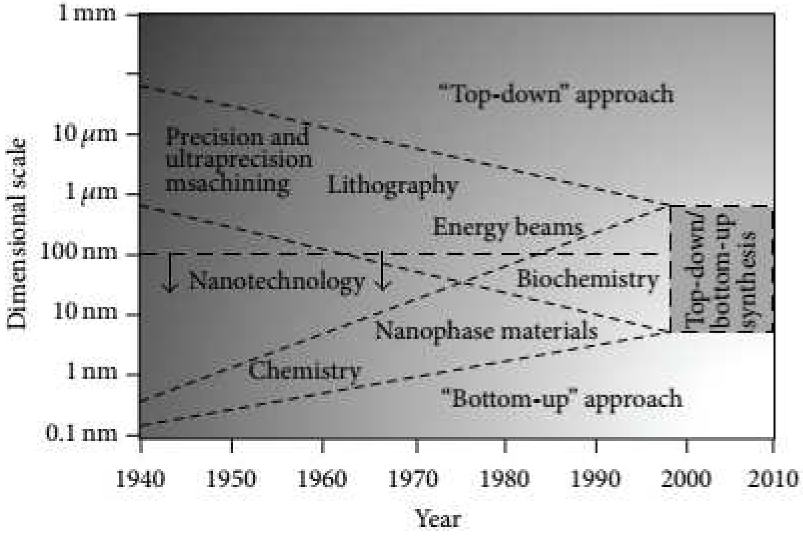

Figure 1.1: *Concurrence of Top-down and Bottom-up approach [20].*

1.5 Particle interaction

Colloidal particles dispersed in different solvents are affected by a range of attractive and repulsive forces. They are basically electrostatic in origin and the interplay between them prevents the molecular aggregation. However, despite the similar origin, all interparticle interactions take place in different ways since they are not only affected by the electrostatic interaction but also by the medium between the surfaces and in particular by the ions dissolved in it. As a consequence, the interparticle forces are divided into several categories [21].

1.5.1 Van der Waals forces

The van der Waals' interaction is a combination of forces that acts between all molecules or atomic groups independently if the molecules or atoms are uncharged or do not have dipole moment. The principle for understanding this intermolecular interaction is the Coulomb force which divides vdW forces into three groups depending on how the molecular interaction is originated. The dipole-dipole interaction arises from molecules with permanent dipoles; it is referred to as the Keesom energy. The Dipole-induced dipole interaction arises when a permanent dipole induces a dipole by polarization of a non-polar atom or molecule; it is referred to as the Debye interaction. The Dispersion force arises when at a certain moment a charge fluctuation in a molecule generates a momentary dipole that induces an instantaneous dipole in any nearby molecule or atom producing a short attractive force; it is referred to as the London interaction. The latter interaction increases with the polarizability of the molecules which usually makes the most important contribution to the total vdW force. London dispersion explains why non-polar atoms or molecules attract each other [22].

The addition of Keesom, Debye and London dispersion contributions are considered the vdW force. All of them decrease the potential energy at the same distance dependency of $1/D^6$. However, they are long-range forces, from more than 10 nm to atomic-scale around 0.2 nm and with an attractive or repulsive character [23]. The Van der Waals energy between two macroscopic solids depends on the material and the geometry of the two bodies interacting. The microscopic approach in the case of two spheres with radii R_1 and R_2 [22]:

$$W = -\frac{A_H}{6}\left[\frac{2R_1R_2}{d^2-(R_1+R_2)^2} + \frac{2R_1R_2}{d^2-(R_1-R_2)^2} + \ln\left(\frac{d^2-(R_1+R_2)^2}{d^2-(R_1-R_2)^2}\right)\right] \tag{1.1}$$

$$A_H = \pi^2 C_t \rho_1 \rho_2 \tag{1.2}$$

where d is the distance between sphere centers and D the distance between surfaces defined as $D=d-R_1-R_2$. The previous equation only takes attractive vdW forces into account. At very short distances, the molecules orbitals overlap and the molecules repel each other [22].

The Hamaker constant A_H, is defined by the equation 1.2, where C_t is the total Keesom, Debye and London energies contribution and ρ_1 , ρ_2 are the molecular density in the solid 1 or 2. The Hamaker constant is positive when vdW interaction is attractive and directly proportional to the magnitude of vdW interactions i.e., measures the strength of the vdW forces. The Hamaker constant can be calculated through the macroscopic approach of Lifshitz theory. This approach does not neglect the influence of a third molecule in the vdW interactions between two molecules. Lifshitz theory considers the solid as a continuous material ignoring the discrete atomic structure what results in the similar vdW dependencies but a different equation for Hamaker constant. It turns out that the Hamaker constant depends on the dielectric permittivity properties of the two spheres and on the dielectric properties of the surrounding medium [22].

The equation 1.1 is obtained by integrating volume elements along the two macroscopic spheres. However, when the spheres are partially immersed in two different media, the vdW interaction is more complicated than when they are in bulk phase and therefore the integration method has to be approximated and simplified.

The Hamaker approach predicts a linear dependence of the effective Hamaker constant, A_{eff}, on the volume fraction immersed in the liquid [24]:

$$A_{eff} = A_{air} + f^2(3-2f)\left(A_{liq} - A_{air}\right) \tag{1.3}$$

Where, A_{air} is the Hamaker constant for the particles in air, A_{liq} is the Hamaker constant for the particles in the liquid and f is the linear fractional immersion which is related with the contact angle θ:

$$f = (1 + \cos\theta)/2 \tag{1.4}$$

A practical method to stabilize colloidal suspensions and therefore to modify the vdW interactions is by coating the surface particle with a hydrophobic layer. Silica nanospheres have been functionalized with acidic silanol groups in a process called silanisation. In this way, Hamaker constant and Van der Waals interaction are reduced due to an increase in the interparticle distance. Particles with thicker layers tend to diminishes vdW interaction in a greater degree than particles grafted with shorter alkyl chains. In addition, particles grafted with polymer layers are affected by steric interaction. When two particles approach each other, the concentration of grafted polymer between the particles increase, the osmotic pressure is subsequently raised and a repulsive force exerted. The range of interaction depends on the chain density over the particle surface, its length and the interaction with the solvent [21].

1.5.2 Electrostatic double layer interaction

Long-range electrostatic forces also take part in the colloidal system. Otherwise the attractive vdW force between similar particles would tend to aggregate all particles in the medium and precipitate them as solid material. In fact, particles are normally charged in any liquid with high dielectric constant and in consequence coalescence is prevented through the emergence of repulsive forces between particles [21].

Most particles and substances in a polar medium have their surface charged via different mechanisms. The charge in the particle surface affects the distribution of ions in the vicinity of the charged surface; counter-ions are attracted to the surface and co-ions repelled away. Therefore, the ion organization together with the molecular mobility promoted by the thermal motion lead to the generation of the electric double layer composed of the charged surface and a cloud of ions around it. In the proximity of a particle under the double layer effect, the nature of the electrostatic interaction is modified and screened so the coulomb interaction between particles decays exponentially with the distance. In order to address this effect, the electric double layer theory try to explain the distribution of ions and the consequent electric potential at the proximity of the charged surface [25].

The origin of the charged surface can follow three mechanisms: (i) Ionization or dissociation of surface groups, e.g., aminoacids depending of pH of the solution. (ii) Adsorption or binding of ions on a surface without initial charge. (iii) Between not similar surfaces whose protons or electron are interchanged until the surfaces render an opposite charge causing electrostatic attraction. Independently of the charging mechanism, the electric double layer is divided into an inner region of charged surface by co-ions, which may include transient bounded counter-ions, and a diffuse region of counter-ions in thermal motion that balance the oppositely charged surface (Figure 1.2) [23].

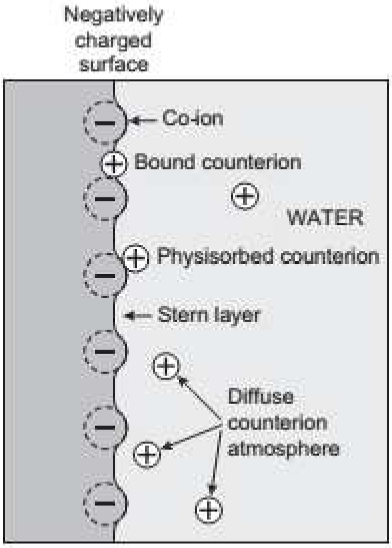

Figure 1.2: *Representation of a diffuse electric double layer [23].*

The ion concentration gradient and the related diffuse double-layer potential can be calculated by the Poisson-Boltzmann equation in which the potential decays exponentially with the distance as depicted in the Figure 1.3.

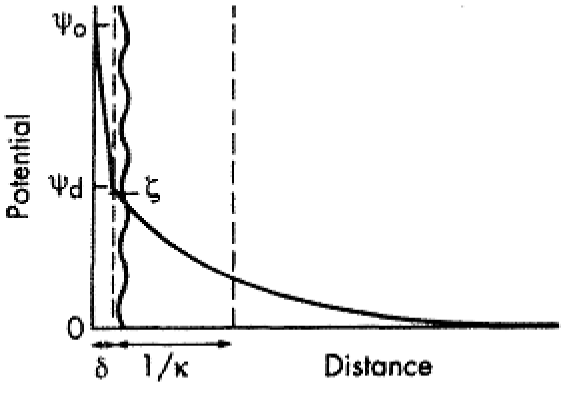

Figure 1.3: *Representation of the electric double layer potential including the layer of adsorbed ions on the surface according to Stern's theory [25].*

An important consideration is the repulsion between two identical parallel surfaces close to each other. The origin of this force is not entirely electrostatic since although the double layers of the two surfaces tend to overlap and as a result surface charges are not completely screened, the attracted counter-ions and the surface charge of each particle must be neutral. However, the main contribution for the repulsive interaction is the increase of osmotic pressure due to an excess of counter-ions accumulated in the separation gap between the particles [21]. The potential interaction between surfaces is given by the following expression:

$$W = 64 k_b T n_0 tanh^2 \left(\frac{ze\psi_0}{4k_b T}\right) \exp\left(-\kappa D\right) \tag{1.5}$$

where n_0 is the ion concentration, $k_b T$ is the thermal energy, z is the charge of the symmetric electrolyte, e is the elementary charge, ψ_0 is the surface potential, κ the inverse Debye length and D the separation distance between surfaces.

The repulsive interaction energy between planar surfaces can be adapted for particles with curved surfaces by the Derjaguin approximation. The expression for two identical spheres is given by [23]:

$$W = \frac{32\varepsilon\varepsilon_0 a (k_b T)^2 \gamma_0^2}{e_0^2 z^2} \exp\left(-\kappa D\right) \tag{1.6}$$

$$\kappa^{-1} = \sqrt{\frac{\varepsilon\varepsilon_0 k_b T}{2N_a e^2 I}} \tag{1.7}$$

Equation 1.7 represents the Debye length in an electrolyte solution where I is the ionic strength of the electrolyte, ε_0 is the permittivity of the suspending medium, ε is the dielectric constant, k_b is the Boltzmann constant, T is the absolute temperature, N_a the Avogadro number and e the elementary charge.

The double layer influence in aqueous medium can be modified by varying the Debye screening length. The Debye length is inversely proportional to the square root of the ion strength; increasing the ion concentration reduces the Debye length and thereby the strength of electrostatic repulsion decreased by a strong screening effect.

Measurement of the double layer interaction between particles at the liquid-air interface may be challenging due to theory limitations. The expression governing the double-layer interaction between particles in the medium arises from the assumption of isotropy required by the mean-field theory. However, the ion concentration is higher in the bulk than close to the interface due to solvation differences between them. Therefore, an anisotropic medium exists in the respective phases. At the same time, other influences

that difficult the double layer modeling are the effects of electromagnetic nature which give rise to dipoles in the liquid-air interface increasing the system complexity [26].
In particular, an idea to overcome the difficulty of defining the electrostatic double-layer interaction between charged spherical particles at the liquid-air interface lies on surface functionalization of particles with hydrophobic chains in non-polar environment since the surface charge density is insignificant and thus the double layer interaction negligible.

1.5.3 DLVO theory

The Derjaguin-Landau-Verwey-Overbeek (DLVO) theory explains accurately interactions and dispersion stability in colloidal suspensions. The total interaction energy between two charged surfaces is fundamentally influenced by the electrical double layer and van der Waals interplay. These two forces play different roles in the colloidal solution, whereas vdW forces cause coagulation, double-layer forces provide repulsion effects in order to promote the stabilization of the colloidal system. DLVO theory describes the coagulation process as a consequence of ion concentration increase with a subsequent reduction of repulsion effects between particles. In this way, particles in continuous thermal motion have higher chances to approach each other to few Angstroms and then to aggregate [22].

The balance between attractive and repulsive interactions in a colloidal suspension are encompassed in DLVO theory and referred as to the two important factors for the suspension stability. The energy per unit area between two spheres separated by a distance D is:

$$W_{total} = W_{edl} + W_{vdW}$$

$$W_{total} = 64 k_b T n_0 tanh^2 \left(\frac{ze\psi_0}{4k_b T}\right) \exp(-\kappa D) - \frac{A_H}{12\pi D^2} \qquad (1.8)$$

where vdW term is represented by the most common approach. The Figure 1.4 represents the energy interaction between two colloidal particles or surfaces equally charged under DLVO forces. Surfaces with high charge in a medium with low ionic concentration have long Debye length and hence long-rage repulsion. As the concentration of electrolyte increase, the energy barrier decrease and a secondary minimum emerge. In this situation, the colloidal particles may remain totally dispersed or sit at the secondary minimum since the energy barrier for aggregation to occur is still too high to be overcome. At this secondary minimum, the adhesion can be reversible and it is defined as the Kinetic equilibrium state to oppose the thermodynamical equilibrium state of the irreversible primary minimum. Further increase of the electrolyte into solution or surfaces with low charge density causes a decrease into the width of the energy barrier the same as the height when high concentration of electrolyte is added to the dispersion. The net potential energy approaches then the pure van der Waals curve and subsequently when the energy barrier reduces below the zero energy potential known as the critical coagulation concentration, the colloidal particles are unstable and coagulate meeting the irreversible adhesion primary minimum [23].

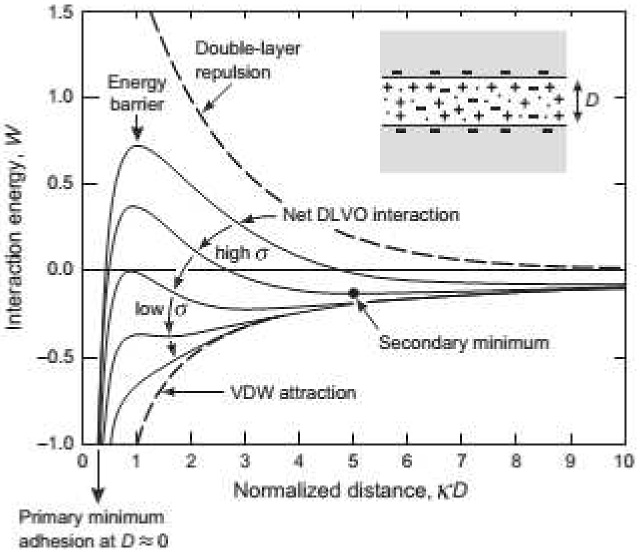

Figure 1.4: *DLVO interaction profiles schematically represented by interaction energy versus surface separation. The energy W depends on particle size and interaction area [23].*

Besides the screening of Coulomb repulsions between particles, coalescence can be also produced by decreasing the pH or by increasing cation binding. However, DLVO theory has been developed with some fundamental assumptions and simplifications to acquire an analytical solution. This theory is developed assuming a dilute colloidal system with low electrolyte concentration neglecting the discrete effect of molecular environment which is really significant between particles and medium at the interface. Those discrete effects can be regarded as the no continuity of charge density of the surface, the solvation forces arisen from the molecular medium and the finite ion size. Moreover, the mobility of ions in the electrostatic double layer creates an atmosphere of a highly polarizable layer, the main mechanism of van der Waals interaction, increasing drastically the attractions between two double layers at close separations of around 4nm or less. Lastly, electrostatic repulsion, besides colloidal stability, provides long-range ordering without which highly-ordered colloidal crystal at the air-water interface would not be possible to organize if only short-range attractions dominated the system [27].

1.5.4 Capillary forces

Capillary forces are long-range interactions at the triple phase boundary between a non-miscible solid particle, a liquid suspension medium and a third mobile phase (commonly air). The origin of capillary forces is the minimization of the surface energy in the liquid-particle interface by an appropriate surface deformation. Capillary forces principally depend on the surface tension, contact angle and particle size. Furthermore, system geometry determines the kind of capillary interaction and the direction; the capillary force may be perpendicular to the horizontal plane as in liquid bridges between spheres or parallel to this plane as in adjacent spheres [27].

The capillary interaction found in two-dimensional particle self-assembly differs from the conventional lateral capillary force between floating particles in two aspects: (i) The particles are partially immersed in water and (ii) particles with sizes even smaller than 10 nm are subjected to the lateral capillary effect, therefore particle weight and buoyancy influences can be neglected [28]. In fact, the only role of gravity by means of the disjoining pressure is to keep the film surface planar on the meniscus when the film thickness is thin enough [29]. Accordingly, capillary forces between particles are governed by surface interactions as seen in equation 1.9 [28].

$$\Pi(h) = -\frac{A_H}{6\pi h^3} \tag{1.9}$$

Where $\Pi(h)$ is the disjoining pressure, A_H is the Hamaker constant and h is the film thickness [29].

Lateral capillary force is guided almost tangentially to the horizontal plane and the main interaction involved in convective self-assembly [31]. For this reason, the distinct normal capillary force (capillary bridge force) acting perpendicular to the contact line do not have any role in the self-assembly of particles resting on a plane surface.

The lateral capillary forces arise from the deformation caused by the existence of particles on a flat liquid surface. The strength of the capillarity relies on the degree of particle perturbation on the liquid, i.e., surface deformation. As a consequence, the larger the perturbation on the superficial shape is, the stronger the capillary effect. The origin of the lateral capillary forces varies depending on the nature of interaction between the particle and the liquid surface. Accordingly, capillary effects can be divided in two distinct types regarding if particles are freely floating or partially immerse in a liquid layer [30].

Lateral flotation capillary, which can be attractive or repulsive, is related to the particle weight and buoyancy force. The attraction effect between particles leads to a reduction in the gravitational potential energy due to the convenient meniscus deformation. On the other hand, lateral immersion capillary exhibited in confined particles is more interrelated with the wetting properties, such as contact line or contact angle, than with the gravity influence [30][31]. These two different cases of capillary forces are depicted in Figure 1.5 in which flotation (Figure1.5(a),(b),(c)) and immersion forces (Figure 1.5(b),(d),(f)) are also depicted with attractive or repulsive interactions. The effect which drives the molecular adhesion or separation is related to the sign of the meniscus slopes. In flotation forces, the contact angle ψ is greater than zero for light particles and less than zero for heavy particles. Regarding immersion forces, ψ is greater than zero for hydrophilic particles and less than zero for hydrophobic particles. Obviously if ψ equals zero, there is no film deformation and thus no capillary effect. Consequently, taking into account the slopes of the two contact lines, the force will be attractive when $\sin\psi_1\sin\psi_2 > 0$ and repulsive when $\sin\psi_1\sin\psi_2 < 0$ [31].

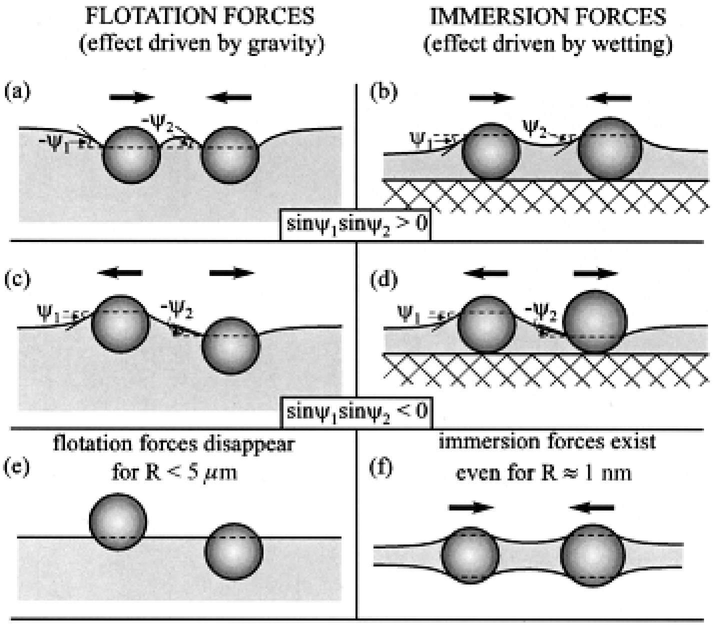

Figure 1.5: *Types of lateral capillary forces. Flotation forces (a,c,e) and Immersion forces (b,d,f) between two particles. (a) attractive capillary interaction between two similar particles, (b) attractive capillary interaction between two partially immersed particles, (c) Repulsive capillary interaction between a light and a heavy floating particles, (d) repulsive capillary interaction between a hydrophobic and a hydrophilic particles, (e) small particles with no capillary interaction between them (f) attractive capillary interaction between two particles confined in a liquid.[31]*

Capillary forces are described by the Laplace equation of capillarity which defines the liquid profile and the meniscus between two particles. The figure below depicts the liquid contour between two spheres that lead to an asymptotic solution of the non-linear Laplace equation onto a horizontal substrate without weight effect and restricted vertical displacement [32].

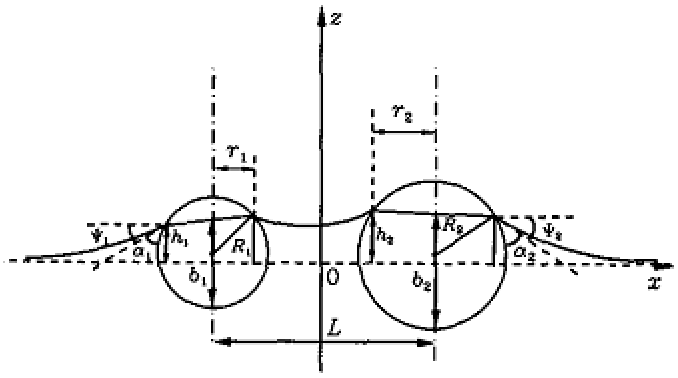

Figure 1.6: *Thin film profile and meniscus around two particles of radii R_1 and R_2, α is the three-phase contact angle, r is the radius of the contact line and L the centre-to-centre distance [32]*

The total energy of lateral capillary forces for two particles separated a distance L with radii R_1 and R_2 and contact line radii r_1 and r_2 is:

$$\Delta W \approx -2\pi\sigma Q_1 Q_2 K_0(qL) \tag{1.10}$$

where σ is the liquid interfacial tension, Q_1 and Q_2 are the "capillary charge" defined by:

$$Q_i = r_i sin\psi_i \quad (i = 1,2) \tag{1.11}$$

where r_i is the contact line radius and ψ_i is the angle with the *i* particle at the contact line. Depending if the particles are floating or partially immersed in the liquid, ΔW represents the change in gravitational energy or the wetting energy respectively [32]. The lateral capillary force is defined as the derivative F=-dΔW/dL:

$$F = -2\pi\sigma Q_1 Q_2 q K_1(qL) \qquad r_k \ll L \tag{1.12}$$

where K_1 is the first-order modified Bessel function and q is defined as:

$$q^2 = \Delta\rho g/\sigma \tag{1.13}$$

$$q^2 = (\Delta\rho g - \Pi')/\sigma \tag{1.14}$$

Equation 1.13 is used for thick films and equation 1.14 for thin films. $\Delta\rho$ is the mass density difference between fluid phases above and below the liquid contact line, g is the gravity and Π' the derivative disjoining pressure which in thick film becomes negligible [32].

The asymptotic solution (1.12) is solely valid for particles located at large distances so Q_1 and Q_2 are independent of the interparticle distance L. When particles come progressively closer and thus, the interparticle distance reduced, the contact line radius r_i and the contact line angle ψ_i, become dependent of L. Under these conditions, P.A. Kralchevsky and K. Nagayama proposed computational approximations in order to calculate the lateral capillary force for two spherical particles partially immersed [33].

The field of action of lateral capillary interactions is determined by the capillary length q^{-1} since the function K1(qL) decay exponentially when L>q-1. When qL≪1, the lateral capillary becomes relevant and the asymptotic solution of equation (1.12) is reduced to [32]:

$$F = -2\pi\sigma Q_1 Q_2/L \qquad r_k \ll L \ll q^{-1} \tag{1.15}$$

where Q_1 and Q_2 simply define the angular variation of the contact line which leads to the meniscus shape and in turn, an attractive or repulsive lateral force depending if the product Q_1Q_2 is greater or less than zero respectively. The similarity between the last equation and the Coulomb`s law, explains why Q_1 and Q_2 are known as the “capillary charge”. However, due to the dissimilar physical origins of immersion and flotation forces, Q_1 and Q_2 differ in magnitude. Therefore, surface tension and particle radius have different contribution on the lateral forces depending on the type of capillary whereas the interparticle distance plays the same role in both [31]. In the particular case of R_1=R_2=R and $r_k \ll L \ll q^{-1}$:

$$F \propto (R^6/\sigma)K_1(qL) \tag{1.16}$$

$$F \propto \sigma R^2 K_1(qL) \tag{1.17}$$

where equation 1.16 represents the proportional magnitude for flotation force and equation 1.17 for immersion force. Accordingly, a deeper insight of equations dependency exhibits that immersion force increases when the surface tension also increases. Moreover, the particle radius has a stronger influence in the decrease of flotation force than in immersion force. That is the reason why flotation force can be considered negligible for particles with radius less than 5-10 μm whereas immersion force is still significant with particles sizes down to R=2 nm and hence considered one of the most preeminent self-assembly mechanisms of colloidal particles and proteins in liquid films or lipid bilayers [30].

A comparison between immersion and flotation capillary forces of two particles separated a distance of 2R is depicted in Figure 1.7. Particle aggregation commences when the Brownian force is overcome by the capillary force. The noticeable difference in magnitude between immersion and flotation capillary is due to the degree of deformation in the liquid surface. Small floating particles give rise to small interfacial deformation causing a negligible capillary force. On the other hand, particles partially immersed in a thin liquid film with vertical displacement restriction drive more protuberant deformation in the liquid surface and hence a larger lateral force that substantially increases the particle attraction as the film becomes thinner [32].

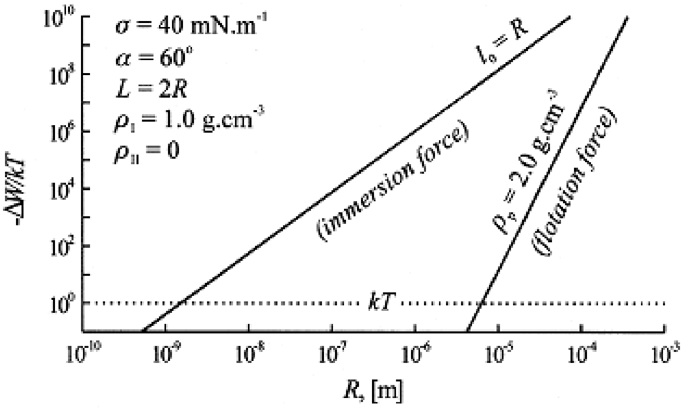

Figure 1.7: *Capillary energy in terms of KT units vs. particle radius. The two lines represent the cases of two similar particles partially immersed on a horizontal substrate and two particles floating in the liquid-air interface. The values of particle mass density* ρ_p*, surface tension* σ*, contact angle* α*, interparticle distance L and density difference* ρ_I*, are inserted in the illustration [32].*

The origin and approach of the Lateral capillary interactions in each particle is the sum of two forces: The hydrostatic pressure over the non-immersed particle surface and the interfacial tension of the meniscus along the contact line of the particle. The overlap of perturbations in each particle causes an inclined contact line L_1 and L_2 which becomes more prominent as the interparticle distance decreases. The irregular contact angle over the particle causes an asymmetric force distribution with a final net horizontal force [31].

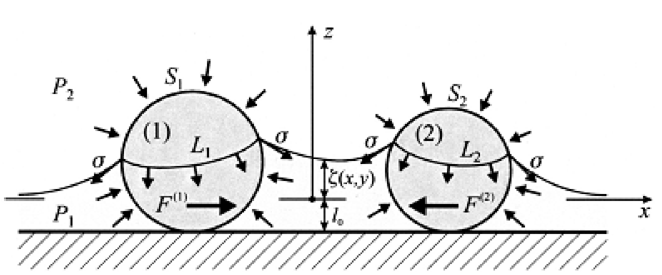

Figure 1.8: *Force distribution over two particles partially immersed in a liquid.* S_1 *corresponds to the particle surface affected by the hydrostatic pressure and* L_1 *the contact line where the surface tension* σ *acts. F is the net horizontal force contribution.* P_1 *and* P_2 *are the pressures in the different phases,* $\zeta(x,y)$ *is the meniscus shape and* l_0 *the plane-parallel liquid layer [31].*

The self-assembly of nanostructures from colloidal particles is mostly influence by lateral immersion capillary forces and electrostatic interactions. The interplay between these two effects plays an important role for structure organization. In this particular method, the lateral immersion capillary attractive energy overcomes the electrostatic repulsion in various orders of magnitude, an essential characteristic for particle organization and structure configuration. The capillary lateral force varies during the evaporation process in the self-assembly of colloidal particles. Therefore, the interaction between opposing capillary forces and frictional forces as hydrodynamic drag force changes considerably [27].

1.5.5 Non-DLVO forces

All molecular interactions described above are primary forces in self-assembly processes. However, DLVO theory fails explaining the behavior of particles separated a distance of few nanometers since it is based on continuous density and uniform orientation. Therefore, several interactions besides DLVO theory complete the interplay at short-range separation. These complementary and significant Non-DLVO forces are: Solvation, Hydration, Hydrophobic, Steric and hydrodynamic forces.

The solvation force is originated when a liquid is confined between two surfaces in a region over a few molecular diameters. In this small environment, molecules are ordered in layers which are squeeze out one by one as the surfaces keep approaching. For this reason, the resulting interaction is oscillating between attractions when particles are freer or repulsion when particles are tightly ordered. These forces were named solvation forces because they depend on the adsorption of solvent molecules onto the approaching surfaces [22].

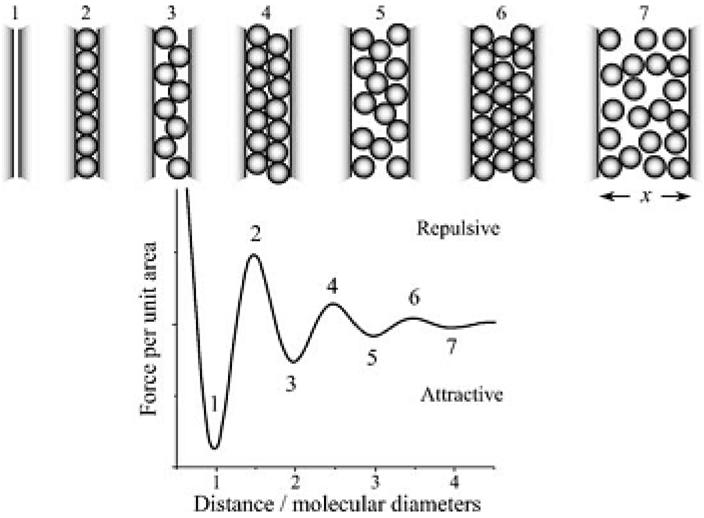

Figure 1.9: *Periodic force emerged for the severe change of molecular order inside two solid parallel surfaces approaching each other [22].*

The hydration force is a repulsive effect that introduces notable divergences with DLVO theory predictions when water molecules are bounded to ions or ionized surfaces. Even at situations of small separations with high electrolyte concentration in which van der Waals interaction should dominate and promote aggregation, the extra repulsion provided prevents the molecular coalescence of hydrophilic surfaces in an effective range up to 3-5 nm. The hydration forces arise from hydrogen bonding of hydroxyl surface groups and consequently the repulsion energy is proportional to the bonding disruption and dehydration process. The hydration repulsion energy between two hydrophilic surfaces decay exponentially with the distance [27]:

$$W = W_0 \, e^{\frac{-D}{\lambda_0}} \tag{1.18}$$

where $\lambda_0 \approx$ 0.6-1 nm and $W_0 \approx$ 3-30mJ/m^2 [27].

The hydrophobic forces arise from the orientation of water molecules around the hydrophobic particle. This molecular order is entropically unfavorable and consequently the water molecules try to overcome the absence of bonding establishing hydrogen bonding between other neighboring water molecules while avoiding hydrophobic molecules. Consequently, water molecules reconfiguration facilitates the molecular interaction and attraction between hydrophobic molecules. The hydrophobic attraction, with a long-range up to 100 nm, could be even stronger than van der Waals interaction. However, at short-range interplay, the interaction exponentially decay between 1-2 nm; as the two surfaces approach each other, water structure is forced to rearrange and the hydrophobic effect is then weakened. Thus, for two hydrophobic surfaces the hydrophobic total energy between 0-10 nm is given by [22]:

$$W = -2\gamma_i e^{\frac{-D}{\lambda_0}} \tag{1.19}$$

where γ_i is the interfacial energy typically 10-50 mJ/m^{-2} and $\lambda_0 \approx$ 1-2 nm.

The Steric force arises when colloidal dispersions are stabilized by polymers. The force between two coated surfaces strongly depends on the quality of the solvent since it affects the direct interaction between polymer chains. In good solvents for the polymer, the force exerted by the segments is repulsive whereas in bad solvents the resulting force is attractive. On the other hand, the net force also depends on the quantity of bound polymer onto the surface. When two polymeric-functionalized surfaces approach each other, the mobility of the polymer chains is reduced and hence the entropy decreases. Furthermore, while surfaces approach, the concentration of polymers in the gap between surfaces grows with a subsequent osmotic pressure increase. The entropy decrease and osmotic pressure increase lead to a net repulsive interaction force [27]. The repulsion force for low grafting density between two coated surfaces in a good solvent is defined by [34]:

$$\Pi(x) = \frac{2k_bT\Gamma}{x}\left(\frac{2\pi^2R_g^2}{x^2} - 1\right) \; for \;\; x \leq 3\sqrt{2}R_g \tag{1.20}$$

$$\Pi(x) = \frac{2k_bT\Gamma x}{R_g^2} e^{-\left(\frac{x}{2R_g}\right)^2} \; for \; x > 3\sqrt{2}R_g$$

Where Π is the repulsive steric disjoining pressure, Γ is the grafting density and R_g is the radius of gyration.

For high grafting density the force per unit area is related to [34]:

$$\Pi(x) = k_bT\Gamma^{\frac{3}{2}}\left[\left(\frac{2L_0}{x}\right)^{\frac{9}{4}} - \left(\frac{x}{2L_0}\right)^{\frac{3}{4}}\right] \tag{1.21}$$

where L_0 is the thickness of the polymer layer. The previously defined repulsive steric disjoining pressure for functionalized surfaces with low or high polymer concentration is depicted in the figure 1.10.

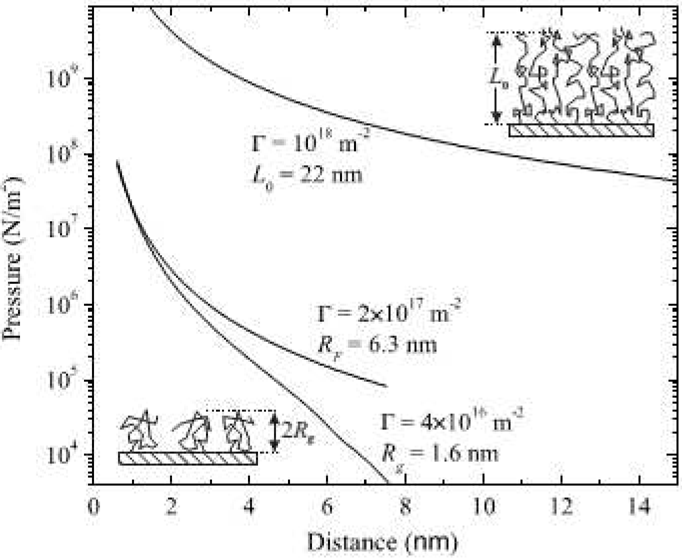

Figure 1.10: *Repulsive steric disjoining pressure between two surfaces coated with low, intermediate and high polymer density in a good solvent. The parameters assumptions are entered in the figure [22].*

The hydrodynamic forces play an influential and crucial role in self-assembly evaporative techniques due to the convective flow of particles from the periphery to the meniscus. This convective flow is originated by the stronger evaporation rate at the droplet three-phase contact tending to concentrate particles at the nucleation point. The hydrodynamic drag force overcomes the electrostatic and van der Waals interactions by orders of magnitude so the particles are displace and packed tightly. This effect will be further discussed in detailed [27].

1.6 Nanosphere lithography

Nanosphere lithography is a promising low-cost, efficient, flexible and parallel nanofabrication technique susceptible of producing a wide variety of nanostructures and well-ordered two-dimensional arrays. The ordered arrays of colloidal particles and the interstices between them are utilized as masks or templates to design patterns through etching or material deposition. The monodisperse colloidal particles used are efficiently synthesized through emulsion polymerization and sol-gel processes with large variety of sizes and shapes that range from tens of nanometers to micrometers. This size uniformity in a dispersed phase allows particles to self-assembly into two dimensional array or even into three dimensional periodic formation commonly known as colloidal crystal [35].

Nanosphere lithography takes advantage of positive characteristics of bottom-up and top-down techniques to combine them in a two-step fabrication process. A simple method is represented in the Figure 1.11 in which mask generation is the first step. A droplet of monodisperse colloidal suspension of e.g. silica or hydrophilic-functionalized polystyrene is deposited over a substrate. Upon drying, the self-organized monolayer or bilayer formed is then employed for selectively design a pattern through the nanospheres interstices via material deposition. The mask is then detached (lift-off) from the substrate by sonication in a convenient solvent and therefore a desired pattern left behind on the substrate. Other steps may be required such as annealing which initiate a crystallographic phase change [3].

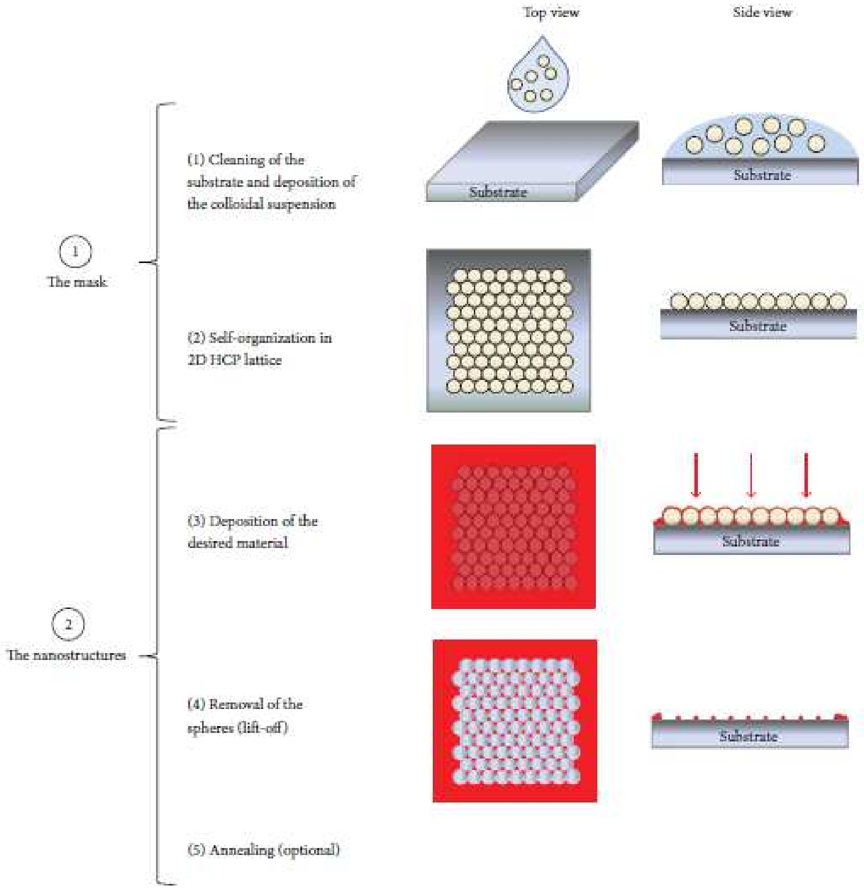

Figure 1.11: *Nanosphere lithography process [3].*

Nanosphere lithography is also known as colloidal lithography or natural lithography. The concept of natural lithography was introduced for the first time by Fischer and Zingsheim [36] in 1981. They obtained a small array of self-organized polystyrene particles with a diameter of 312 nm by simple evaporation process. Soon after, Deckman and Dunsmuir expanded the Fischer’s approach by showing that a self-assembled array of colloidal nanospheres could be used both as a “deposit material” and as a mask [37]. The term natural lithography comes from the fact that masks formation is generated by self-assembly phenomenon instead of by photolithography. In the 90s Van Duyne et al., renamed this method to be more descriptive in practice, and it is still currently known as nanosphere lithography. Their work were based in an extension of the single-layer methodology as well as the development of double layers which provide small dots of periodic particle arrays due to smaller interstices after material deposition onto the close-packed mask [38].

The need of reproducible results and trustful fabrication process has led the efficient and inexpensive Nanosphere lithography to a continuous refinement and development through a better control in shape, size and interparticle distance. The process always starts with a colloidal solution of nanospheres suspended in a specific solvent and deposited onto a substrate specifically selected for mask self-assembly. The deposition methods employed such as droplet evaporation, vertical deposition, dip-coating, Langmuir-Blodgett coating and spin coating among others, allow particles to freely diffuse in order to organize and therefore minimize the energy of the system. The particle mobility across the substrate is often carried out by a negative functionalization of the particle surface that electrostatically repels the negatively charged substrate and hence the capillary forces transport the nanospheres more easily to the nucleation site for crystal growth. The monolayer colloidal crystals inherently self-assembly in a hexagonal-close-packed pattern including a range of structural defects due to polydispersity, vacancies, slip dislocations and dissimilar domains that limit the size of defect-free areas between 10 to 100 μm^2 [39].

1.6.1 Single layer periodic particle array

The single layer periodic particle array (SL PPA) or hexagonal-close-packed monolayer colloidal crystals is the most common and simple self-assembled hcp monolayer since the two-dimensional arrangement is thermodynamically stable [39]. The surface symmetry of the single layer is used for metal deposition through the sphere interstices leading to triangular-shaped nanoparticles that are organized in an array with P_{6mm} symmetry [40]. The regular pattern depicted in the figure 1.12 is characterized by the particle metrics and their relationships in the mask geometry. The perpendicular bisector of the particles defined as the in-plane particle diameter, a, and the interparticle spacing, d_{ip}, for the SL PPA are mathematical described as [40]:

$$a = \frac{3}{2}\left(\sqrt{3} - 1 - \frac{1}{\sqrt{3}}\right) D \qquad (1.22)$$

$$d_{ip} = \frac{1}{\sqrt{3}} D \qquad (1.23)$$

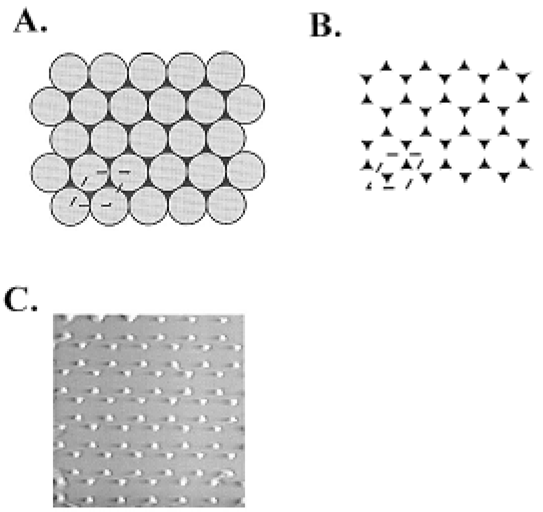

Figure 1.12: *Schematic representation of SL PPA. (A) Single layer mask. Dotted line represents one unit cell. (B) Two particles per cell. (C) 1.7x1.7μm constant height AFM image of Ag nanoparticles with D=264nm onto mica substrate [38].*

The particles cover 7.2% of the substrate in the figure 1.12 in which height is not controlled by the properties of nanosphere technique although it should be equal to the mass thickness of the material deposited over the monolayer mask. The SL PPA is able to fabricate large areas without defects and is one of the most usual nanosphere techniques for the basis of nanostructure modeling [38].

1.6.2 Double layer periodic particle array

When nanosphere concentration is increased in the solution, the colloidal crystal is not entirely assembled into a monolayer since a significant part of it will be formed by a crystal of hexagonal-close-packed bilayer. The double layer periodic particle array (DL PPA), is an assembly of two monolayers, one above the other, blocking three-fold hole and hence a smaller density of dots are available for metal deposition. After deposition and Nanosphere liftoff, a regular pattern of hexagonal nanoparticles in shape are left on the substrate as it is shown in figure 1.13. The mask geometry provides the relationships between the diameter of the hexagonal particles, a, and the interparticle spacing, d_{ip}, as a function of nanosphere diameter D [39] [40].

$$a = \left(\sqrt{3} - 1 - \frac{1}{\sqrt{3}}\right) D \tag{1.24}$$

$$d_{ip} = D \tag{1.25}$$

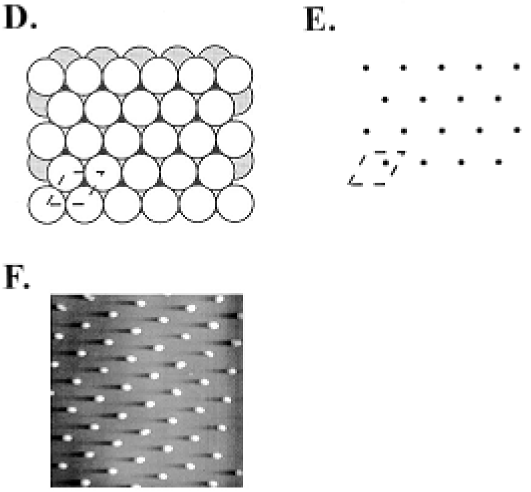

Figure 1.13: *Schematic representation of DL PPA. (A) Double layer mask. Dotted line represents one unit cell. (B) One particle per cell. (C) 2x2 μm constant height AFM image of Ag nanoparticles with D=264nm onto mica substrate [38].*

The AFM image in the Figure 1.13 shows a 4μm^2 without defects with 2.2% of substrate coverage. The features of DL PPA nanoparticles can be adjusted by controlling the properties of the metal deposited onto the nanosphere mask by means of mass thickness and nanosphere diameter, or even with a third layer assembled on top of the double layer mask. In this scenario, successive monolayer packing in the sequence ABAB is a regular hcp arrangement where the hexagonal interstices remain opened to the substrate. On the contrary, further packing of layers in the ABCABC sequence defines a face-centered cubic (fcc) arrangement with an equally dense packing than hcp but blocking all the mask holes and therefore impeding the deposited material to contact the substrate [40].

DL PPA has been proposed as a structural designing technique for patterning single domains of magnetic nanoparticles encompassed in nanosphere methods in which domain magnets will play more efficiently as “ones” and “zeros” in binary data storage [40].

1.7 Self-assembly methods of monolayer colloidal crystal

1.7.1 Two-dimensional convective self-assembly

The two-dimensional mechanism for self-assembly of colloidal particles in suspension on solid surfaces is mainly driven by two interactions: Lateral capillarity and convective flow. The dynamics of the 2D crystallization begin with a nucleus formation in which capillarity plays a preeminent role. The nucleation phenomenon is led by attractive forces between partially immersed neighboring particles and a subsequent convective flux caused for the evaporation excess from the well-ordered array that is being formed. The approaching model commences when the liquid surface curves towards concave arrangement while gradually gets thinner. In this way, once the liquid height equals the particle diameter, a 2D crystal nucleus is formed and therefore, the self-assembly process initiated. As evaporation continues, the particles protrude from the water surface giving rise to capillary effects that force to particles surrounding the nucleus to move towards the nucleation zone and to organize. Thereafter, further evaporation, reduces the water molecules between neighboring particles leading to a menisci formation promoted by surface tension. These menisci hinder the continuous evaporation of the thinner water layer and therefore, to overcome the energetic opposition for further evaporation, convective flux transport particles from the thicker water layer to the thinner one eventually originating the molecular order and crystal growth [41].

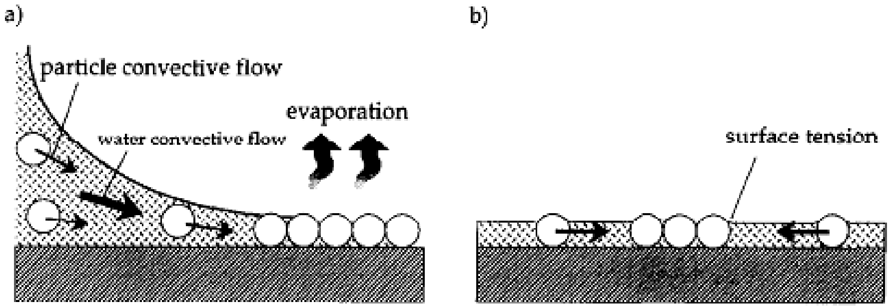

Figure 1.14: *Particle assembly mechanism driven by water flux and capillary force during solvent evaporation of a colloidal solution. (a) Movement of particles by convective flow due to evaporation (b) Attractive lateral capillary force between two particles due to surface tension and surface deformation [42].*

The convective transport is well-known to be the mechanism by which coffee droplets leave a ring-like shape after evaporation. Solid particles primarily dispersed all over the droplet are carried together with liquid supply to the interface, from the interior to the droplet outline in a flux that replaces the liquid evaporated in the edge. The transit of particles from the inside to the outer periphery continues as long as the contact angle is non-zero, the contact line is fixed and solvent evaporation is taking place [43]. The convective transport is explained in more detail during evaporation process by the contribution of geometrical restrictions. The droplet height h(r) is reduced by contraction from all sides with an expected radius decrease. However, the droplet radius cannot be reduced since the contact line is pinned and consequently the height reduction is restricted to droplet shrinkage. At the same time, the surface tension constricts the droplet spherical shape. Therefore, in order to keep the geometrical restrictions imposed during evaporation, solvent molecules and particle flow are carried to the edge, as shown in Figure 1.14b.

The transport velocity is related to the evaporation rate J(r) involved in the whole evaporation process, which is depicted in the Figure 1.15. An important condition that influences the evaporation rate is the vapour concentration c(r) close to the droplet surface, which is saturated due to evaporation, and consequently J(r) diffuses outwards. Vapour rapidly reaches the steady-state concentration on the droplet surface, i.e., the concentration does not change with time so Fick’s first law can appropriately describe the evaporation rate by relating the evaporative flux with the concentration gradient.

$$J(r) = -D\nabla \mathrm{c} \tag{1.26}$$

where D is the diffusivity of vapour in air. The evaporative flux depends on the distance r as it comes closer to the edge of the droplet, with a final expression [43]:

$$J(r) \propto (R - r)^{-\lambda} \tag{1.27}$$

where R is the droplet radius and $\lambda = (\pi - 2\theta_c)/(2\pi - 2\theta_c)$ which increases up to 0.5 as the contact angle decreases to 0. Thereby, the velocity of mass transport towards the droplet boundary is proportional to the evaporation flux and complements the restrictions previously mentioned. All points situated at r > 0 are transported towards the edges, as defined by the previous equation, where more convex regions have higher evaporation rate and therefore denser particle deposition.

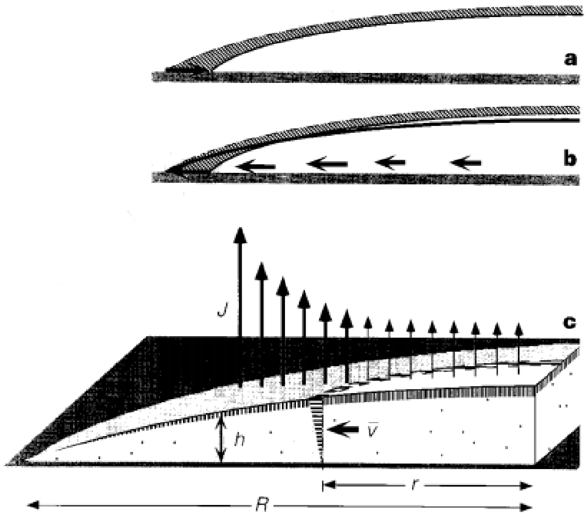

Figure 1.15*: Mechanism of droplet evaporation. (a) Droplet shrinkage during evaporation with free retracting movement of contact line. (b) Required flow in order to pin the contact line. (c) Outward flow during evaporation process and solute transport velocity towards the edge [43.]*

In conclusion, 2D crystal array formation over a solid substrate proceeds via two processes; nucleation through lateral capillary, and a subsequent crystal growth through convective flux during water evaporation. The particles are attracted by lateral force creating a nucleus at some unknown place of the substrate since nucleation is a random process while more particles from the bulk are brought into close contact enlarging the crystal array formation in a continuous self-assembly mechanism [44].

1.7.2 Dip-coating

This method is based on the studies of monolayer formation through convective assembly in evaporation deposition. However, the distinctive characteristic is that the substrate is vertically removed from a bulk suspension of colloidal nanospheres with a fine-tuning withdrawal speed. The large-area self-assembled monolayer obtained with high regularity and defect-free has assigned dip-coating one of the most reliable nanosphere lithography methods.

The self-assembly of ordered structures by dip-coating is basically divided in three important technical stages described as: Immersion and dwell time, deposition and drainage, and evaporation. The first stage is immersion and dwell time, a substrate is immersed into a colloidal suspension at a constant speed followed by a dwell time at which the substrate remains fully covered and motionless inside the bulk solution to provide sufficient time for substrate-particle wetting. The second stage is deposition and drainage, the substrate is pulled up from the colloidal solution at a constant speed and a thin film is then deposited. Excess of liquid is drained from the surface to the bulk and the coating thickness will depend on the withdrawal speed. The last stage is evaporation, the solvent evaporates from the substrate and the deposited particles self-assembly in a well-organized thin film [45].

Dip-coating is a quite simple method, but however a better understanding of the underlying microscopic processes during film formation allows controlling the properties and quality of self-assembled monolayer or multilayer. The thin film formation can be divided in a first convective particle transport form the bulk to the substrate due to solvent evaporation in the thin film surface followed by interparticle interaction that leads to array order. The origin of the interparticle interaction in a saturated vapour atmosphere comes from the modification of pressure equilibrium in a small bulk volume inside the thin film.

$$\Pi + P_{cp} = P_c + P_h \tag{1.28}$$

$$P_h = \Delta\rho g h_c \tag{1.29}$$

Where Π is the van der Waals and electrostatic disjoining pressures, P_{cp} is the capillary pressure due to liquid curvature in the thin film, Pc is a capillary pressure reference, Ph is the hydrostatic pressure, h_c the relative height, $\Delta\rho$ is the density difference between the suspension and the surrounding air and g is the gravity. In an atmosphere unsaturated with water, the evaporation mechanism takes place and the terms in equation 1.28 vary modifying the equilibrium. The right-side term remain almost invariable since the capillary pressure reference is related to the horizontal suspension and hence equals zero. In the same way, the small increase of the relative height can be minimized by adding colloidal suspension to counterbalance. However, the menisci curvature increment due to evaporation causes the left-side term to increase in both components producing a pressure gradient from the bulk to the film substrate [46]. The pressure increment is shown in the equation 1.30.

$$\Delta P = \left(\Pi + P_{cp}\right) - \left(P_c + P_h\right) \tag{1.30}$$

Evaporation in the suspended thin film, $j_{e,}$ originates a flux between the bulk and the vertical substrate which consists on a water component, $j_{w,}$ and a particle component, $j_{p,}$ as depicted in figure 1.16. Fluxes compensation via convective particle transport causes particles to move towards the substrate and organize forming compact structures in the thin film [46].

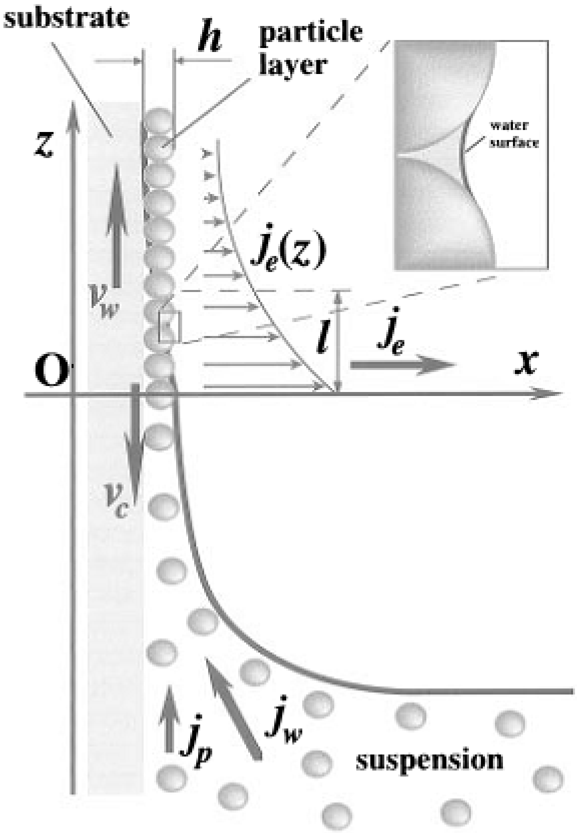

Figure 1.16: *Theoretical considerations of self-assembly particle array film on a substrate that is slowly withdrawn from the colloidal suspension. The inset represents the menisci between to particles.* v_w *is the substrate withdrawal rate,* v_c *is the array growth rate,* j_w *is the water influx,* j_p *is the particle influx,* j_e *is the water evaporation flux and h is the thickness of the array [46].*

The regular formation of 2D structures requires that withdrawal speed equals the rate of array formation. Therefore, the withdrawal rate for periodic self-assembly formation is calculated in a steady state process when there is a material flux balance between the evaporation flux and the water flow from the bulk to the substrate. The withdrawal rate for 2D growth of particle arrays is defined as [46]:

$$v_w = v_c^{(k)} \frac{\beta l}{0.605} \frac{j_e \varphi}{kd(1-\varphi)} \tag{1.31}$$

Where $v_c^{(k)}$ is growth rate of the k-layer array, φ is the particle volume fraction, j_e is the evaporation rate, d is the particle diameter k is the number of layers, l is the evaporation length and β is the coefficient of proportionality between the macroscopic mean velocity of the suspended particles and the macroscopic mean velocity of the water molecules. For weak interactions and dilute suspension β approaches 1 whereas for strong particle-particle and/or particles-substrate interactions approaches 0 [46].

The withdrawal speed has an important influence in the array organization and in the final thickness of the thin film. In case of very slow lifting speed, water evaporation exceeds the substrate movement initiating an agglomeration process above the drying line as a consequence of continuous convective transport of particles that balances the evaporation effect. On the contrary, too high withdrawal speed hinders the arrival of colloidal particles over the substrate resulting in scattered stripes or only a narrow region with high order [45].

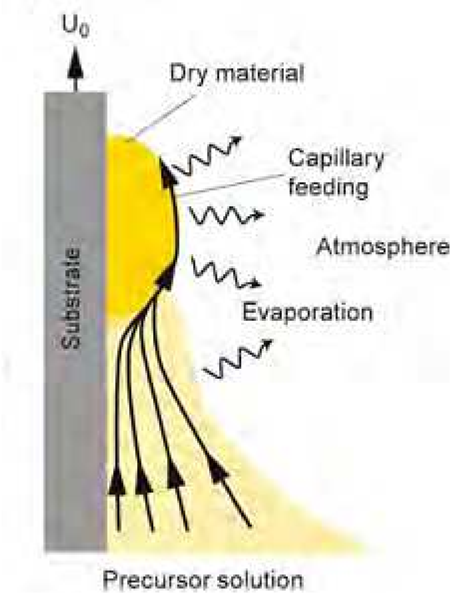

Figure 1.17: *Particle accumulation in the upper part of the meniscus at low withdrawal speed [45].*

Other requirements for self-assembly of highly regulated structures can be described as important influential variables. The relative vapour saturation surrounding the substrate at saturated levels dictates an extremely slow assembly as in comparison with not saturated environments. Particles and substrates negatively charged provide an electrostatic repulsion at close contact inside the suspension that together with the interparticle electrostatic repulsion during self-assembly, lead to arrays with dense packing of particles. Furthermore, the thickness of the wetting film, h_f, has an important relationship with the colloidal particle diameter. When the particle diameter is less than h_f, bumps of particles could be found in the substrate after drying, on the other hand, when the particle diameter is much greater than h_f, the particles are driven to the bulk by the inclined meniscus and no particles are found on the substrate after drying. Lastly, a further reduction of h_f causes an increase in the lateral capillary force and subsequently an increase in ΔP in equation 1.30. Therefore, the friction force between the particles and the substrate is also increased which may impede the particle reorganization in the array and eventually to generate shorter domains [47].

1.7.3 Langmuir-Blodgett coating

The Langmuir-Blodgett technique has been proven as an efficient way of preparing organized molecular assemblies with a precise control of the layer structure at molecular level as well as the resulting film thickness. The classical materials used in this technology for monolayer formation are amphiphilic molecules due to their hydrophobic and hydrophilic character. The amphiphilic nature of these molecules dictates the orientation and organization in the air/ water interface to minimize free energy and to assemble an insoluble monolayer [48].

The monolayer preparation starts with dissolving amphiphilic molecules in a volatile organic solvent and subsequently spread at the air-water interface. After solvent evaporation, the amphiphiles are structured in a monolayer which is manipulated via mobile barriers that control the area available per molecule. The adsorption of surface-active agents at the interface and the subsequent monolayer formation is thermodynamically driven by the energy excess of the liquid surface which imposes the molecular orientation and reduces the system energy through surface tension decrease [49]. As the film is compressed by reducing the molecular area available, the surface tension of the pure liquid is reduced proportionally to the force exerted by the film. Therefore, the difference between the surface tension of the pure subphase (γ_0) and the surface tension with the monolayer present (γ) is called surface pressure (Π):

$$\Pi = \gamma_0 - \gamma \tag{1.32}$$

Where Π is the two-dimensional analog of pressure corresponding to the force applied per unit length by the film. The surface pressure is measured by the Wilhelmy plate method which usually consists in a thin platinum plate partially immersed in the liquid subphase (figure 1.18). The forces acting on the plate are the gravity and the surface tension as downward forces and the buoyancy as upward force. Therefore, the net downward force acting on a rectangular plate is defined as [48]:

$$F = \rho_p gLwt + 2\gamma(t + w)\cos\theta - \rho_L gtwh \tag{1.33}$$

where L, w and t are the length, width and thickness of the rectangular plate respectively, ρ_p is the plate density, θ is the contact angle between liquid and solid plate, ρ_l is the liquid density, g is the gravity and h is the immersed height.

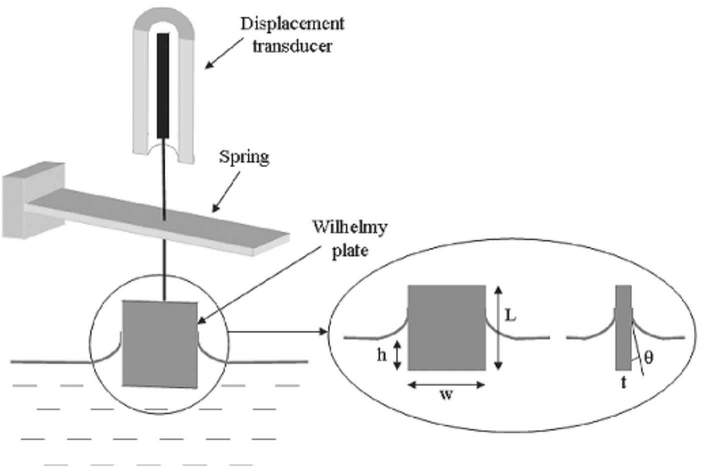

Figure 1.18: *Sketch of Wilhelmy method for surface pressure measurement.*

The Langmuir-Blodgett technique commences spreading molecules at low concentration onto the water surface to assure that the molecular dispersion is high enough and the lateral adhesion forces between particles are avoided. At this stage, the monolayer is regarded as a two-dimensional gas phase where molecules have almost no effect on the surface energy of the water subphase. When the mobile barriers start compressing the film, the area available per molecule is reduced, so the amphiphilic molecules are forced to organize and in consequence to increase the order. The molecules react to the geometrical restrain by exerting a repulsive force that opposes the compressive force what decreases the surface energy regarded as surface tension. Further compression gives rise to order increase through several phase transformations analogous to gas, liquid and perfectly ordered solid state [50].

The continuous monitoring of the surface pressure as a function of available area per molecule while the monolayer is progressively compressed leads to the surface pressure (Π) – Area (A) isotherm diagram depicted in the figure 1.19. The different molecular organizations due to different degrees of freedom during compression give raise to different aggregation states that correspond with discontinuities between phases in the isotherm [50].

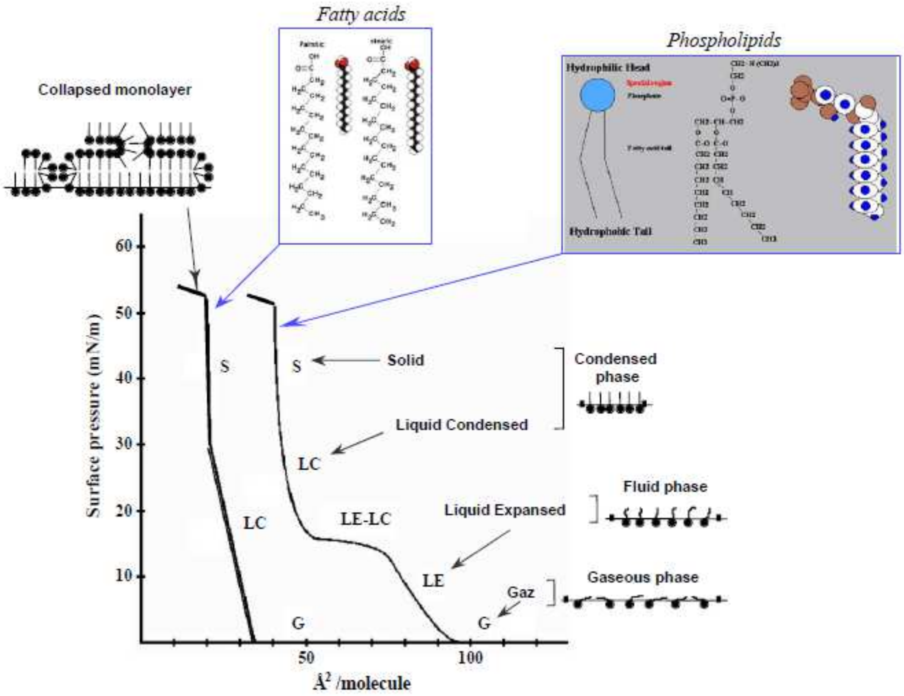

Figure 1.19: *Schematic Π-A isotherm of fatty acids or phospholipids [50]*

Surfactants can aggregate in aqueous and non-aqueous media to form many different structures or behave as emulsifiers in emulsion preparation. However, it has been also proven that colloidal particles behave quite similar to amphiphilic molecules at the water-air interface with only dissimilarities in the way of assembly, i.e., for solid particles, solubilization phenomenon does not take place. However, they efficiently attach thermodynamically to the interface and therefore, they can be also conveniently transferred on different substrates by LB technique. This analogy between surfactants and individual particles has promoted the use of water/air interface as a medium for self-assembly of colloidal particles with the subsequent monolayer transfer onto a solid substrate by controlled withdrawal [51].

The most relevant parameter that characterizes the adsorption of surfactants to the water-air interface is the packing parameter. However, in case of solid spherical particles adsorbed at the interface, the contact angle θ between the particles and the interface is the most important characteristic. For hydrophilic particles, θ is usually less than 90º and the main part of the particle remains immersed in the water phase whereas for hydrophobic particles θ is normally greater than 90º and a larger part of the particle surface dwells in air.

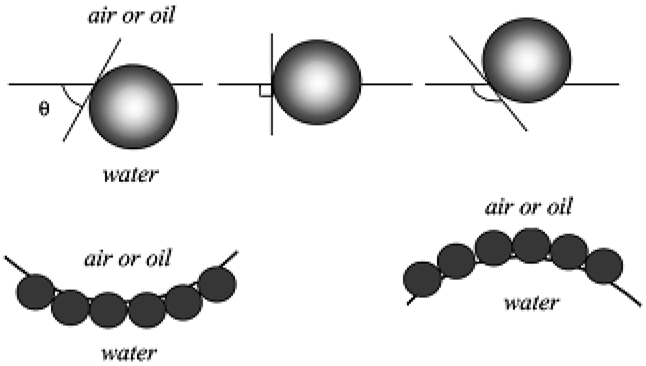

Figure 1.20: *(Upper) Spherical particle at the interface with contact angle less than 90º, equal to 90º and greater than 90º. (Lower) Interface curvature for particles with contact angles less than 90º (left) and greater than 90º(right) [51].*

Hydrophilic and hydrophobic solid particles assembly into monolayer with strong attachment to the interface despite the lack of amphiphilic character and the much less spherical symmetry than surfactant molecules. The energy of attachment of a solid particle at the air-water surface is not only related to the contact angle but also to the tension of the interface. The energy needed to remove the particle from the interface towards the air phase or towards the water phase is given by [52]

$$E_{OUT} = \pi R^2 \gamma_{LA} (1 + \cos\theta)^2 \tag{1.34}$$

$$E_{IN} = \pi R^2 \gamma_{LA} (1 - \cos\theta)^2 \tag{1.35}$$

Equation 1.34 represents the energy of removal to the air phase and equation 1.35 the energy of removal to the water phase. R is the particle radius, γ_{LA} is the liquid-air interfacial tension and θ is the contact angle between the particle and the interface. The last two equations show that particles are more attached to the interface when θ=90º and $E_{IN} = E_{OUT}$, while for angles less than 90º the energy of detachment needed for removing the particle to the bulk is decreased, i.e., the particle is hydrophilic. On the contrary, for angles greater than 90º the energy of detachment needed for particle removal from the interface towards the air phase is decreased, i.e., the particle is hydrophobic. The smaller amount of energy required to move the particle upward is the reason why preparing films of hydrophobic colloidal particles using LB technique has been transferred onto a solid substrate by up-stroke [52].

Colloidal crystal formation in Langmuir-Blodgett trough is induced by a continuous compression of the particles. The solid phase starts consequently when the area available per molecule is diminished and the mean interparticle distance is equal or greater than twice the Debye length plus the particle diameter. In this scenario, conveniently hydrophobised silica particles have been observed to order in a hexagonal close-packed monolayer. Therefore, in order to characterize the LB films, the surface pressure-area isotherm is used to measure the surface pressure for such monolayers. The surface area available per particle is calculated as A=At/N where A_t is the total interface area available for the particles with the barriers completely opened and N is the amount of particles spread on the interface [53]:

$$N = (m/\rho)/(4\pi r^3/3) \tag{1.36}$$

where m is the mass of the spread particles, ρ (g/cm^3) is the sphere density and r the sphere radius. Additionally, the film density (g/cm^2) is defined as:

$$\delta_{film} = \frac{m}{S} \tag{1.37}$$

where S is the area occupied by the film. The unit cell of hexagonal packing contains one sphere with mass defined as $m=4/3\pi r^3\rho$. The area per particle in the unit cell is given by:

$$A = 2\sqrt{3}\mathrm{r}^2 \tag{1.38}$$

If perfect hexagonal arrangement at the interface is assumed, the film density δ_{film} of the unit cell equals the δ_{film} of the whole monolayer and the final expression for the film density becomes [54]:

$$\delta_{film} = \frac{m}{S} = \frac{2\pi}{3\sqrt{3}}\rho r = \frac{\pi}{3\sqrt{3}}\rho D \tag{1.39}$$

where the sphere density ρ can be found in the Langmuir isotherm if the amount of particles (m) spread on the interface and the sphere diameter are known.

1.8 Characterization of self-assembled monolayers

The quality of colloidal films and molecular monolayers has been frequently characterized by different variables such as surface coverage, average domains and Fourier analysis between others. However, all this techniques do not provide a complete idea of the degree of order since they cannot differentiate between the dissimilar kinds of defects existing in the ordered structures. Therefore, to obtain a qualitative analysis, the size of the ordered arrays and the size and type of the defects in the domains should be characterized cooperatively [55]. The two methods usually used to describe accurately the arrangement in a 2D crystal structure is the Delaunay triangulation to identify and classify the structural defects and the pair distribution function to identify the size of the ordered domains.

A Delaunay triangulation is a tessellation of regular polygons between a set of points covering a certain area without overlaps or gaps. The mesh of polygons is formed with triangles limited by the condition that any point of the set of points or any triangle of the triangulation will be found inside of the circumcircle of any other triangle [56]. In the case of study, the vertices of the triangles are the centers of coordinates of the particles. For this reason, a perfect triangular mesh is formed by equilateral triangles where the side length is equal to the particle diameter plus an error of tolerance. Exceeding this distance indicates a defect in the hexagonal array.

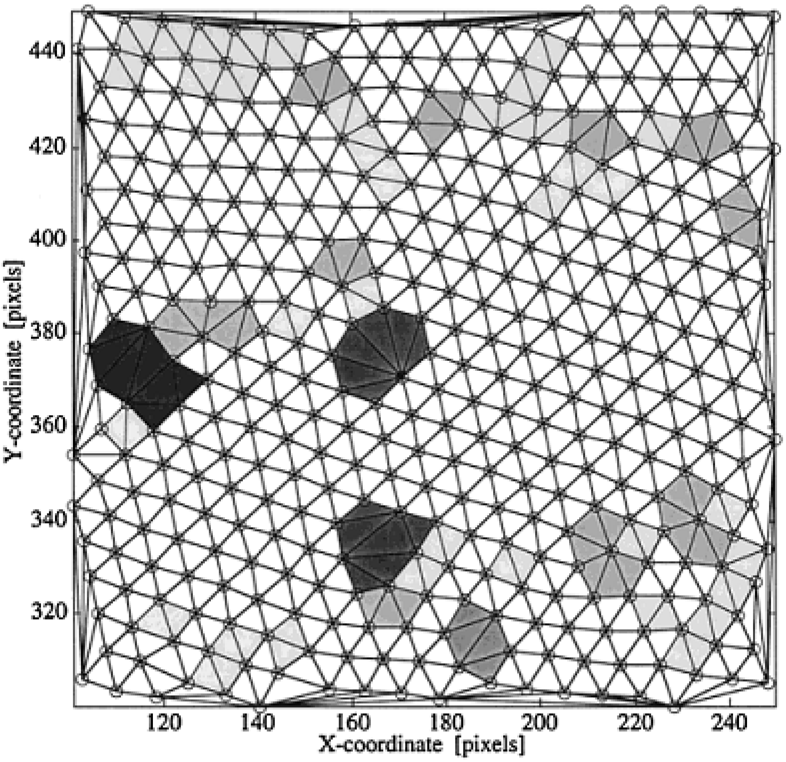

Figure 1.21: *Example of Delaunay triangulation. The vertices of the triangles are the centers of the particles. The grey triangles show the different arrangement of pores and the white-colored triangles show the hexagonal arranged mesh [57].*

The triangulation configuration helps to identify faults and defects in the domains in order to classify them. One triangle enclosing a pore between particles defines the triangular order characteristic of the hexagonal configuration. Two triangles enclosing a pore between particles define a quadrilateral configuration, three triangles enclosing a pore define a stacking fault and four triangles enclosing a pore define a larger stacking fault or a missing particle as depicted in Figure 1.21 [57].

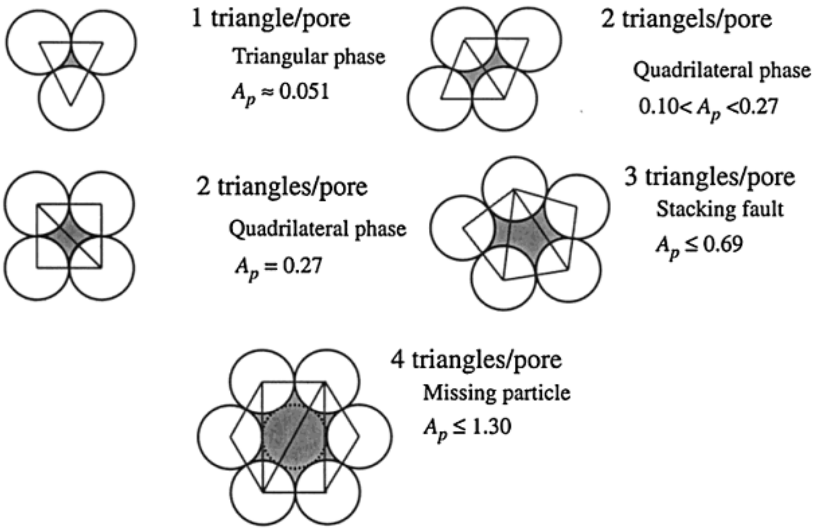

Figure 1.22: *Geometry of the different particle arrangements in a Delaunay Triangulation. The pores are colored gray and* A_p *represents the normalized pore area [57].*

The pair distribution function g(r) provides a quantitative characterization of ordered arrays in 2D colloidal crystals. The particles distribution in a colloidal film, in which the configuration is obtained from the centers of the particles, allows calculating the separation distance between particles to analyze long-range monolayer order. The pair distribution function proceeds selecting a particle from the molecular structure and then counting the number of particles that are found in a ring area within a distance r, r+dr away from the particle. The general procedure is illustrated in Figure 1.23 where the selected particle is colored in red and the particles within the ring area are colored in blue.

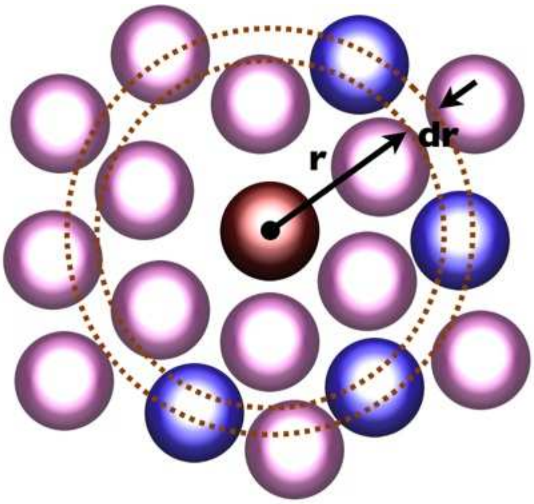

Figure 1.23: *Schematic of the calculating method of the pair distribution [58].*

The pair distribution function calculates de particle density inside the ring area and divide it by the mean particle density of the complete area analyzed. Therefore, the pair distribution calculates how the particle density varies as a function of the distance for a specific selected particle [59]. The 2D pair distribution function is then defined as:

$$g(r) = \frac{1}{N}\sum_{i=1}^{N}\frac{n_i(r)}{C2\pi r\Delta r} \tag{1.40}$$

Where r is the radial distance from the selected particle, Δr is the width of the ring, $n_i(r)$ is the number of particles within the ring area r, r+ Δr, C is the mean particle density in the total image analyzed and N is the total number of particles that contributes to the pair distribution function

Usually for well-ordered structures, the pair distribution functions exhibits many peaks and slow decay confirming the long-range order. The largest peak is normally found at the minimum separation distance of one particle diameter. For radial distances much greater than a particle diameter, the pair distribution function tends to one.

2 Materials and methods

2.1 Materials

This section contains the different chemicals used in this project. The table contains information about the chemical name, lot or batch number and supplier.

Chemicals	**Description**	**Manufacturer**
Acetone	Lot: STBC0099V	Sigma Aldrich
Ammonium hydroxide 30%	Lot: SZBB1390V	Sigma-Aldrich
Ethanol	Lot:15C170514	VWR chemicals
Hydrogen peroxide 30%	-	Sigma-Aldrich
Isopropanol	Lot:SZBE058BV	Sigma Aldrich
LUDOX® HS-40	Lot:07524_029	Sigma Aldrich
Polystyrene microspheres	grafted with poly(acrylic acid)	-
Polystyrene nanospheres	grafted with poly(acrylic acid)	-
Sodium hydroxide	Lot SZBE2520V	Sigma Aldrich
Toluene anhydrous 99.8%	Lot STBF7647V	Sigma Aldrich
Trichloro(1H,1H,2H,2H-perfluorooctyl) silane	Lot MKBN9080V	Sigma Aldrich
(3-Aminopropyl) Trimethoxy-silane	Lot BCBL6126V	Sigma Aldrich

Table 2.1: *List of the different chemicals used during the experimental work*

2.2 Colloidal suspension of silica and polystyrene particles

2.2.1 Silica dispersion

Monodisperse silica particles were obtained from LUDOX® HS-40 colloidal silica 40% wt with a diameter of ~30nm. The LUDOX solution was washed twice with absolute ethanol and centrifuged at 10.000 rpm for 30 min to remove any remaining surfactant. The precipitated silica was resuspended in deionized water, ethanol or a mixture of both in an appropriate concentration ranging from 0.04-4% w/v. 0.1mM Sodium hydroxide was used as solvent in several samples to control pH around 9 to assure high surface charge an electrostatic stabilization.

2.2.2 Polystyrene dispersion

Polystyrene spheres grafted with poly(acrylic acid) in methanol with diameters of ~2μm and ~350nm were kindly supplied by the nanobiotechnology department. The samples were precipitated by centrifugation at 10.000 rpm for 30 min and resuspended in deionized water, ethanol or a mixture of both in an appropriate concentration ranging from 0.05-30%w/v without further purification.

2.2.3 Sizing of micro-and nanospheres

Colloidal particles were characterized by different techniques in order to describe and compare the different method suitability between results. Silica particles were analyzed with Nanoparticle Tracking analysis, NTA, (see appendix A for data report) scanning electron microscopy and direct interpretation from the images obtained in atomic force microscopy. The NTA utilizes a laser beam which gets scattered by the particles in suspension allowing their visualization. A high-sensitivity CMOS camera captures the particle moving in real-time under Brownian motion. The particle concentration analyzed inside the chamber should be diluted to 10^6 - 10^9 particles per milliliter. The speed of motion or diffusion constant of the Brownian motion is related with particle size by using the Stokes-Einstein equation:

$$Dt = \frac{TK_b}{3\pi\eta d} \tag{2.1}$$

Where Dt is the diffusion coefficient, K_b is the Boltzmann's constant, η is the viscosity, T is the temperature and d is the sphere-equivalent hydrodynamic diameter. Consequently the particle diameter can be calculated if the sample temperature and solvent viscosity are known.

Polystyrene particles were analyzed from direct interpretation of AFM images and through statistical analysis of SEM images via the cross-platform image analysis tool ImageJ. (see appendix A for data). The software calculates the particle area by modeling the particles with ellipses and then measuring the pixels occupied. The quality of the image had a clear brightness contrast between the particles and background to set a threshold that allows a distinctive definition and differentiation between them. The expected particle size was ranged between a maximum and a minimum value in order to avoid noise picked from the background that otherwise would be interpreted as very small particles.

2.3 Substrate wetting properties

2.3.1 Substrate and cleaning procedure

Silicon wafers of roughly 1 cm^2 were used as substrate and were cleaned thoroughly to render a hydrophilic surface through one of the following cleaning protocols:

1. The silicon substrates were placed in acetone and sonicated for 5 min in the ultrasonic bath. When finished, the substrates were rinsed firstly with acetone, secondly with Isopropanol and finally blow-drying with nitrogen.

2. Cleaning procedure based on RCA-1. 250 ml of water and 50 ml of 30% ammonium hydroxide was mixed in a beaker and heated until the reaction reached 65ºC. Then 50 ml of 30% hydrogen peroxide was added while the temperature was maintained constant in a final ratio of NH_4OH (30%):H_2O_2(30%):H_2O 1:1:5 at 65ºC. The silicon wafer was soaked in the solution for 15 min. Right after, the silicon substrates were placed in a beaker with DI water and sonicated for 1 min in the ultrasonic bath to remove the reaction residues. The silicon substrate was then blow-drying with nitrogen.

A final UV/ozone treatment was applied to all substrates used in dip-coating and Langmuir-Blodgett methods for 10 min to render a hydrophilic surface whereas some substrates in droplet evaporation method were deliberately untreated to investigate the effects of surface wetting in monolayer formation.

2.3.2 Substrate functionalization

Silicon wafers were functionalized with Trichloro(1H,1H,2H,2H-perfluorooctyl) silane (PFS) and (3-Aminopropyl)Trimethoxy-silane (APTMS) in order to provide different wetting properties in the study of self-assembly monolayers.

Prior surface functionalization, silicon wafers were thoroughly clean via cleaning protocols 1 and 2 and a UV/ ozone treatment applied to render a clean surface without contaminants. The vacuum chamber was dehydrated for 10 min with a Knf lab Laboport model N820.380 pump to remove the air and refilled with Argon. The silicon substrates were then placed on a petri dish inside the vacuum chamber, the system evacuated for 5 minutes and refilled with Argon. This stage previous to surface functionalization promotes the dehydration purge and removes the remaining water on the substrates. A solution of 25% v/v APTMS in Toluene or 25% v/v PFS in Toluene was then introduced to the chamber and the system evacuated for 5 min. A small volume of Argon was introduced into the sealed chamber raising the pressure but kept below the atmospheric pressure to assure an argon atmosphere surrounding the substrates to avoid humidity. The reaction time for the molecules to freely evaporate and condense onto the substrate in case of PFS silanisation was 10h and in case of APTMS silanisation 1h.

2.3.3 Substrate contact angle via static sessile drop method

The wetting properties of the substrates after cleaning procedure one or two were characterized before and after the UV light /ozone treatment on the substrate. The static contact angle measurements were carried out at room temperature in an open atmosphere. The needle and the syringe were cleaned with DI water before running the contact angle experiment. A small drop of ~ 2 mm of diameter was deposited on top of the substrate. In order to avoid shape distortion and vibrations due to droplet impact with the substrate, the needle was placed almost in contact with the bottom of the specimen to supply the liquid and then gently detached from de droplet. The drop was illuminated by a light source and an image of the drop shape was taken with a DMK 23U618 USB 3.0 Monochrome Industrial Camera. The droplet image was analyzed with the freely-available computer software called ImageJ through Brugnara plugin for contact angles before UV/ozone treatment and Low Bon Axisymmetric Drop Shape Analysis (LB-ADSA) by Sage et. al [55] for contact angles after UV/ozone treatment. In the case of APTMS-treated and PFS-treated substrates the droplet image was analyzed by LB-ADSA plugin.

2.4 Methods for production of self-assembled monolayers

2.4.1 Monolayer self-assembly by Droplet Evaporation technique

The colloidal solution was sonicated in an ultrasonic bath for 30 min to ensure that the colloidal particles were fully dispersed. A droplet of the suspension was then deposited over a silicon substrate placed on the bottom of a regular Petri dish used as experimental cell. The Petri dish was covered with the lid and sealed with parafilm to minimize the external air flow. The proper particle concentration and volume spread were chosen depending on the deposition area and on the particle size in order to provide a close-packed monolayer of approximately 1cm^2 after solvent evaporation. The particle/solvent proportion was calculated by finding the number of nano-or microspheres necessary to self-assembly in the required area. The original particle concentration in a colloidal solution is:

$$N = \frac{6w}{\pi\rho\varphi^3}10^{12} \tag{2.2}$$

where N is the particle / ml, w is the concentration of solid particles in grams/ml, ρ is the density of polymer in grams/cm^3, and φ is the diameter of the particles in micrometers. The number of particles necessary to cover the selected area:

$$n_p = \frac{A}{\pi\left(\frac{\varphi}{2}\right)^2} \tag{2.3}$$

where the term in the denominator represent the area occupied per particle. Dividing n_p by an appropriate amount of solvent, the original particle concentration in the colloidal suspension required to form a monolayer expressed in equation 2.2 can be tuned to satisfied equation 2.3. However, the particle concentration deposited on the substrate should not be critical, one or two times higher than the theoretical value calculated also provides good results. Equations 2.2 and 2.3 are also valid for the approximation of particle/solvent proportion in Dip-coating and Langmuir-Blodgett technique.

In the case of APTMS-treated and PFS-treated substrates a preferred volume of deionized water was deposited on the substrate to form a small droplet and on top a volume of polystyrene dispersion was spread at the liquid-air interface. The sufficient concentration to form a full monolayer in the area delimited by the circular base contour of the droplet upon evaporation is calculated by the equations that relate the volume of the droplet spherical shape, the contact angle and the contact base radius [61]:

$$V = \pi R^3 f(\theta) \tag{2.4}$$

$$f(\theta) = \frac{(1-\cos\theta)^2(2+\cos\theta)}{3\sin^3\theta} \tag{2.5}$$

where V is the droplet volume of the spherical shape resting on a horizontal plane, R is the contact base radius and θ the contact angle.

2.4.2 Monolayer self-assembly by Dip-coating technique

The self-assembled monolayers were obtained by dipping a silicon substrate into a colloidal suspension at room temperature. The colloidal solution was sonicated in an ultrasonic bath for 30 min to ensure that the suspension was fully dispersed. A suspension volume of 4mL was poured in a 5 mL beaker to provide enough depth for the substrate to dip in. The solvent used for the colloidal particles was ethanol, water or a mixture of both at different proportions diluted to a definite concentration range between 0.3-3% w/v. The experimental procedure was carried out by means of a Langmuir-Blodgett dipping arm used for the substrate immersion into the suspension. The silicon sample was placed on the holder clip and vertically dipped into the suspension until the substrate was fully covered by the solution. The substrate was left immersed in the solution for 4 min and then lifted up at a constant withdrawal speed between 1-90 mm/min accurately controlled by the computer.

2.4.3 Monolayer self-assembly by Langmuir-Blodgett technique

The self-assembled monolayers were obtained by compression of polystyrene particles suspended on the air/water interface followed by a subsequent transfer of the thin film onto a silicon substrate.

The Langmuir-Blodgett trough and barriers were cleaned with 96% ethanol and the Wilhelmy plate inserted into a hot flame for a few seconds to remove any contaminant from the plate. The trough was filled with DI water as subphase until it reached a couple of millimeters above the edges. The Wilhelmy plate was placed perpendicular to the barriers in the center of the trough making sure that about 1/3 of the plate was immersed in the subphase. Barriers were closed back and forth to check for superficial contaminants which were removed with a pipette over the surface inside the barriers. The surface pressure between initial and final area never increased above 2mN/m.

The Minimicro Langmuir-Blodgett trough is manufactured by KSV instruments. The trough made up of Teflon has dimensions of 195mm length, 50mm width, 4mm depth with a dipping well of 30mm length, 20mm width and 30mm depth. The total available surface area is 8000 mm^2 and total volume is 57mL. Surface pressure is measured through the Wilhelmy plate method with a platinum plate with perimeter of 40.24mm suspended from an electro-balance device. The dipping mechanism consists in a mechanical arm that holds the substrate via a clip-holder and controls the immersion and withdrawal speed in a speed range of 1mm/min to 99mm/min.

Surface pressure-area isotherm of the particle films were obtained from the convenient colloidal suspension volume spread on the interface. The colloidal suspensions of polystyrene were prepared in ethanol at different concentrations (w/v) for particles of ~2μm diameter and particles of ~350nm diameter. The suspensions were ultrasonicated 30 minutes before spreading onto the interface and then an appropriate volume gently deposited. The surface pressure did not exceed 0.5mN/m during deposition. The system was left 30 min for the solvent to evaporate while particles dispersed throughout the initial available area. Particles were compressed at a constant speed of 5mm/min until the selected surface pressure for film transfer was reached. The substrate coating was carried out by using the vertical dipping method at different withdrawal speed in a range of 1mm/min to 90mm/min.

The surface pressure was plotted versus area per particle expressed in cm^2/mg. The initial surface area per particle is $A=A_t/N$, where A_t is the available area with the barriers opened and N the total number of particles. In order to compare experimental results with the expected π-A isotherm, the theoretical area covered by the polystyrene spheres was calculated by equations 1.36 and 1.38 assuming perfect hexagonal close packing and particle density of $1.05g/cm^3$.

In order to quantify the influence of the monolayer disruption in the vertical deposition technique upon substrate withdrawal/dipping, a horizontal transfer was investigated in different hydrophilic and hydrophobic substrates. The polystyrene particles were spread and compressed on the subphase following the same procedure showed previously in vertical Langmuir method. A small hole was made in the monolayer and the substrate immersed inside the subphase. With the help of tweezers, the substrate was gently elevated and the monolayer picked horizontally at constant compression rate. The monolayer was then dried at ambient conditions and compared with the conventional vertical dipping method. Another variation was introduced in some samples to transfer the monolayer by touching the film from the top and then lifted up into the air.

2.4.4 Surface characterization

Atomic Force Microscopy (AFM) and Scanning Electron Microscopy (SEM) are used as complementary techniques for surface investigations.

The AFM equipment used is called NTEGRA Aura model TS-150. The sample was scanned at room temperature in tapping mode with an Olympus OMCL-AC160TS cantilever with a resonance frequency of 300KHz. The images obtained were analyzed and treated with WSxM software.

The SEM equipment used is a field emission Zeiss 1540 XB model with an extra high tension (EHT) of the electron beam of 10kV. All samples were appropriately coated with a conductive film of gold via Edwards Sputter coater model S150B.

2.5 Methods for structural characterization and ordering analysis

In order to find the centers of the particles, SEM images of self-assembled monolayers were examined using ImageJ software. A region of interest was selected to avoid text, labels and undesirable effects. The image was converted to binary grayscale and contrast and brightness were adjusted until the background and the particles were clearly differentiated. Few pixels connecting particles were removed by using the option "watershed". The software guesses the border between particles following the most probable direction and overlays the particles to make them distinguishable. The particles were analyzed by adjusting a threshold in the expected range of particle size to avoid background noise to be interpreted as small particles. The particles at the edges were discarded.

Once the coordinates of the centers were obtained, the first level analysis began by using the Delaunay triangulation method in MATLAB to generate a triangular mesh [62] (see Appendix B1.1) between centers of particles within a region of interest. The MATLAB code was initially based in the work of Leere et al., but it was modified, explained and optimized to fulfill the requirements demanded. The average side deviation L_{i_adev} and average angle deviation φ_{i_adev} were calculated by the expressions proposed by S. Mátéfi-Tempfli et al., [63]:

$$L_{i\_adev} = \frac{1}{3L_{dom}} = \sum_{k=1}^{3} \left| L_{i,k} - L_{dom} \right| \cdot 100\% \tag{2.6}$$

Where L_{dom} is the average side, $L_{i,k}$ is the k'th side of the i'th triangle and

$$\varphi_{i\_adev} = \frac{1}{\pi} \sum_{k=1}^{3} \left| \varphi_{i,k} - \frac{\pi}{3} \right| \cdot 100\% \tag{2.7}$$

where φ_{i_k} is the k'th angle of the i'th triangle. The mesh order was then sorted by green color for well-ordered triangles if both mean side deviation and mean angular deviation are below 10%, by yellow color if only mean side deviation in the triangle is below 10%, by blue color if only the mean angular deviation in the triangles is below 10% and by white color for non-ordered triangles.

Moreover, to further characterize the ordering of the triangular level, a histogram with the distribution of side distances and distribution of angles were calculated together with the total ordered area and a parameter of order in percentage defined by the total well-ordered area (green triangles) divided by the total area analyzed.

The second-level analysis began by finding groups of related triangles inside the well-ordered areas. These groups of triangles form grains where the structural transition between other grains gives rise to triangular deviation and structural defects. The grain analysis was evaluated with a MATLAB code (see Appendix B.1.8). The spreading algorithm for grain growth depends on if the triangle analyzed shares two vertices with a triangle that is already part of the grain as well as fulfills the deviation criterion defined previously (10% deviation). Only grains with at least 6 triangles are considered true grains. The MATLAB code generated a triangulation with groups of triangles distinctively colored to identify different well-ordered regions. For better grain characterization total grain area (hexagonal order) was calculated as well as the largest grain in each ordered domain and the distribution of grains.

The pair distribution function was calculated to characterize the size of the ordered domains in the colloidal crystal film to be compared with the results obtained by the triangulation and grain analysis. The radial distance was normalized with the particle diameter and evaluated with a MATLAB code (see Appendix B1.7).

A color-coded orientation map is also available in the Appendix B1.10 based in the work of Aaron C. et al.,[64], it was modified, polished, explained and optimized to fulfill the requirements demanded. The algorithm is based in the different rotations between grains. The angle of orientation is calculated through the angles formed with a central particle surrounded by six particles in regions with no faults or defects.

An overview of the SEM images collected during the monolayer self-assembly are organized in tables 2.2, 2.3, 2.4 and 2.5 for further analysis and to identify the degree of order, grain size, interparticle distances and angular deviation. The samples are divided depending on the method utilized for 2D crystal fabrication.

Droplet evaporation						
Region	substrate	Φ (µm)	w/v (%)	$V_{dispersion}$ (µl)	$V_{droplet}$ (µl)	MAG.
1	APTMS	2.3	3	1	20	899X
2	Hydrophilic	0.35	10	0.5	-	2.52KX
3	Hydrophilic	0.35	1	1	-	2.04KX
4	Hydrophilic	0.35	1	1	-	2KX

Table 2.2: *SEM images collected of polystyrene self-assembled monolayers via droplet evaporation for structural characterization and analysis.*

Dip-coating							
Region	substrate	Φ (μm)	w/v (%)	$V_{solution}$ (μl)	Immersion time (min)	Withdrawal (mm/min)	MAG.
1	Hydrophilic	2.3	3	4	4	1	498X
2	Hydrophilic	2.3	3	4	4	2	502X

Table 2.3: *SEM images collected of polystyrene self-assembled monolayers via dip-coating for structural characterization and analysis.*

Langmuir-Blodgett								
Region	substrate	Φ (μm)	w/v (%)	V (μl)	Barrier (mm/min)	Π (mN/m)	Upstroke or downstroke (mm/min)	MAG.
1	APTMS	2.3	2.5	206	4	25	1	1.05KX
2	APTMS	2.3	2.5	206	4	25	1	1.01KX
3	APTMS	2.3	2.5	206	4	25	1	1.01KX
4	APTMS	2.3	2.5	206	4	25	3	1.01KX
5	APTMS	2.3	2.5	206	4	25	3	1.01KX
6	APTMS	2.3	2.5	206	4	10	1	1.03KX
7	APTMS	2.3	2.5	206	4	10	1	1.03KX
8	APTMS	2.3	2.5	206	4	15	1	1.02KX
9	APTMS	2.3	2.5	206	4	15	1	1.02KX
10	APTMS	2.3	2.5	206	4	15	1	763X
11	Hydrophilic	2.3	5	102	4	20	1	500X
12	Hydrophilic	2.3	5	102	4	20	5	501X
13	Hydrophilic	2.3	7.5	60	4	20	1	503X

Table 2.4: *SEM images collected of polystyrene self-assembled monolayers via Langmuir-Blodgett for structural characterization and analysis.*

Horizontal transfer							
Region	substrate	Φ (μm)	w/v (%)	V (μl)	Barrier (mm/min)	Π (mN/m)	MAG.
1	APTMS	2.3	2.5	206	4	25	1.04KX
2	APTMS	2.3	2.5	206	4	25	1.04KX
3	APTMS	2.3	2.5	206	4	25	1.04KX
4	Hydrophilic	2.3	2.5	206	4	25	1.04KX
5	Hydrophilic	2.3	2.5	206	4	25	1.04KX
6	PFS	2.3	2.5	206	4	25	1.08KX
7	PFS	2.3	2.5	206	4	25	1.04KX
8	PFS	2.3	2.5	206	4	25	1.04KX
9	PFS	2.3	2.5	206	4	25	1.04KX

Table 2.5: *SEM images collected of polystyrene self-assembled monolayers via Horizontal method for structural characterization and analysis*

3 Results

3.1 Sizing Silica and polystyrene particles

Self-assembly processes depend to a large extent on the physical characteristics of the building blocks that form the system. Shape, size as well as the polydispersity or monodispersity in the colloidal solution have a capital role in the final arrangement and order in the well-structured array. In order to characterize the particle size and size distribution, silica particles were analyzed by Nanoparticle tracking analysis (see Appendix A). The average diameter found was 28 nm with a large range of particles having a diameter ~30nm and a certain degree of polydispersity. The two different polystyrene particles in size used in this master thesis were analyzed by ImageJ through respective images obtained from SEM. Figure 3.1 depicts the two different images of different particle size employed by the software. The images are pretreated in black and white colors to highlight the boundaries between particles and background for increasing the efficiency during software processing. The statistical analysis generates a table with the occupied area per particle which can be consulted in Appendix A.

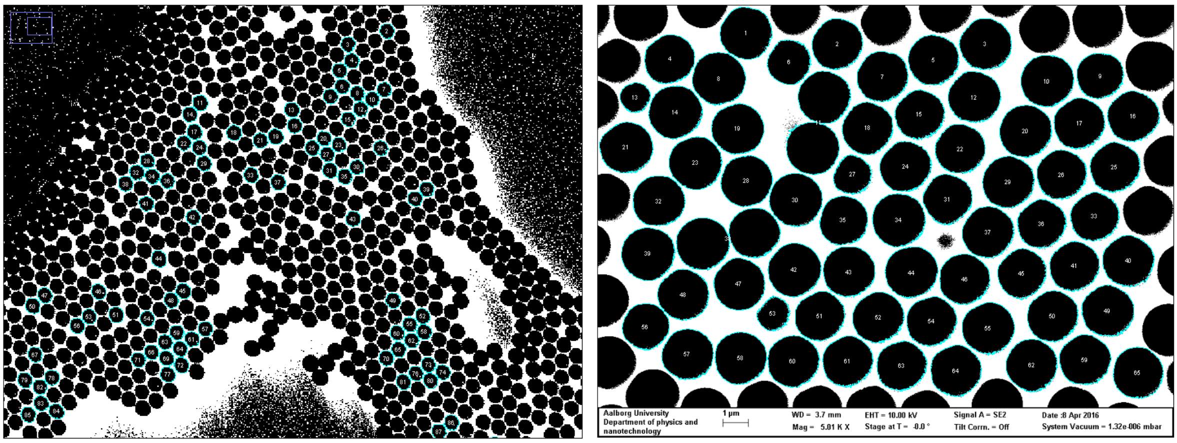

(a) (b)

Figure 3.1: *Statistical analysis of particle size and size distribution by ImageJ. Particles accurately identified for software processing are encircled by a blue line. (a) Polystyrene particles' of ~350nm diameter. (b) Polystyrene particle of ~2µm diameter*

Polystyrene particles in Figure 3.1 (a) resulted with an average diameter of 352.8 nm, a median of 345.7nm and standard deviation of 7.3 nm. Figure 3.1 (b) resulted with an average diameter of 1.994µm, a median of 2.03µm and a standard deviation of 169.9

nm. The polydispersity factor is more pronounced in the latter case and therefore the particle size variability will hinder the order in the course of self-assembly.

3.2 Substrate contact angle via static sessile drop method

The wetting properties of silicon surfaces after cleaning via first o second cleaning procedure before and after UV/ ozone treatment are depicted in the Figure 3.2. The surface energy values provide information on the hydrophobicity and hydrophilicity of the substrate, i.e. the wettability of the surface due to surface contamination. The measurement is carried out right after the drop contacts the surface to avoid advancing contact angle over the dry solid surface implying a change in the contact surface. The contact angles found on the substrate before UV/ozone treatment were 76.1º and 58.7º for cleaning procedure 1 and 2 respectively. The contact angle after UV/ozone cleaning ranges around a magnitude of approximately 10º indicating the high hydrophilicity rendered on the substrate surface.

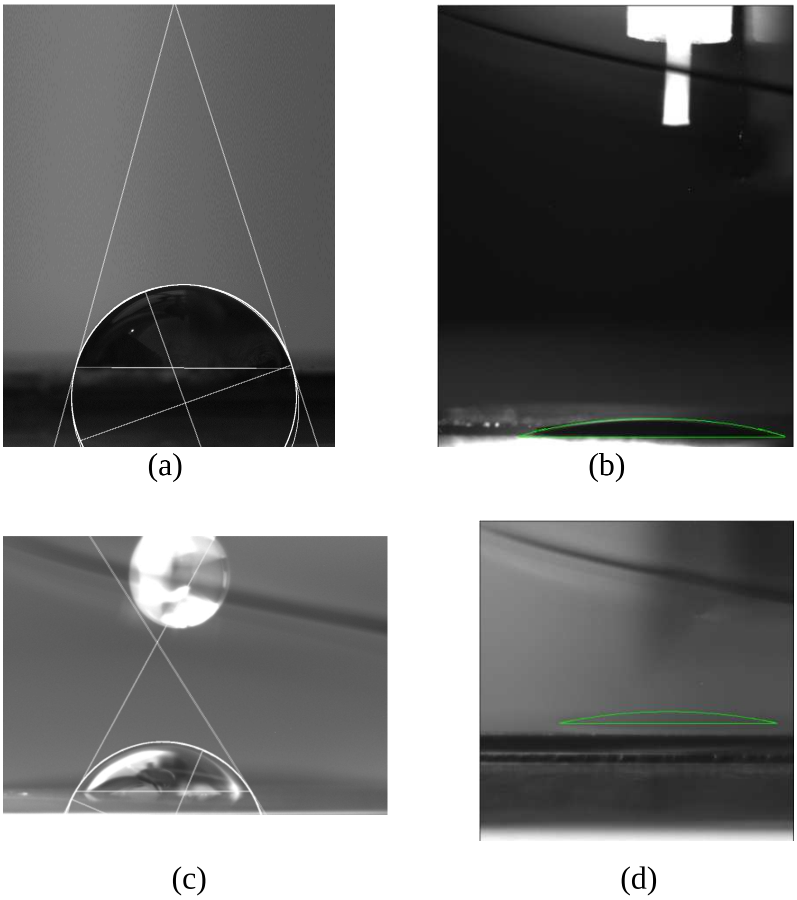

(a) (b)

(c) (d)

Figure 3.2: *Surface contact angle on silicon substrate cleaned via procedure 1 (a)-(b), and via procedure 2 (c)-(d). (a) and (c) represent the contact angle before UV/ozone treatment with a value of 76.1º and 58.7º respectively. (b) and (d) represent the contact angle after UV/ozone treatment with a magnitude of a few degrees.*

The wetting properties of silicon surfaces functionalized with APTMS and PFS are depicted in the Figure 3.3(a) and Figure 3.3(b) respectively. The measurement is carried out right after the drop contacts the surface to avoid advancing contact angle over the dry solid surface implying a change in the contact surface. The contact angles found were 58.5º for silicon substrates functionalized with APTMS and 105.7º for those functionalized with PFS.

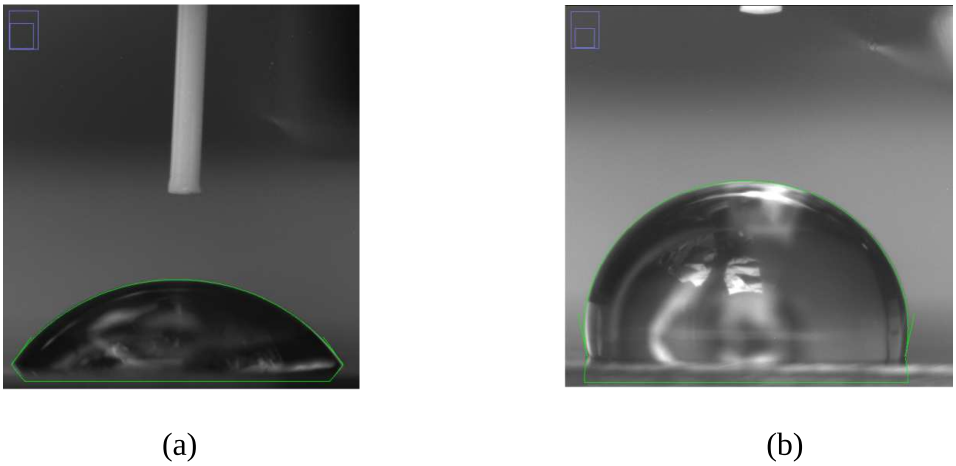
(a) (b)

Figure 3.3: *Surface contact angle on functionalized substrates. (a) APTMS-treated substrate with contact angle of 58.5º (b) PFS-treated substrate with contact angle of 105.7º*

3.3 Monolayer Self-assembly by droplet evaporation.

3.3.1 Silica particles

The deposition process and drying profile of colloidal droplets are subordinated to physical and chemical restrains. For this reason, self-assembled monolayers of silica nanospheres were attempted to form at different concentrations, volumes of deposition, solvents and contact angles. Figure 3.4 presents the resulting patterns of colloidal droplets after droplet evaporation with contact angles larger than 58º. During the drying process the solid particles migrate to the pinned contact line leaving a coffee ring phenomenon. Droplets with higher concentration in ethanol than water in the ethanol-water binary mixture acting as solvent experiment a surface tension decrease with a consequent spherical shape distortion.

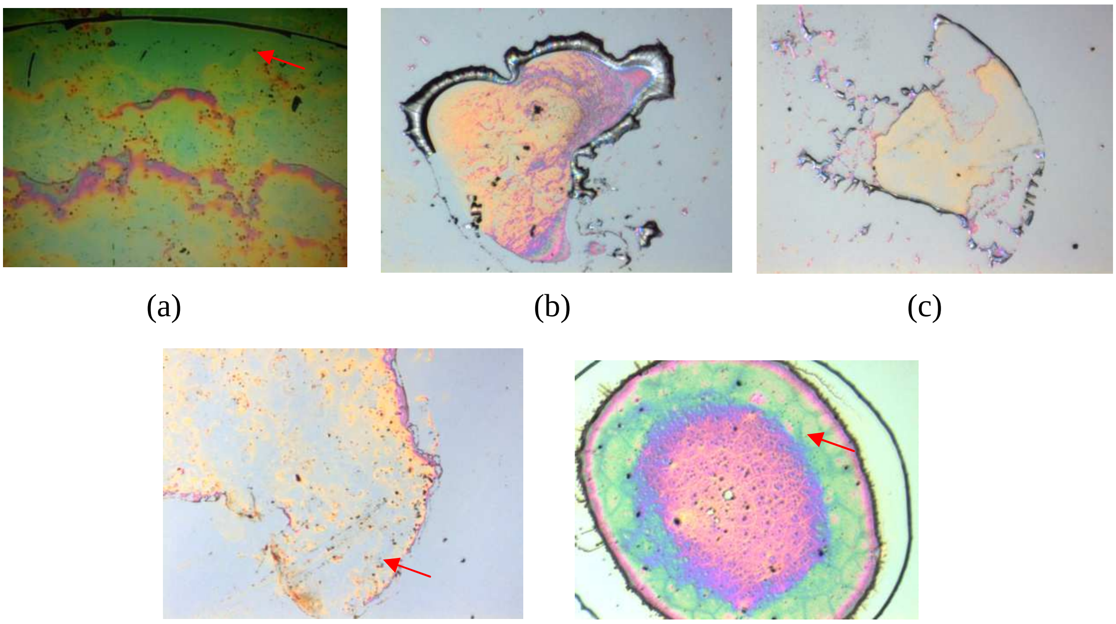

(a) (b) (c)

(d) (e)

Figure 3.4: *Optical images of a ring deposition and irregular structures after evaporation of a sessile colloidal droplet captured with an inspection camera mounted on Opten zoom 125C. Mass concentration, solvent ratio and initial volume in (a-d) images are: (a) 0.4% w/v silica, Ethanol: DI water 1:1, 10μl, (b) 0.4% w/v silica, Ethanol: DI water 2:1, 10μl (c) 0.4% w/v silica, Ethanol: DI water 3:1, 10μl (d) 0.04% w/v silica, Ethanol: DI water 1:1, 10μl, (e) 0.4% w/v silica DI water 1mM NaOH pH 9. The red arrows point at the place where AFM scans were carried out.*

The images shown in the Figure 3.4 illustrate the irregularity of the droplet structure after evaporation process. Further surface characterization at different regions inside the droplet rim is made to determine the molecular structure ordering and organization of the nanospheres in order to verify the existence of self-assembled monolayers. Figure 3.5 shows the nanosphere arrangement close to the ring profile in the vicinity of the contact line where according with theoretical predictions, ordered crystal structures should be easier to be found. However, only agglomeration of silica particles forming multilayers without any periodic pattern is seen.

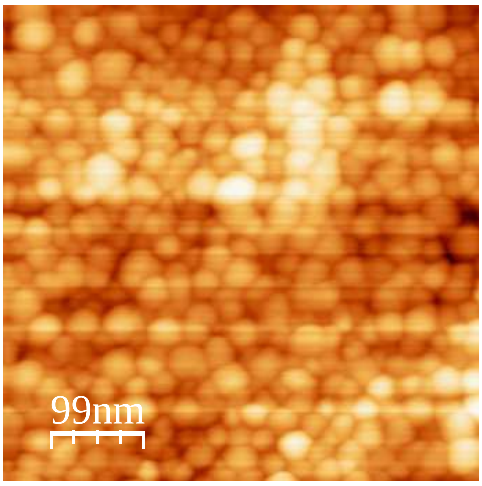

Figure 3.5: *AFM image of colloidal droplet evaporation, 0.4% w/v silica, Ethanol: DI water 1:1 and initial volume of 10µl.The area scanned is shown by the arrow in the figure 3.4(a). No order is found.*

The mass concentration of silica is lowered to provide a more diluted dispersion as a change in the experimental conditions to avoid particle aggregation in a try to look for another preferential deposition rather than the ring-like shape and the subsequent disordered inner area upon droplet evaporation. Figure 3.6 shows the molecular arrangement after droplet deposition of 0.04%w/v silica. Figure 3.6(a) shows several island-like aggregates of colloidal particles. The height profile shown on Figure 3.6(b) demonstrates the particle agglomeration considering that the mean nanosphere diameter is ~30nm.

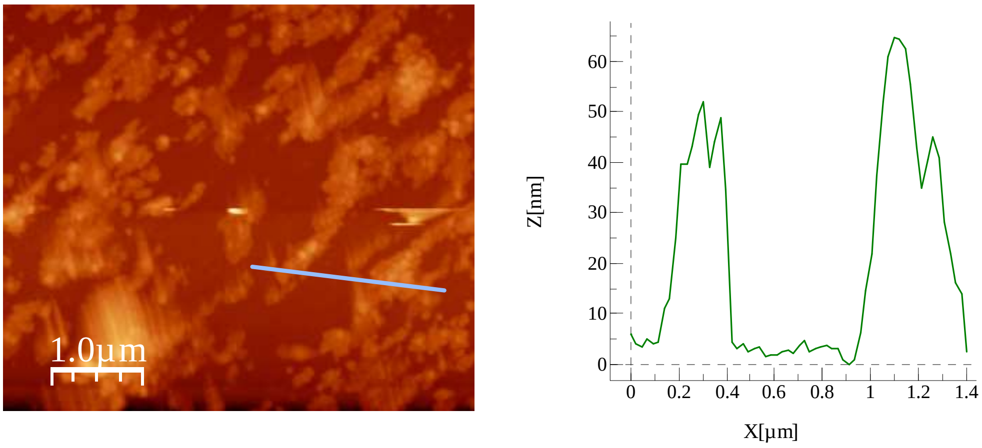

(a) (b)

Figure 3.6: *AFM image of a colloidal droplet evaporation, 0.04% w/v silica, Ethanol: DI water 1:1 and initial volume of 10µl. (a) The blue line marks the height profile shown on (b). The cross-section shows that particles are aggregated in a multilayer. The scannig area corresponds with the area pointed by the arrow in figure 3.4(d).*

Silica particles were dispersed in DI-water 1mM NaOH at pH 9 to enhance electrostatic repulsion between particles with low ion concentration to not interfere with the screening effect by decreasing the Debye length. However, several AFM scans at different areas showed that the molecular adhesion persisted as depicted in Figure 3.7

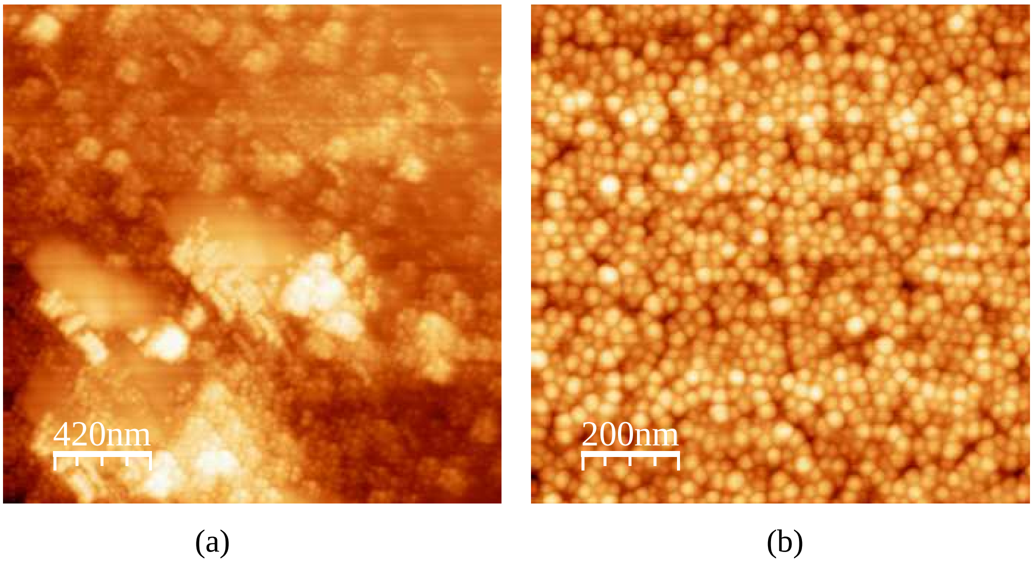

(a) (b)

Figure 3.7: *AFM image of a colloidal droplet evaporation, 0.4% w/v silica, DI water, 1mM NaOH and initial volume of 8μl.(b) The scannig area corresponds with the area pointed for the arrow in figure 3.4(d).*

DI water was used as solvent for the colloidal particles but the adhesion forces still led to molecular disorder after droplet evaporation. Figure 3.8 shows the particle arrangement into large groups of molecular clusters stacked in random configurations.

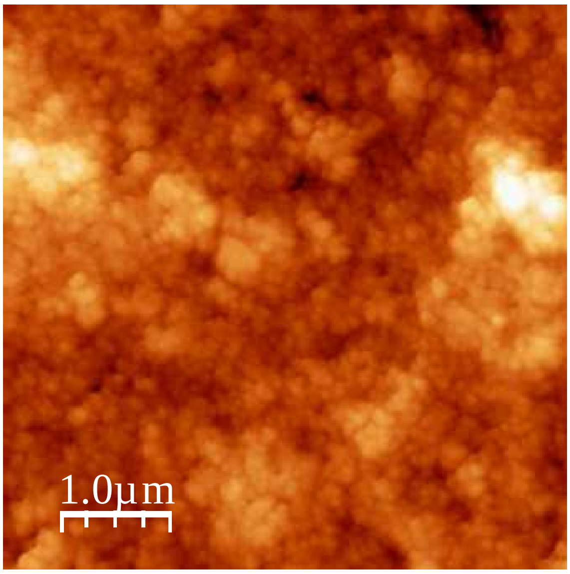

Figure 3.8: *AFM image of a colloidal droplet evaporation, 1% w/v silica, DI water, initial volume of 4.5μl.*

Wetting properties of silicon substrates for monolayer self-assembly were further analyzed by applying a UV/ozone treatment after cleaning procedure 1 or 2. The silicon substrate was rendered with an increased hydrophilicity quantified by the sessile contact angle method after droplet deposition. The final contact angle of a few degrees facilitates the droplet spreading all over the substrate and modifies the convective flow which is clearly dependent on the wetting properties. Different silica concentrations were suspended in DI water with different ion concentration, ethanol or mixture of both as studied before. However, neither monolayers nor well-defined self-assembled structures were found; only isolated areas after droplet evaporation appeared to provide some sort of small order.

Figure 3.9 shows the arrangement of silica nanospheres on a more wettable substrate due to contact angle reduction. As a result, more ordered monolayers and bilayers are found. However, the close-up of Figure 3.9(c) indicates that the monolayer is poorly arranged in a defined pattern showing vacancies and strong adhesion forces between neighboring particles as it is inferred from the height profile shown in Figure 3.9(d).

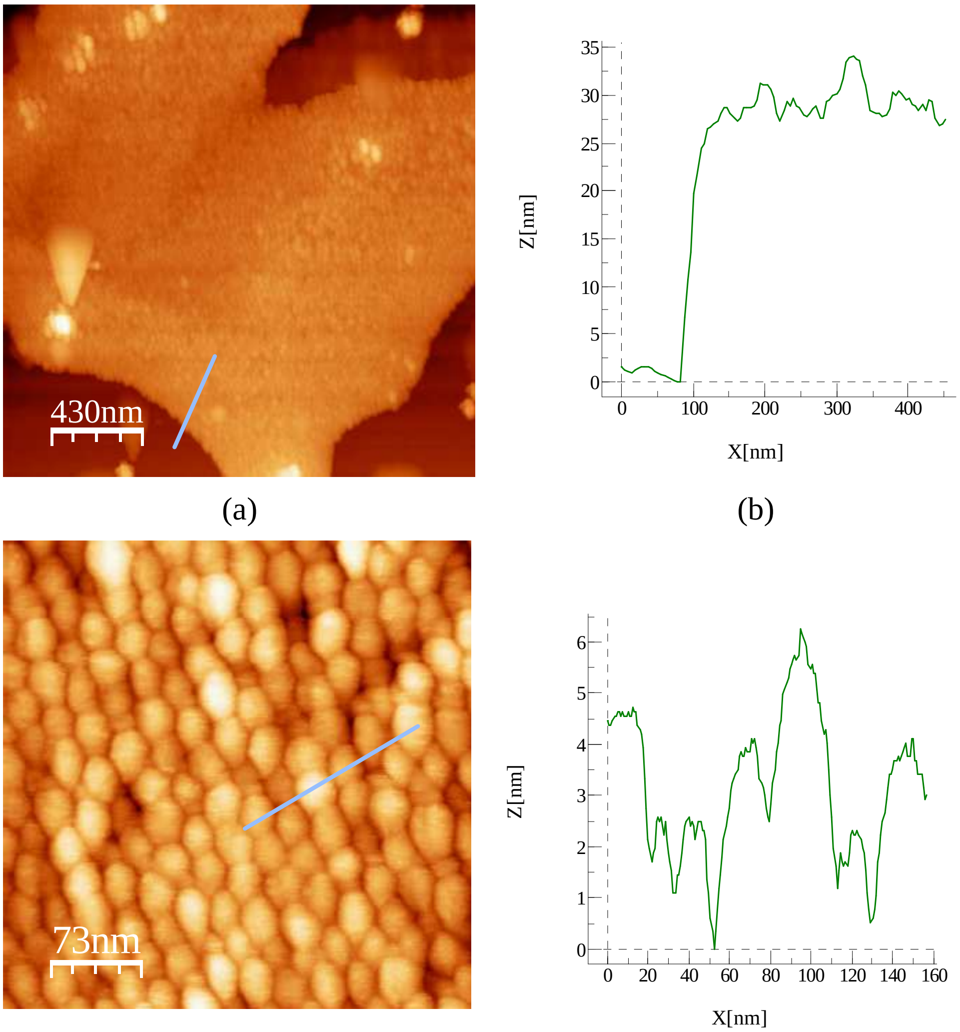

(a) (b)

(c) (d)

Figure 3.9: *AFM images of a colloidal droplet evaporation, 1% w/v silica, DI water, deposition volume of 1μl. (a) Large layer of particles found close to the ring-like structure.The line marks the height profile shown on (b) The height profile of ~30nm indicates some case of monolayer organization. (c) Close-up of the layer shown in (a). Silica nanospheres are more ordered without showing a clear pattern. The line marks the height profile shown on (d). The disorganization of particles in the monolayer is clarifed by the irregularity on height profile.*

Figure 3.10 shows the effect of using a solvent mixture of DI water and ethanol to try to avoid agglomeration resulting in a well-disperesed silica. However, the particles still adhered each other forming stripes and increassing the presence of empty areas between disordered groups of particles. Figure 3.10 (b) shows in more detailed the non-well-structured silica particles and the multilayered arrangement.

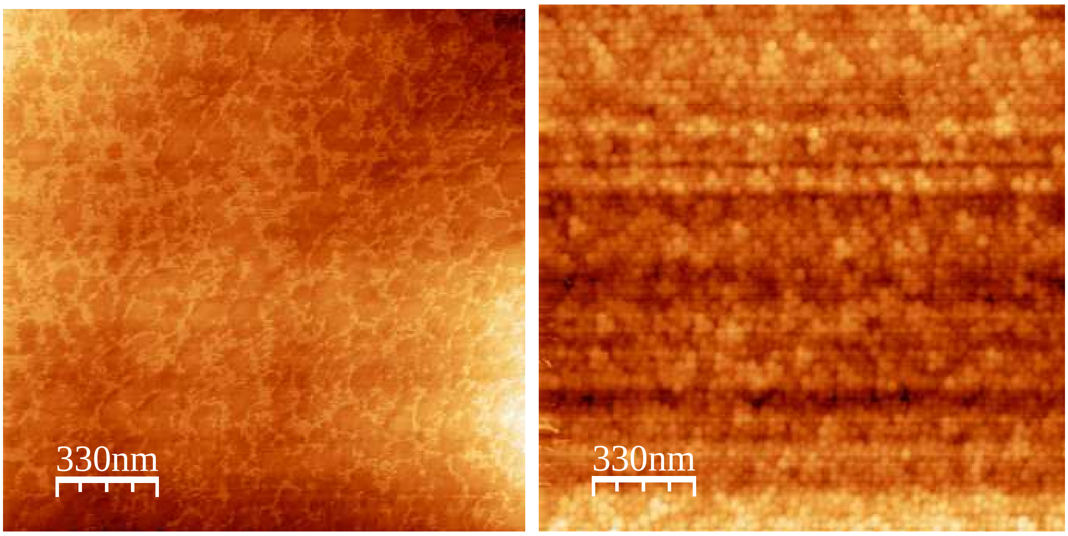

Figure 3.10: *4% w/v silica AFM image of colloidal droplet evaporation, 0.04% w/v silica, Ethanol: DI water 1:1 and initial volume of 10μl.*

3.3.2 Polystyrene particles

Hydrophilic substrate

Fabrication of 2D crystals from polystyrene spheres was carried out by preparing a colloidal suspension of poly(acrylic acid)-grafted polystyrene diluted in DI water without further purification. The contact angle of the watery suspension onto the substrate surface was close to zero. The degree of order in the self-assembled monolayer from polystyrene particles with diameter of ~2μm (PS_2) were first compared at different concentrations of 30%, 15% and 7% w/v with an initial volume of 1μl for the first two colloidal suspensions and 1.5μl for the last one as it is shown in Figure 3.11. Figure 3.11(a) and mostly Figure 3.11(b) provided the best results in monolayer fabrication with PS_2 particles. Although, in both cases, the monolayer arrays presented different oriented crystal domains together with grain boundaries, more cracks and vacancies are located in Figure 3.11(a). Figure 3.11(b) particularly yields larger well-defined orientations and long-range order with regular hexagonal arrangement as can be seen in more detail in Figure 3.11(c). When particle concentration in the suspension is further decreased, polystyrene particles are more loosely packed resulting in less order over the substrate coverage and worst packing ratio. Figure 3.11(d) shows the particle ordering affected by the decrease of PS_2 concentration in the deposited droplet.

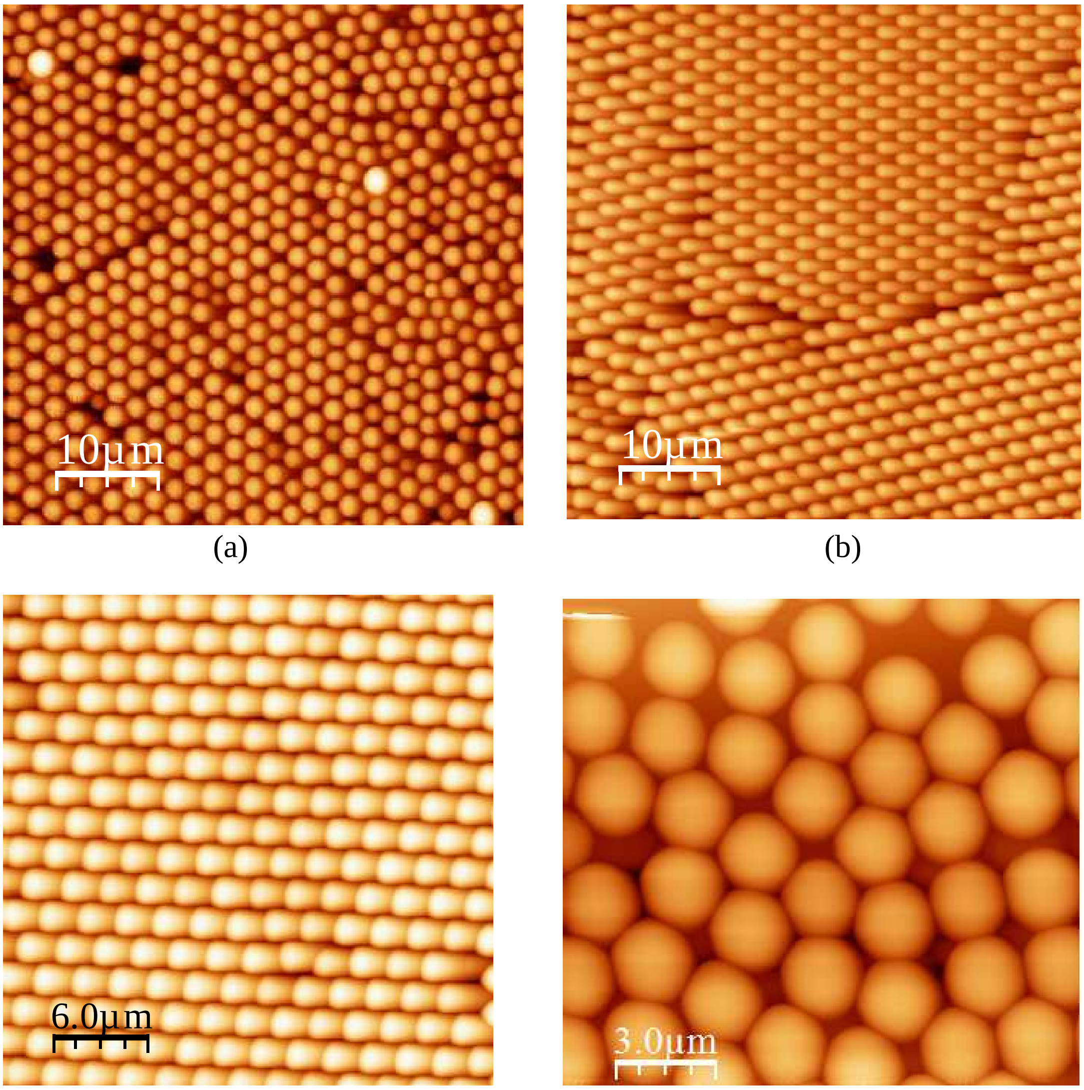

(a) (b)

(c) (d)

Figure 3.11*: AFM images of self-assembled monolayers with particle diameter of ~2μm (a) 30% w/v polystyrene in DI water with initial volume of 1ul, (b) 15% w/v polystyrene in DI water with initial volume of 1μl (c) A close-up resolution of (b), (d) 7% w/v polystyrene in DI water with initial volume of 1,5μl. The molecular arrangement was diminished for the highest and the lowest particle concentration.*

Patterned structures and morphology of the polystyrene monolayers were also examined by scanning electron microscopy. Low-magnification is used to characterize self-assembled structures over wide areas whereas high-magnification is used to observe in more detail the spheres arrangement. Figure 3.12 shows a series of SEM images to determine the long-range ordering of the polystyrene particles. Figure 3.12(a) illustrates a monolayer microstructure formed by small regions of hexagonal order separated by multiple-line defects. It is also appreciated particles with large disparity in diameter and a global lack of homogeneity since polydispersity affects the monolayer packing. Figure 3.12(b) shows a fraction of the ring formation after the drying process at the droplet edge. The piling of layers due to an excessive particle flux is progressive; the particle aggregation and accumulation pass from multilayer formation in the ring-like shape to monolayer formation in the inner part. Decreasing the volume deposited gave rise to short-range ordering between concentric rings as seen in Figure 3.12(c). During the drying time, the droplet has shrunk and the contact angle has receded leaving the characteristic multi-ring structure. The monolayer between two concentric rings is shown in more detailed in Figure 3.12(d) where defects and short-range are better appreciated.

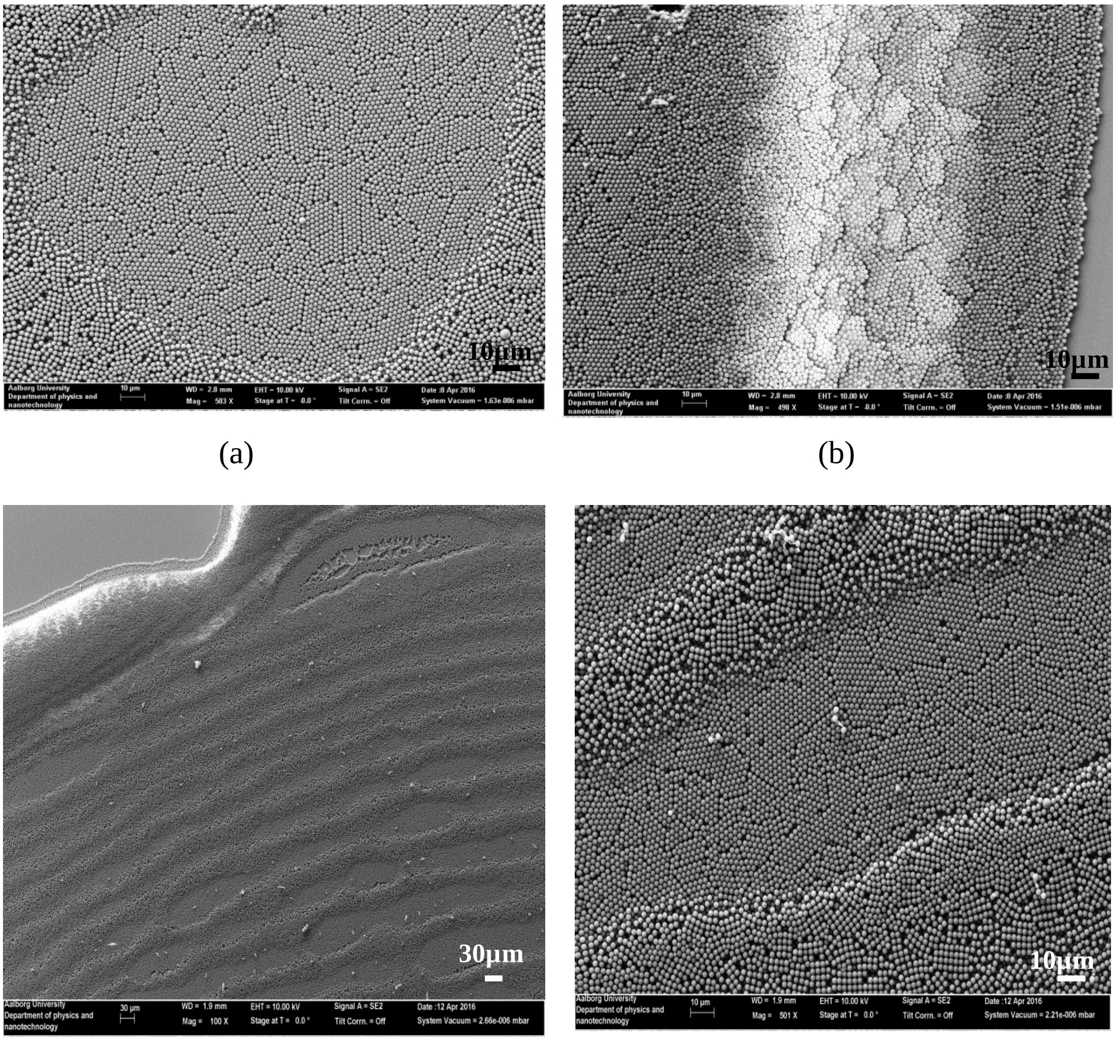

(a) (b)

(c) (d)

Figure 3.12: *SEM images of self-assembled colloidal polystyrene with particle diameter of ~2µm. (a) Self-assembled monolayer at 30% w/v in DI water with initial volume of 1ul 0.5K magnification (b) Fraction of the Ring-like shape formed around the particle assembly, 0.5K magnification, (c)30% w/v in DI water with initial volume of 0.1µl 0.1K magnification (d) A close-up resolution of (c) 0.5K magnification .*

Polystyrene particles with diameter of ~350nm (PS_{350}) at concentrations of 10% w/v initial volume of 1µl and 1% w/v initial volume of 1.5µl are shown in Figure 3.13. The monolayers obtained were denser than in case of PS_2. Figure 3.13(a) and (b) show a densely-packed monolayer in which some defects across both layers can be appreciated. Line defects, vacancies and a combination of both due to accumulation of vacancies are discerned along the monolayers. Additionally, a grain boundary is found in the upper-right corner of Figure 3.13(b). In any case, a closer insight into other areas of the same monolayer still provides large and well-ordered arrangement with hexagonal packing. The height profile depicted in Figure 3.123(d) shows the increment in height between the substrate and the particle arrangement resulting in a difference of one molecular diameter and suggesting the single monolayer formation.

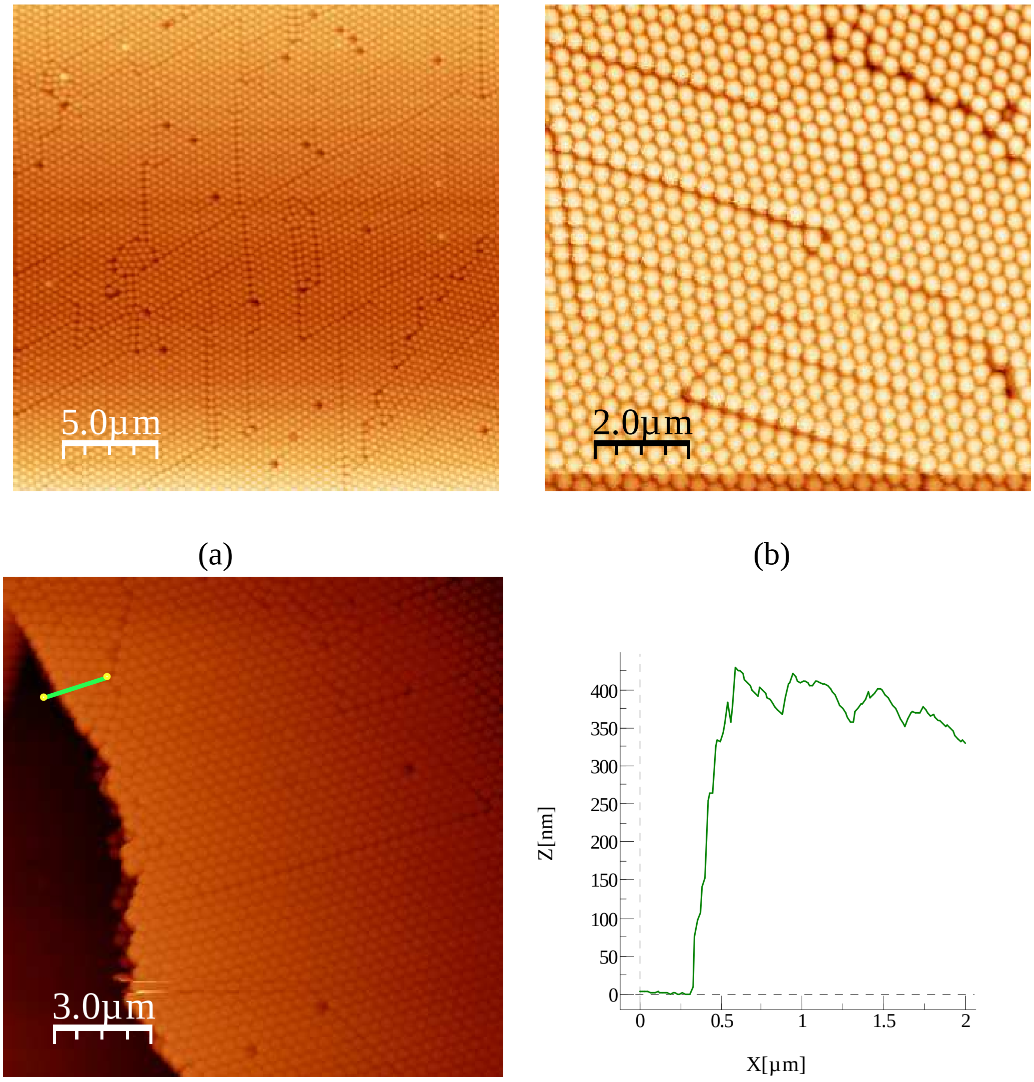

(a) (b)

(c) (d)

Figure 3.13: *AFM images of self-assembled monolayers with particle diameter of ~350nm (a) 10% w/v in DI water with initial volume of 0.5ul, (b) 1% w/v in DI water with initial volume of 2µl (c) A close-up of the image shown in (a), the line marks the height profile shown in (d). The cross-section highlights the difference in height between the substrate and the particle arrangement showing that particle assembly is formed in a monolayer structure.*

SEM images of polystyrene colloidal particles shown in Figure 3.14 confirm the large monolayer arrangement and the hexagonally packed structure. However, the particle array is divided in different domains with structural defects such as line defects, vacancies and grain boundaries as illustrated in the figure below. Figure 3.14(c) shows a self-assembled monolayer from a droplet 10% less concentrated and 4% more volume deposited than in Figure 3.14(a). Both cases in figure 3.14 show better packing with the monodispersed PS_{350} than with the more polydispersed PS_2.

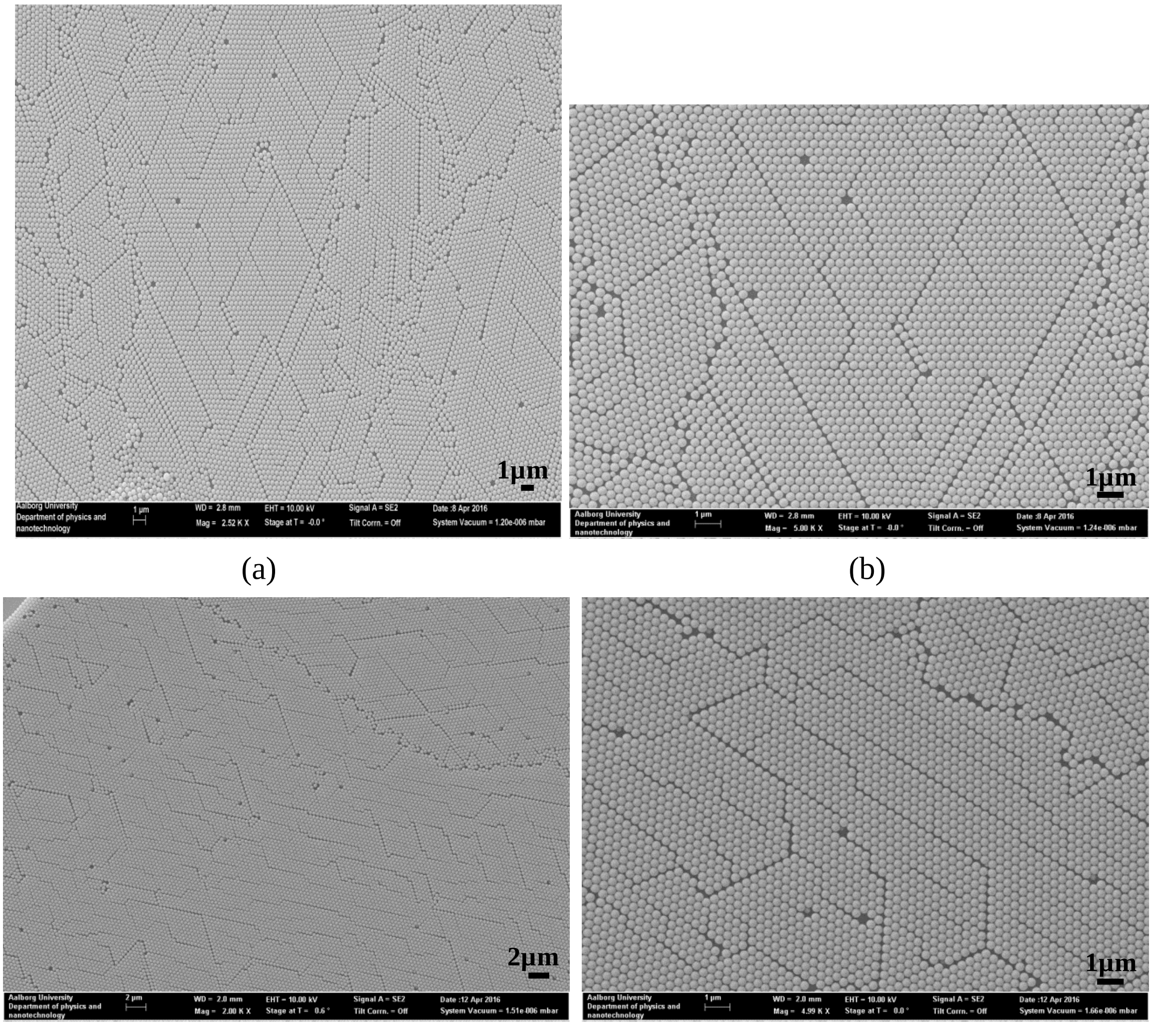

(a) (b)

(c) (d)

Figure 3.14: *SEM images of self-assembled monolayers with particle diameter of ~350nm (a) 10% w/v in DI water with initial volume of 0.5ul, 2.52K magnification, (b) close-up of image shown in (a) 5K magnification, (c) 1% w/v in DI water with initial volume of 2µl, 2K magnification, (d) close-up of (c) 5K magnification.*

APTMS-treated substrate

Self-assembled monolayers of polystyrene micro-or nanospheres were attempted to form by depositing a colloidal suspension of poly(acrylic acid)-grafted polystyrene in ethanol without further purification on top of a deionized water droplet. The contact angle of the water-drop on the substrate was ~ 60º. Different suspension concentration and volumes spread on top of the water-drop were varied to analyze the influence of these variables into the system. A wide representation of the structural patterns obtained with polystyrene particles of ~2μm diameter are summarized by the results obtained at a concentration of 3 % w/v polystyrene and volumes of 2.5µl and 1µl in Figure 3.15. Figure 3.15(a) shows the coffee ring formation at the edge of the droplet as well as particles clusters accumulating in different patterns. The close-up image of Figure 3.15(a) shows the variety of structures formed after droplet evaporation. These amorphous structures enhanced by the opposition between receding contact line and particle deposition were minimized reducing the particle concentration as shown in Figure 3.15(c) and (d). However, the particle arrangement was not compact and the monolayer continuity split in many areas alternating small domains of hexagonal order with empty areas and particle agglomeration. The low degree of order was obtained despite the different concentrations and the suspension volume used.

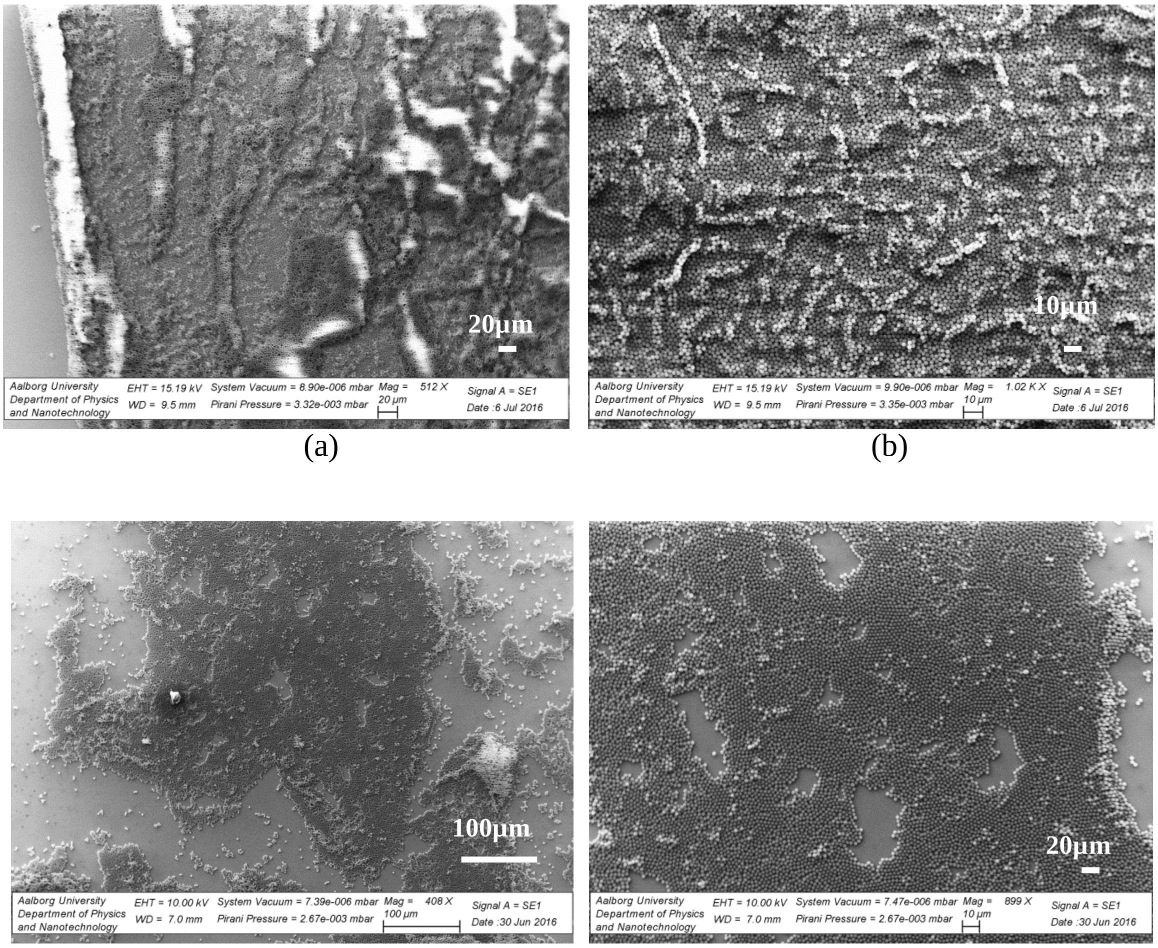

(a) (b)

(b) (c)

Figure 3.15: *self-assembled monolayers with particle diameter of ~2μm on a substrate surface modified with APTMS. (a) 2.5μl of 3 % w/v polystyrene in ethanol deposited over a deionized water droplet of 20μl 0.5K magnification, (b) close-up of image shown in (a) 1K magnification, (c) 1μl of 3 % w/v polystyrene in ethanol deposited over a deionized water droplet of 20μl 0.4K magnification, (d) close-up of (c) 0.9K magnification.*

Polystyrene particles with diameter of ~350nm deposited over a initial water droplet of 20µl at concentration of 1% w/v with a volume of the suspension of 3µl and 2µl are shown in Figure 3.16(a) and Figure 3.16(b) respectively. The deposited nanospheres in a coffee-like structure with clumps of particles in the interior or groups of small isolated islands of particles with may voids and poor arrangement are evidences of an irregular process of mass distribution.

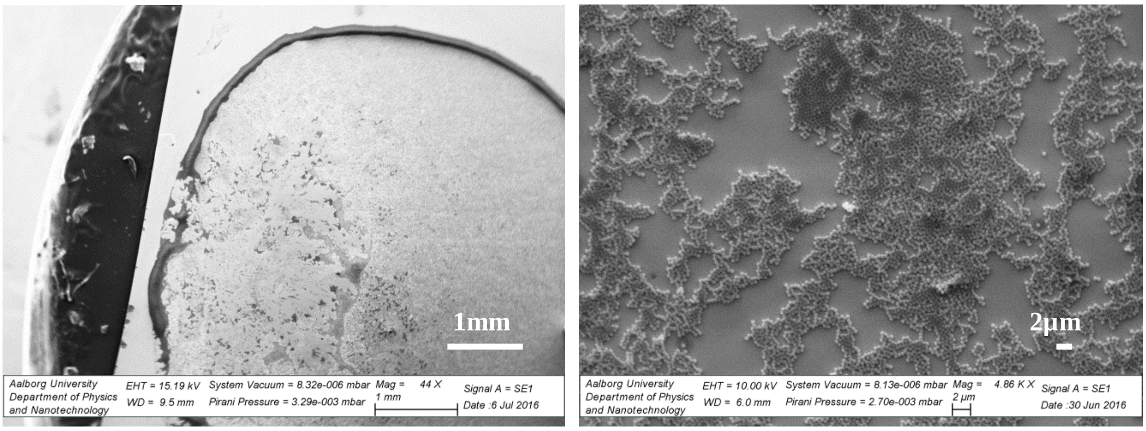

(a) (b)

Figure 3.16: *self-assembled monolayers with particle diameter of ~350nm on a substrate surface modified with APTMS. (a) 3µl of 1 % w/v polystyrene in ethanol deposited over a deionized water droplet of 20µl 0.044K magnification, (b) 2µl of 1 % w/v polystyrene in ethanol deposited over a deionized water droplet of 20µl 0.468K magnification.*

PFS-treated substrate

Nanoparticle self-assembly of poly(acrylic acid)-grafted polystyrene were assayed on a hydrophobic substrate treated with PFS by depositing PS_2 particles in the liquid-air interface as has been reported in the previous section. The contact angle of the water-drop on the substrate was ~ 100º. Different volumes of 3% w/v polystyrene dispersion were spread on a deionized water droplet of 20µl. Figure 3.17 (a) shows a heterogeneous solid deposition in a kind of multiple-ring structure with a concentrated particle distribution in the interior area. The red arrows indicate the trace of particles left behind during the evaporation process. Therefore the pinning-depinning behavior during droplet evaporation gave rise to the characteristic ring formation every time that the droplet receded. The Figure 3.17 (b) presents in more detail the absence of both hexagonal order and monolayer structure, and the presence of ring-like structures which became smaller as the size of droplet progressively decreased during evaporation. The final conformation is an agglomeration of particles in multilayers or other patterns with no specific order as shown in Figure 3.17(c).

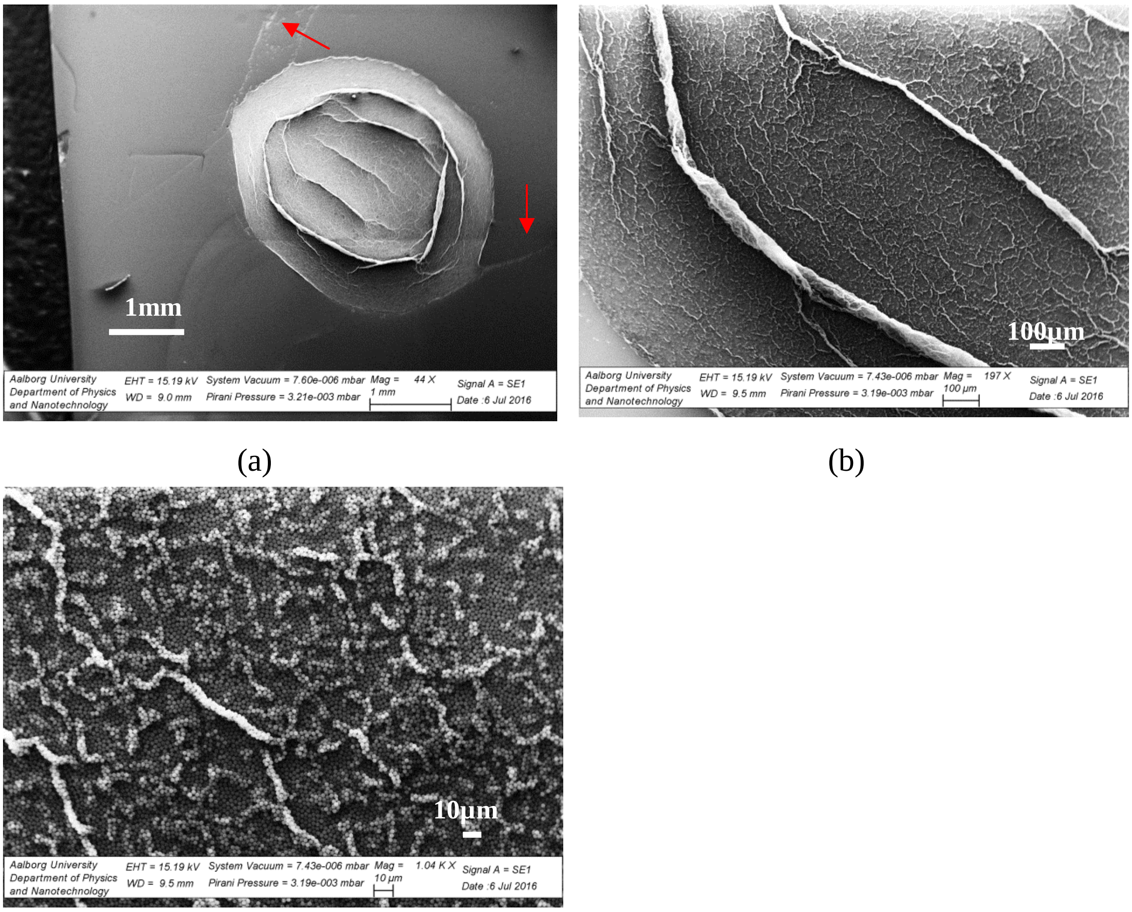

(a) (b)

(c)

Figure 3.17: *self-assembled monolayers with particle diameter of ~2µm on a substrate surface modified with PFS. (a) 2.5µl of 3 % w/v polystyrene in ethanol deposited over a deionized water droplet of 20µl 0.5K magnification, (b) close-up of image shown in (a) 1K magnification, (c) 1µl of 3 % w/v polystyrene in ethanol deposited over a deionized water droplet of 20µl 0.4K magnification, (d) close-up of (c) 0.9K magnification*

3.4 Monolayer Self-assembly by dip-coating

The influence of colloidal particle concentration, withdrawal speed and solvent properties are the main factors investigated for the formation process of well-ordered arrangements. The hexagonal closely packed structures do not cover the whole available area over the substrate since multilayers, loosely packed formations, aggregates or stripes are also found to a greater or lesser extent depending on the variables studied. All the substrates were submerged in a volume of 4ml of colloidal solution with a maximum immersion depth of ~0.8 cm.

Figure 3.18 shows the colloidal self-assembly by dip-coating process in a 3% w/v polystyrene suspension of ~2µm diameter with ethanol/water 1:1 mixture. The substrate remained immersed in the solution for 4 min and then withdrew at a lifting speed of 1mm/min. A regular structure with periodic hexagonal configuration is shown. The vacancy height of around half particle diameter measured in Figure 3.18(b) could suggest that the assembly has been arranged in a multilayer structure.

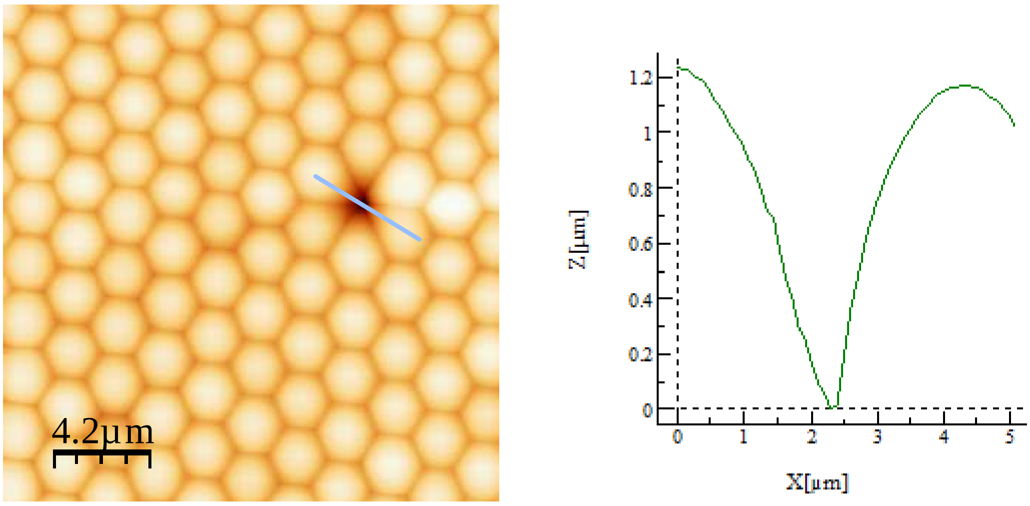

(a) (b)

Figure 3.18: *(a) Closely packed hexagonal assembly with particle diameter of ~2.µm immersed 4 min in 3% w/v polystyrene suspension in a volume ratio Ethanol:DI water 1:1 with withdrawal speed of 1mm/min. The line marks the height profile shonw on (b). The cross-section measures the vacancy height found in the well-packed particle arrangement.*

The influence in the rate of polystyrene particles coverage over the substrate and the degree of well ordered arrangement are evaluated by series of withdrawal speed increments. The increase of withdrawal speed to 2mm/min at the same conditions than before is depicted in figure 3.19(a). An improved order characterized by larger areas and well define periodic structures was achieved although some defects and voices were still found. At a higher withdrawal speed of 10 mm/min the order began to decrease together with the observation of an increase in multilayer phenomena as illustrated in Figure 3.19(b). The self-assembly monolayer consists in narrow stripes with more structural defects such as line defects and voids caused by a more loosely packed arrangement.

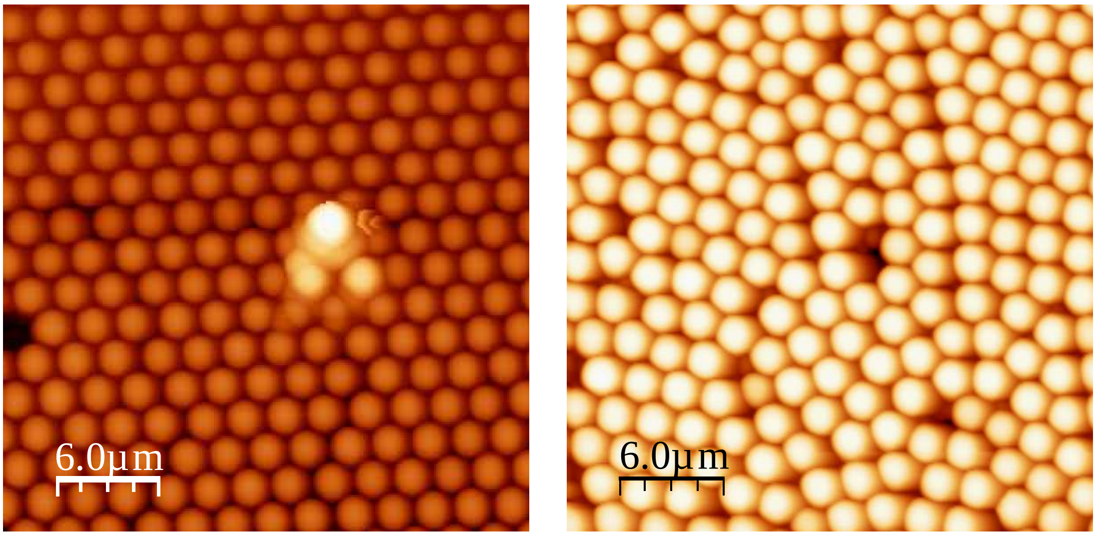

(a) (b)

Figure 3.19: *Self-assembled polystyrene particles with diameter of ~2.µm immersed 4 min in 3% w/v suspension in a volume ratio Ethanol:DI water 1:1. (a) Withdrawal speed of 2mm/min. (b) withdrawal speed of 10 mm/min*

The structural characterization of self-assembled polystyrene microspheres observed by SEM corroborates the similar results found at low withdrawal speed together with the disorder increase at high withdrawal speed than AFM images in Figure 3.19. Long-ordered monolayer and substrate coverage are shown in Figure 3.20(a) and (b). However, the monolayer alternates well-ordered arrangements with empty areas suggesting that more tight compression is required to achieve longer symmetrical hexagonal formation. More ordered close-packed monolayer is found at withdrawal speed of 2mm/min in Figure 3.20(d). Particles are more tightly assembled with larger hexagonal domains but with some line defects as well. The monolayer rupture leads to a scattered pattern with particles distributed within stripes and small islands as seen in Figure 3.20(c). At a high lifting speed of 10mm/min, the self-assembly process increased randomness with dispersed monolayers and disordered bilayers since the too fast speed surpassed the order provided by the capillary regime as shown in Figure 3.20(e) and (f).

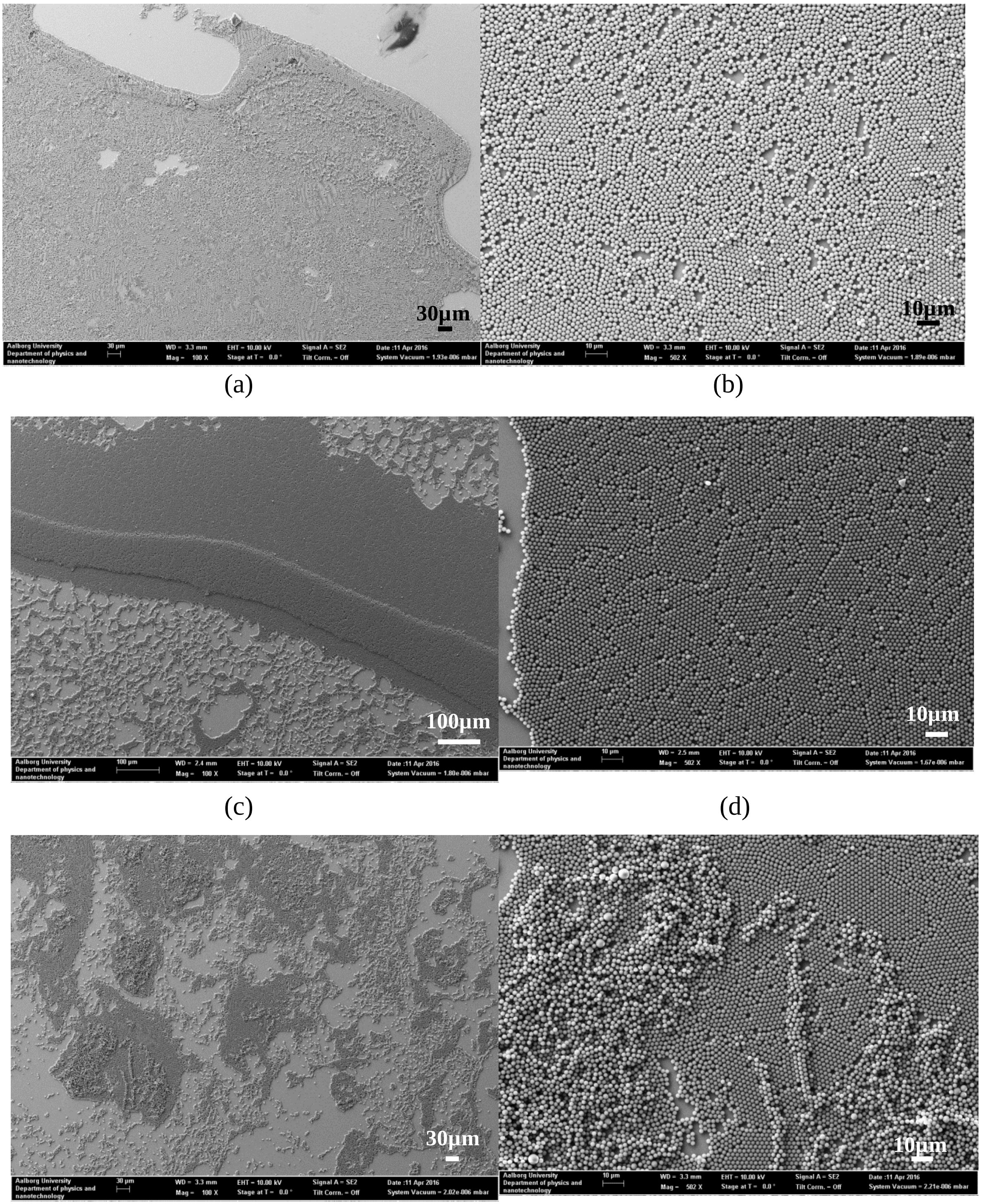

(a) (b)

(c) (d)

(e) (f)

Figure 3.20: *Self-assembled polystyrene particles with diameter of ~2.µm immersed 4 min in 3% w/v suspension in a volume ratio Ethanol:DI water 1:1. (a) and (b) Withdrawal speed of 1mm/min. and 0.1K and 0.5K magnification respectively, (c) and (d) withdrawal speed of 2 mm/min and 0.1K and 0.5K magnification respectively, (e) and (f) Withdrawal speed of 10mm/min and 0.1K and 0.5K magnification respectively*

The surface coating by an ordered self-assembled structure is also apparently dependent of the concentration solution where the substrate is immersed. For this reason, the next variable under study was the particle concentration in the colloidal suspension. Figure 3.21 shows the self-assembled PS_2 immersed 4 min in a 0.3% w/v suspension in a volume ratio Ethanol:DI water 1:1. At this low concentration, in case of 7 mm/min withdrawal speed as shown in Figure 3.21(a), the polystyrene particles are adhered to a narrow region of the substrate, with loosely-packed order and much less surface coverage compared to the previous experimental work done. To further investigate the lifting speed influence at low concentration suspension, the withdrawal speed was increased till 90mm/min. The particle coverage at this high speed is also increased on the surface although the degree of order in the scattered self-assembled regions is found quite similar according to AFM images. Figure 3.21(b) shows an ordered area on top of the image with some loss of order across the scanned sample due to particle polydispersity by which worst packing effect around smaller particles was introduced.

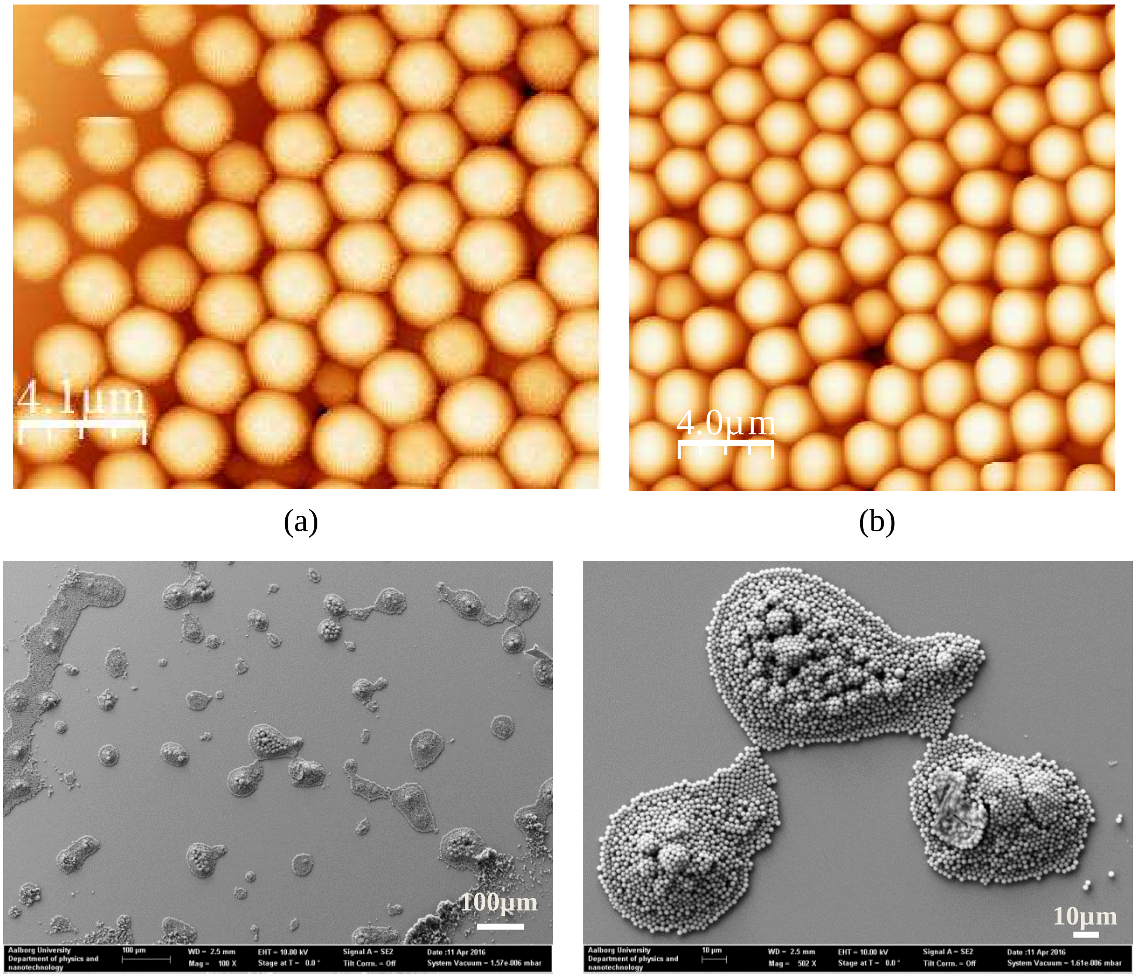

(a) (b)

(c) (d)

Figure 3.21: *Self-assembled polystyrene particles with diameter of ~2.µm immersed 4 min in 0.3% w/v suspension in a volume ratio Ethanol:DI water 1:1. (a) AFM image at withdrawal speed of 7mm/min, (b) AFM image at withdrawal speed of 90 mm/min, (c) SEM image at withdrawal speed of 90mm/min, 0.1K magnification, (d) Close-up image of (c) at 0.5K magnification*

On the contrary, SEM images at withdrawal speed of 90mm/min revealed that in Figure 3.21(c) and (d) no monolayer was formed and the increase in particle concentration over the substrate was arranged in 3D scattered structures that probably responded to the predominant role of viscous drag forces in material deposition at high speeds rather than the evaporation-induced regime.

Monolayer self-assembly by dip-coating was also investigated in polystyrene particles with diameter of ~350nm at different withdrawal speed. Hexagonal order is seen in figure 3.22 within a range of few microns. However, the degree of disorder is directly proportional to the withdrawal speed increase. Figure 3.22(a) shows a central defect line while in Figure 3.22(b) the number of line defects including particle vacancies rises considerably. Lastly, at the highest withdrawal speed, 10mm/min a sub-monolayer is appreciated in Figure 3.22(c). The loss of order at short-range showed by AFM images induces to expect small monolayer extension.

To determine the long-range ordering of the crystal structure, SEM images were taken in the three cases. In Figure 3.23 all samples showed low surface coverage providing only well-ordered monolayers at very small areas. Figure 3.23(a) shows more surface coverage of polystyrene nanospheres but also bilayers and multilayers are found. Figure 3.23(b) shows a not-well compacted stripe and its rupture into small islands. The last SEM image at 10mm/min withdrawal speed is depicted in Figure 3.23(c) where only very small regions of monolayers are distinguished in the whole substrate. According with SEMs images, besides the lifting speed increase, the colloidal particle concentration in the suspension seems to have a crucial role in the studied cases of PS_{350}.

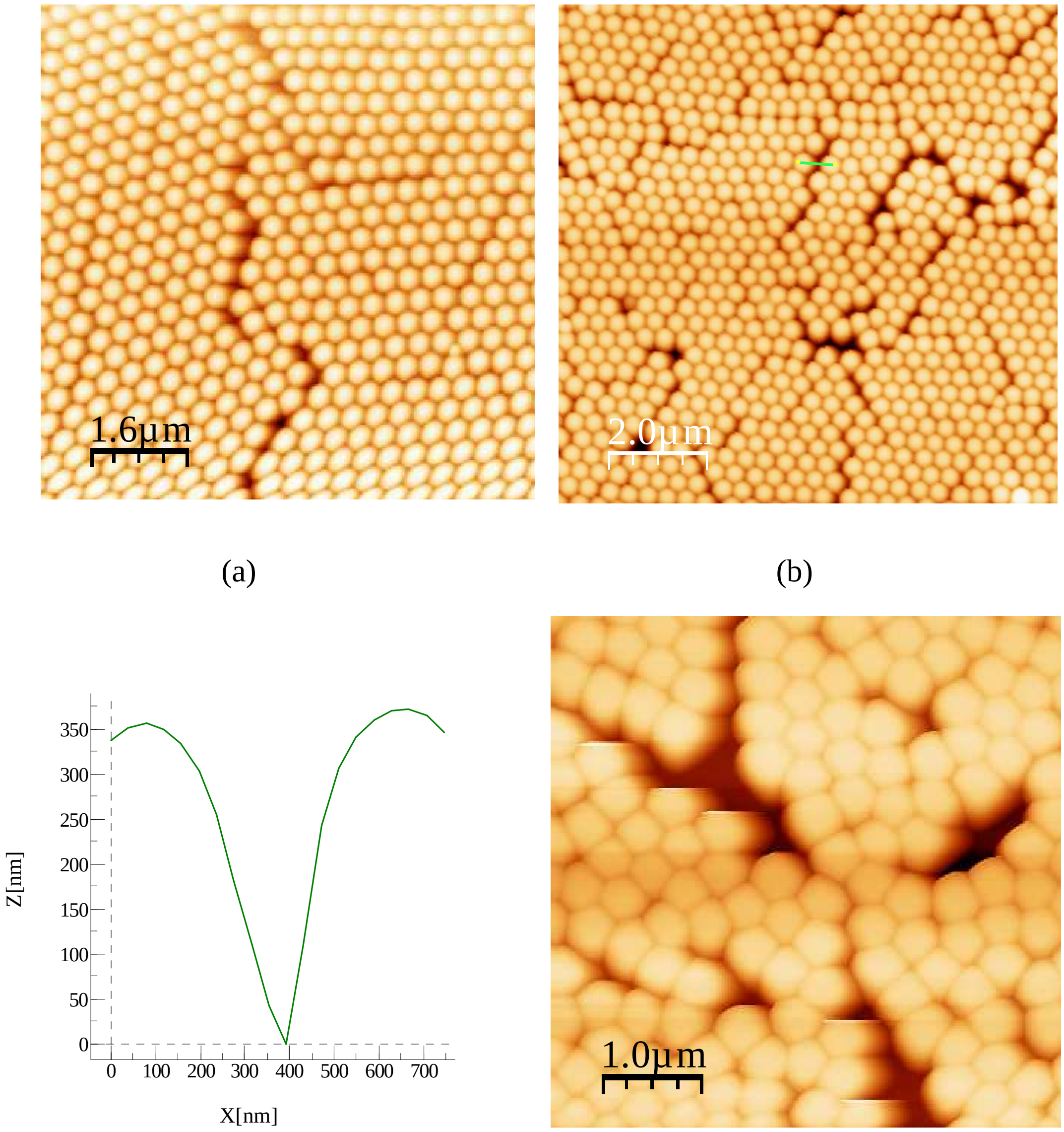

(a) (b)

(c) (d)

Figure 3.22: *Self-assembled polystyrene particles with diameter of ~350nm immersed 4 min in 1% w/v suspension in a volume ratio Ethanol:DI water 1:1 (a) Closely packed hexagonal assembly at withdrawal speed of 1mm/min.(b) Self-assembly at withdrawal speed of 2mm/min. The line marks the height profile shown in (c). The height profile measures the monolayer height in a line defect. (d) Self-assembly at withdrawal speed of 10mm/min*

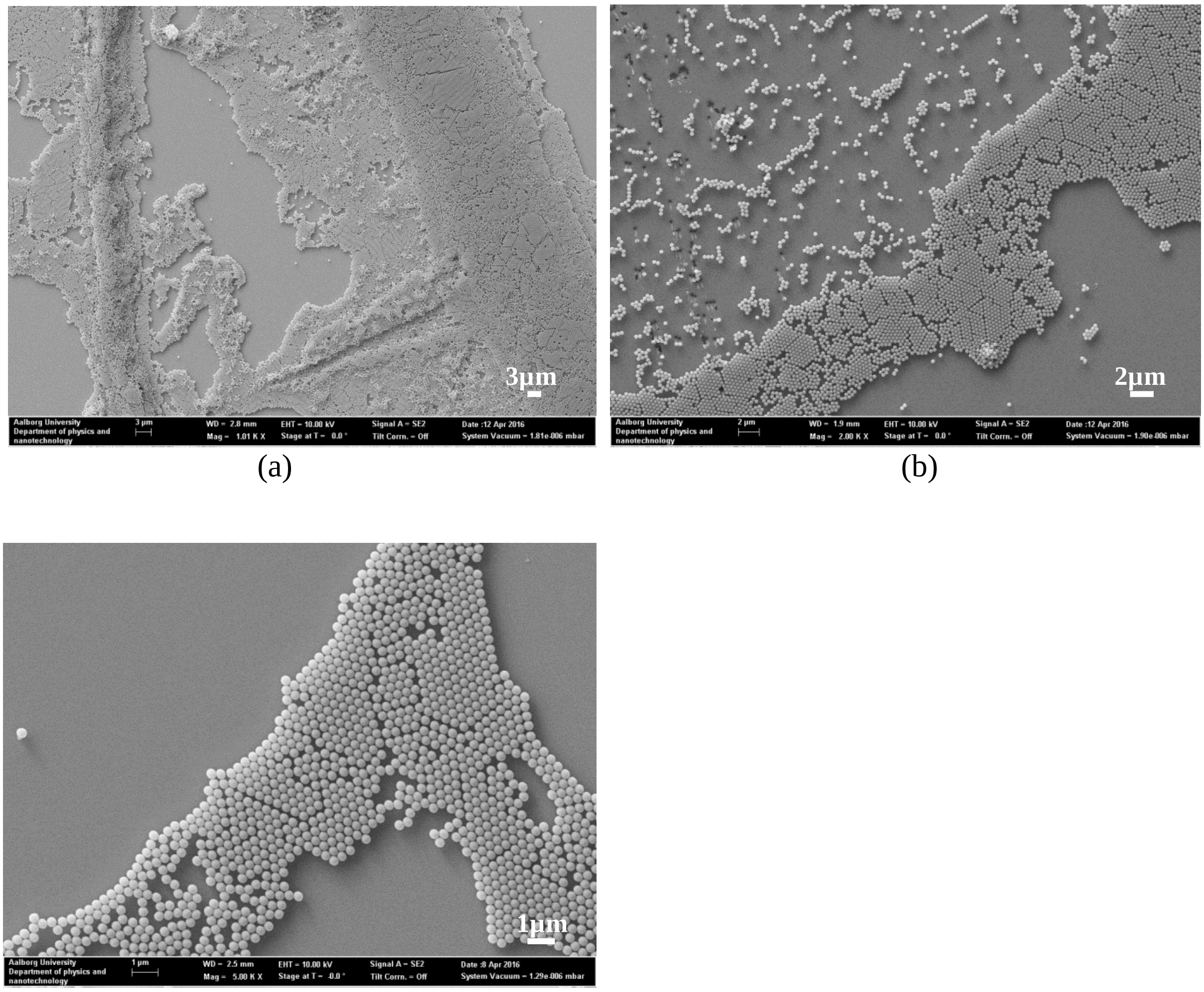

(a) (b)

(c)

Figure 3.23: *SEM images of polystyrene particles with diameter of ~350ηµm immersed 4 min in 1% w/v suspension in a volume ratio Ethanol:DI water 1:1 (a) Self- assembly at withdrawal speed of 1mm/min 1K magnification,(b) Self-assembly at withdrawal speed of 2mm/min 2K magnification, (c) Self-assembly at withdrawal speed of 10mm/min 5K magnification*

3.5 Monolayer Self-assembly by Langmuir-Blodgett

Two-dimensional colloidal crystals of polystyrene spheres are characterized with surface pressure-area (π-A) isotherms to define the most suitable surface pressure for transferring a film onto a silicon substrate in the Langmuir-Blodgett method. The π-A isotherm of polystyrene spheres monolayers at the water/air interface was assayed at different volumes and concentrations to find the most appropriate and typical isotherm which is in fact depicted in Figure 3.24. The surface pressure is plotted versus area per particle expressed in cm^2/mg.

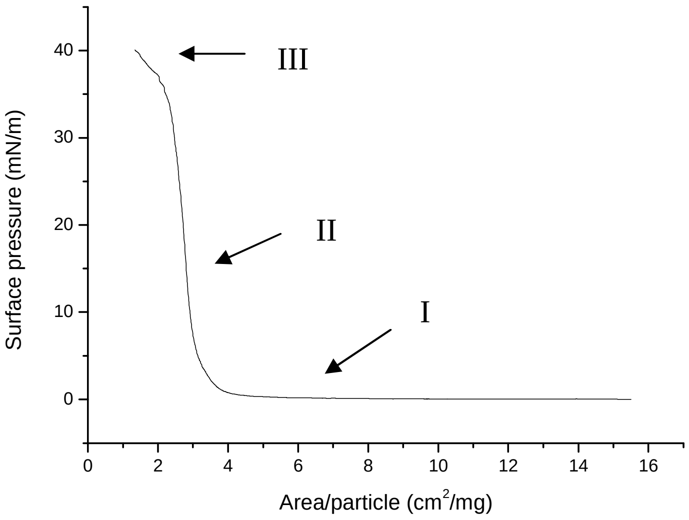

Figure 3.24: *π-A Isotherm of polystyrene particles with ~2μm diameter spread onto the surface in a volume of 68μl of a solution 7.5% w/v.*

The Figure 3.24 shows the typical π-A isotherm formed by three differentiate phases that remains invariable in shape for all compressions maintaining the surface pressure transitions and varying the area/particle. Region I belongs to the gaseous phase which is followed by a sharp transition to the solid phase. The steep surface pressure increase is very linear indicating that the liquid phase is apparently not present in the isotherm. The region III changes abruptly the line slope increasing the surface pressure more slowly. This behavior in the transition between region II and III is the collapse pressure of the thin film. The theoretical area/particle for a close hexagonally packed monolayer was around 7cm^2/mg what indicates that 57.1% of the particles were lost. According with the π-A isotherms, the surface pressure chosen for film transfer onto a silicon substrate was 20 mN/m in the hydrophilic case.

Hydrophilic substrate

The figure 3.25 shows the colloidal particle assembly onto a hydrophilic substrate at withdrawal speed of 1mm/min with PS_2 and initial volume spread over the interface of 68μl from a suspension of 7.5% w/v. The AFM images represent the same monolayer at different regions. In Figure 3.25(a), a not well-organized array of polystyrene microspheres can be recognized although some hcp ordering exists. It can be appreciated that the main disturbing element is the polydispersity. Smaller particles than average are incrusted in the monolayer disrupting the symmetry and the well-order. In Figure 3.25(b) some submonolayers are also found in the same sample in which the domains are small and the disorder extensive although the small islands of particles are well packed.

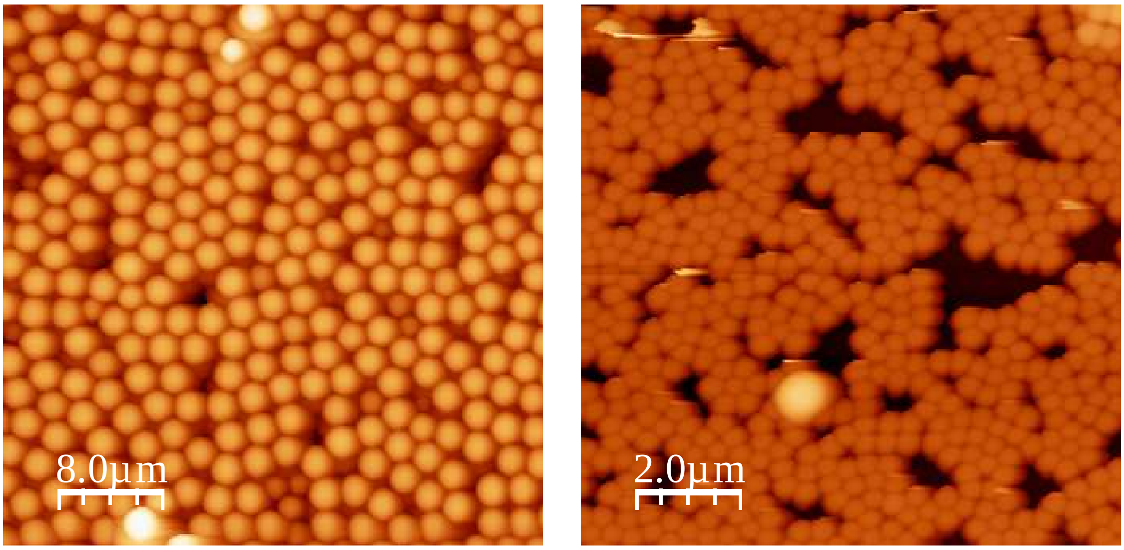

(a) (b)

Figure 3.25: *AFM images of self-assembled polystyrene particles with diameter of ~2µm initial volume of 68µl solution 7.5% w/v at withdrawal speed of 1mm/min and different scales.*

The latter AFM results are corroborated in Figure 3.26. SEM images show large extension coverage of polystyrene particles onto the substrate with hexagonally ordered domains and small empty areas between them. However, the whole monolayer reveals a lack of compressibility between particles to obtain a denser array with more tightly order.

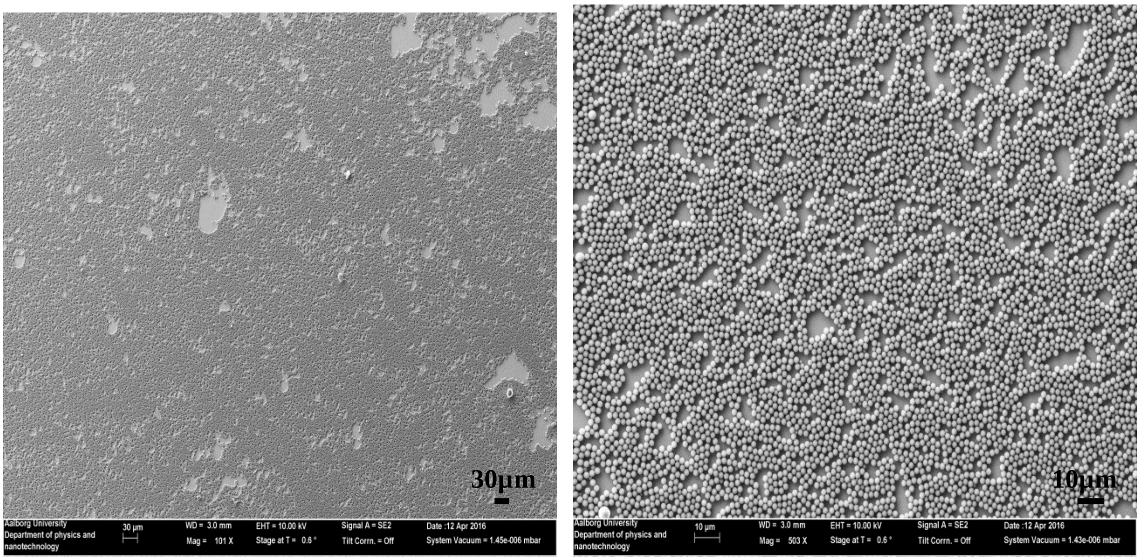

(a) (b)

Figure 3.26: *(a) Self-assembled polystyrene particles with diameter of ~2µm initial volume of 68µl solution 7.5% w/v at withdrawal speed of 1mm/min,0.1K magnification (b) Close-up of (a) 0.5K magnification.*

The Initial concentration and volume spread over the interface was varied to identify the most suitable conditions for improving monolayer packing and order. The best results in monolayer assembly of PS_2 particles were found with an initial volume spread over the interface of 102μl from a suspension of 5% w/v. The AFM image from Figure 3.27 shows a more closed-packed monolayer where the lattice defects are originated in part from the polydispersity. HCP ordering imperfections accumulate around the dissimilarity in particle sizes extending the local faults to larger defects across the monolayer, such as defect lines and vacancies as seen in the image below.

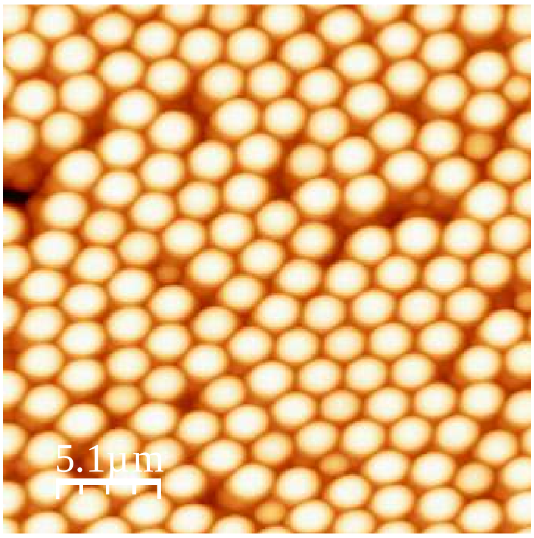

Figure 3.27: *a) Self-assembled polystyrene particles with diameter of ~2μm initial volume of 102μl solution 5% w/) at withdrawal speed of 1mm/min.*

The arrangement and packing are improved regarding the monolayer self-assembly shown in Figure 3.25 and 3.26 suggesting a dependence and influence in the material spread on the subphase. The monolayer is extended over a large area providing great particle coverage in Figure 3.28(a). Figure 3.28(b) shows in more detail the 2D structure in which hcp domains coexist with individual particles non closely-packed and small empty areas. The most probable reason for the absence of a complete hexagonally close-packed monolayer is the lack of further compression during film transfer.

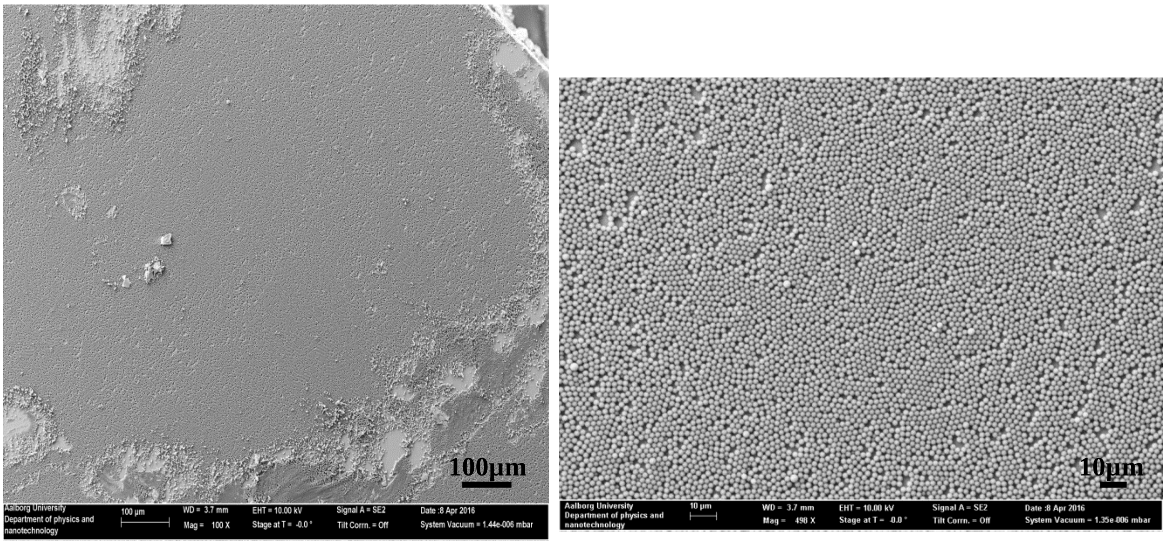

(a) (b)

Figure 3.28: *a) Self-assembled polystyrene particles with diameter of ~2µm initial volume of 102µl solution 5% w/v at withdrawal speed of 1mm/min,0.1K magnification (b) Close-up of (a) 0.5K magnification.*

In order to explore the dependence of self-assembly in the withdrawal speed, the monolayer were transferred at the same conditions than before with the only modification of lifting speed which was 5 mm/min instead of 1mm/min. SEM images in Figure 3.29 show a clear dependency on the withdrawal speed. The surface coverage drastically decreased, the film broke resulting in self-assembled islands rather than a large monolayer and the disorder spread. However, the islands attached to the substrate unexpectedly preserved the 2D well-packed structure with many small domains in hexagonal arrangement, although defects and holes were also present in the film.

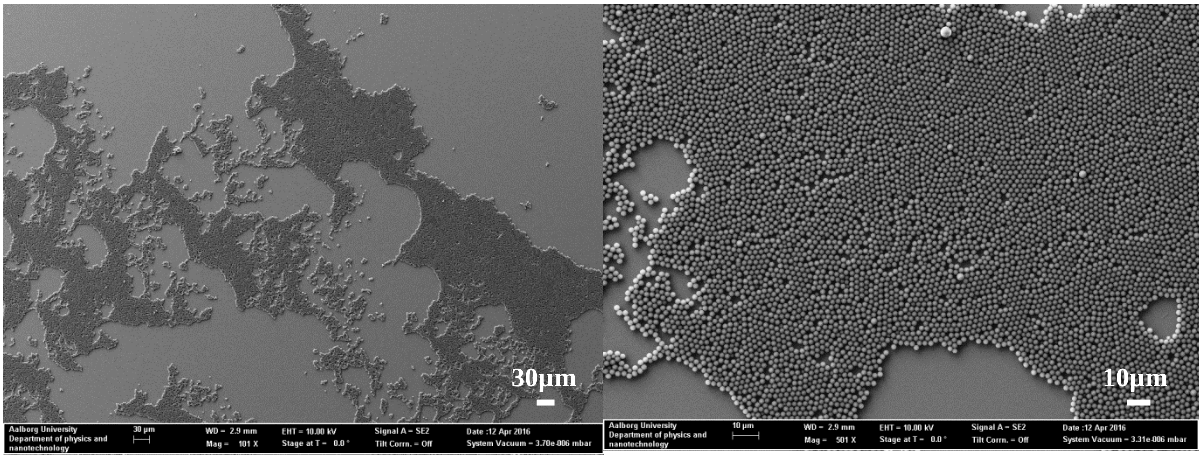

(a) (b)

Figure 3.29: *a) Self-assembled polystyrene particles with diameter of ~2µm initial volume of 102µl solution 5% w/v at withdrawal speed of 5 mm/min,0.1K magnification (b) Close-up of (a) 0.5K magnification.*

Two-dimensional colloidal crystals of polystyrene nanospheres with diameter of ~350nm are characterized with surface pressure-area (π-A) isotherms to define the most suitable surface pressure for transferring a film onto a silicon substrate in the Langmuir-Blodgett method. The π-A isotherm is depicted in Figure 3.30. Unlike the isotherm for PS_2 particles, the surface pressure-Area/particle shows three different slopes indicating three different phases before the collapse pressure takes place (not shown in the graph). The region I represents the gaseous phase followed by a phase transition due to slope increase towards the region II, the liquid phase. The final phase transition appeares around 25mN/m, where the slope sharply changes to give rise to the region III known as the solid phase. The theoretical area/particle for a close hexagonally packed monolayer was around $14cm^2/mg$ what indicates that 78.3% of the particles were lost. The probable increase in particle hydrophilicity favors the appearance of the liquid phase due to solvent interference as well as material lost hinders the transfer film onto the substrate. According with the π-A isotherms, the surface pressure chosen for film transfer onto a silicon substrate was 30 mN/m. Figure 3.31 shows the poor film transfer onto the substrate with a really small particle coverage and scattered distribution. No monolayer was formed and the order was reduced to islands of particles of different sizes with empty areas inside them.

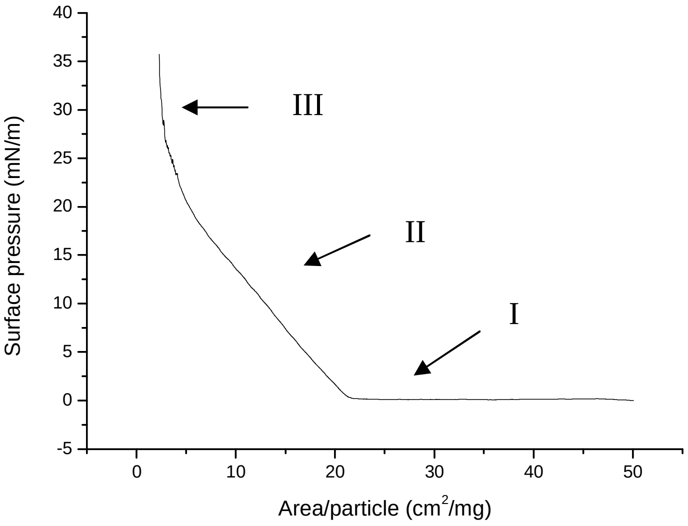

Figure 3.30*: π-A Isotherm of polystyrene particles with ~350nm diameter spread onto the surface in a volume of 77.4µl of a solution 2% (w/v).*

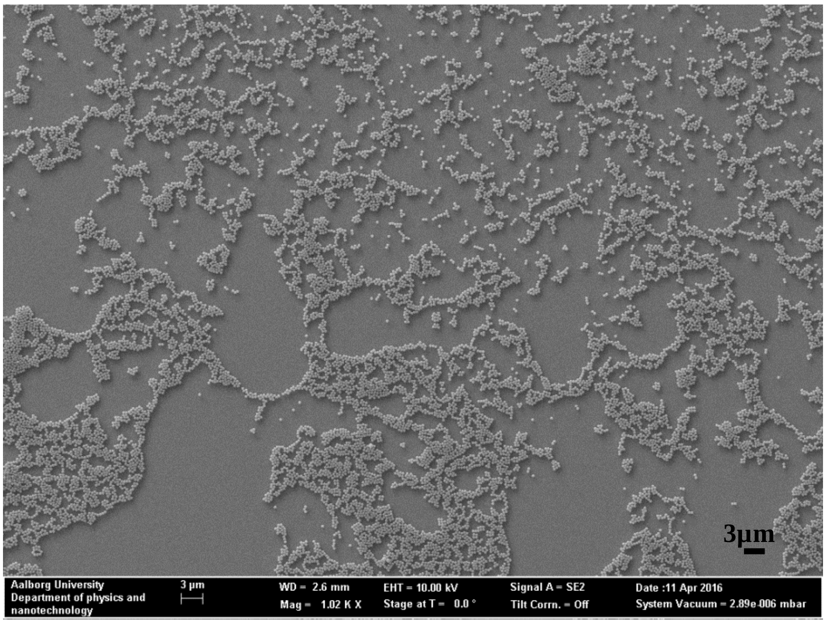

Figure 3.31: *Self-assembled polystyrene particles with diameter of ~350nm initial volume of 77.4µl solution 2% w/v at withdrawal speed of 1 mm/min,0.1K magnification*

APTMS-treated substrate

The behavior of monolayers of polystyrene particles was also studied with Langmuir-Blodgett technique in a substrate with a contact angle ~60º. The molecular organization was characterized in a less hydrophilic substrate in order to attempt to improve the previous results in the fabrication of high-quality colloidal crystals. Figure 3.32 shows the colloidal particle assembly of PS_2 particles onto an APTMS-treated substrate at lowering speed of 1mm/min with an initial volume of 206µl of polystyrene dispersed in ethanol in a series of increasing surface pressure. Figure 3.32(a) and (b) are a Langmuir-Blodgett deposition at 10mN/m, the monolayer structure has several cracks and lack of continuity. In the close-up image small hexagonally ordered domains can be appreciated delimited by voids, stripes and polydispersity which is also another distorting element that generates defects. Although the monolayer transfer has been carried out in the solid phase according with Figure 3.24, the phase at 10mN/m might be considered as liquid condensed considering the results obtained in Figure 3.32(c) and (d) at 15mN/m and Figure 3.32(e) and (f) at 25mN/m. The last two cases seem to have been carried out in the solid phase where the surface pressure provides enough particle cohesion to build a more homogeneous film. The monolayer is more compact and the cracks have disappeared although the close-up images reveal that different oriented small domains and defects such as voids or imperfections induced by polydispersity still remain to some extent.

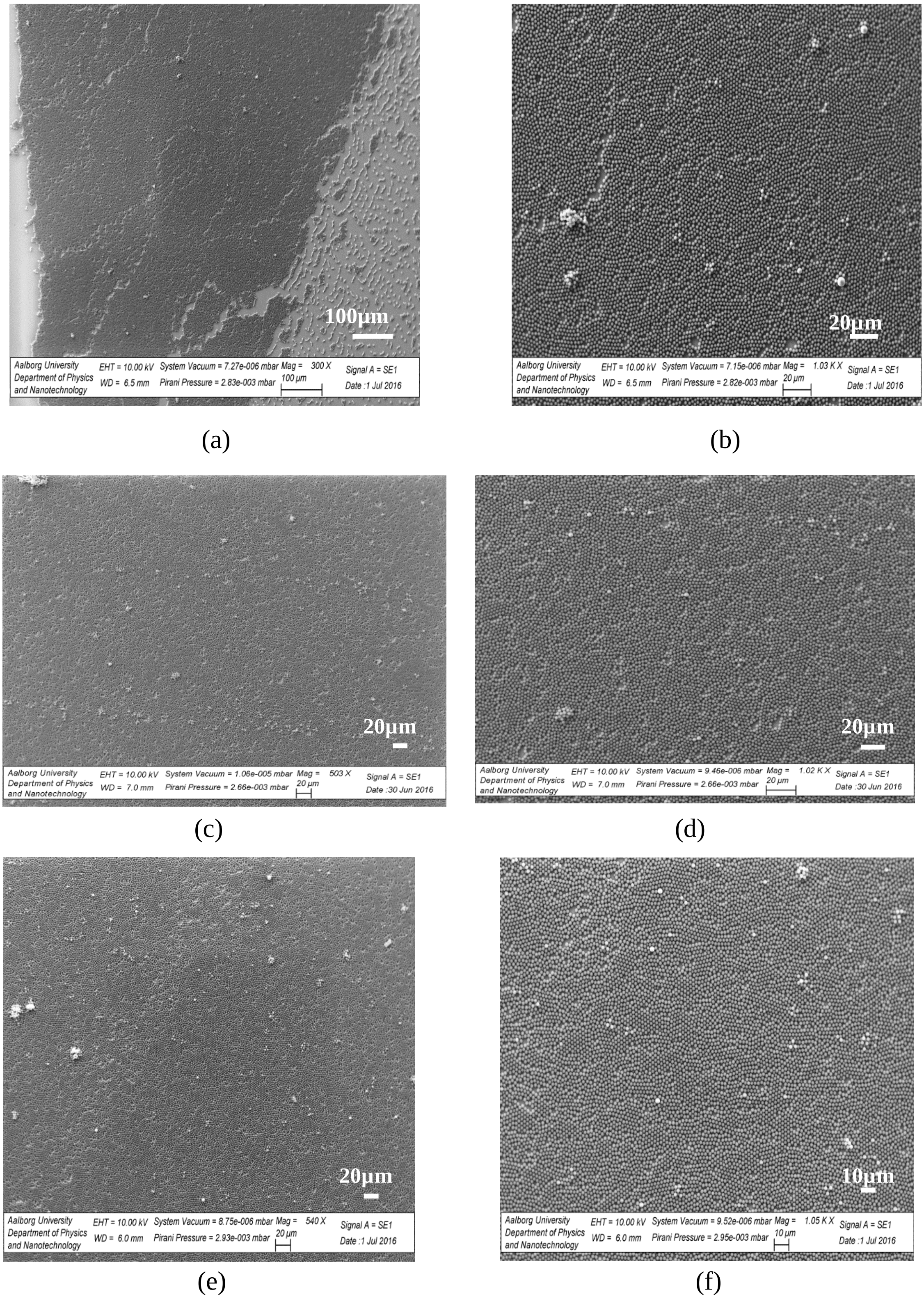

Figure 3.32: *Self-assembled polystyrene particles with diameter of ~2µm initial volume of 206µl solution 2.5% w/v at lowering speed of 1mm/min on a substrate surface modified with APTMS. (a) Surface pressure of 10mN/m 0.3K magnification, (b) close-up of (a) 1.03K magnification,(c) surface pressure of 15mN/m 0.5K magnification, (d) close-up of (c) 1.03K magnification,(e) surface pressure of 25mN/m 0.5K magnification,(f) close-up of (e) 1.05K magnification.*

The influence of the lowering speed of the substrate into the subphase was investigated at the same conditions than Figure 3.32(e), i.e, polystyrene particles with diameter of ~2μm initial volume of 206μl solution 2.5% w/v at lowering speed of 1mm/min and surface pressure of 25mN/m which provided a dense monolayer. Figure 3.33 clearly demonstrates the high dependency in the speed of transfer. Empty areas appeared between the monolayer and propagated accordingly. Figure 3.33(b) shows in more detail the inconveniences of faster lowering speeds than 1mm/min. On the top-right corner a crack has markedly split the film, and the worst packed section around the empty areas situated along the vertical direction on the left side of the image seem to be the initiation mechanism of the monolayer rupture.

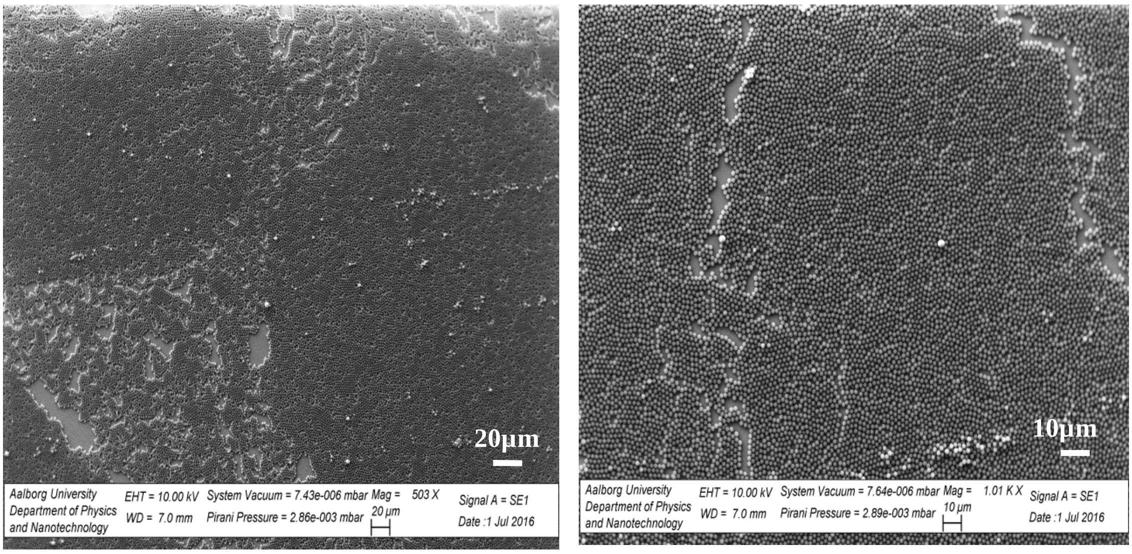

(a) (b)

Figure 3.33: *(a) Self-assembled polystyrene particles with diameter of ~2μm initial volume of 206μl solution 2.5% w/v at withdrawal lowering of 3mm/min on a substrate surface modified with APTMS and surface pressure of 25mN/m. 0.5K magnification (b) Close-up of (a) 1.01K magnification.*

PFS-treated substrate

The increase of the contact angle until ~100° to carry out a Langmuir-Blodgett film deposition on a hydrophobic substrate had a negative effect in the self-assembly of the polystyrene particles. A small change in the surface pressure of 5mN/m fluctuates between a dense particle multilayer and a drastic surface coverage decrease. Figure 3.34(a) shows multilayer patterned structures with protuberant stripes that stand above the average particle arrangement. At higher magnification and at a surface pressure of 20mN/m it can be confirmed that the main configuration is at least a bilayer of particles as depicted in the Figure 3.34(b). This multilayer accumulation is the main pattern obtained when other PFS-treated substrates were assayed. In order to try to decrease the number of particles on the substrate with the consequent layer reduction, the lowering speed into the subphase is increase as shown in Figure 3.34(c). However, only big agglomerates of particles were formed.

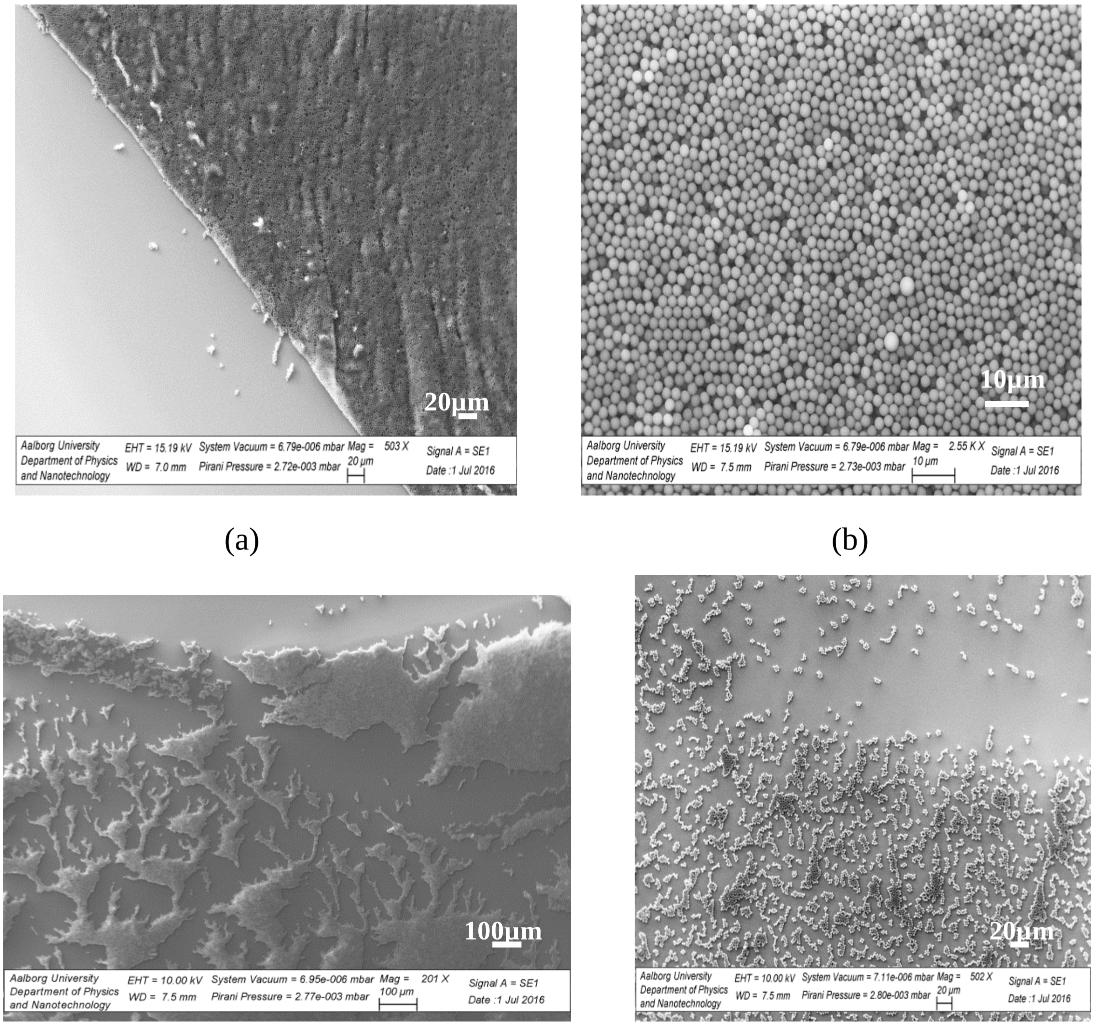

(a) (b)

(c) (d)

Figure 3.34: *Self-assembled polystyrene particles with diameter of ~2μm initial volume of 206μl solution 2.5% w/v on a substrate surface modified with PFS. (a) surface pressure of 20 mN/m, lowering speed of 1mm/min 0.5K magnification (b) Close-up of (a) 2.55K magnification, (c) surface pressure of 25mN/m, lowering speed of 3mm/min 0.2K magnification, (d) surface pressure of 15 mN/m, lowering speed of 1mm/min 2.55K magnification.*

Horizontal drawing-up method

Langmuir-Blodgett technique used to form closely-packed particles in a hexagonal arrangement was not successful in neither hydrophilic nor hydrophobic substrates. In order to investigate the influence in the monolayer order during the critical step of transferring the film onto the substrate, the compressed monolayer on the subphase before the substrate withdrawal or immersion was horizontally transfer to a hydrophilic or hydrophobic substrate. Figure 3.35(a) depicts the monolayer transfer onto an APTMS-treated substrate. The grain size or hexagonal domains grew in comparison with the highly-ordered domains in Langmuir-Blodgett although the particle density is similar, larger voids which were probably enlarged during the substrate drawing-up were promoted. Figure 3.35(b) shows the horizontal lifting (the transfer is made from the top of the monolayer) onto a APTMS-treated surface. The monolayer is disordered because of the low affinity between non-ideal hydrophobic-hydrophilic polystyrene balance for this substrate. Figure 3.35 (c) and the close-up (d) are a monolayer horizontally transferred onto a hydrophilic substrate. The monolayer shows an increment in the number of grains with hexagonal order in comparison with Langmuir-Blodgett technique as well as in Figure 3.35(a) with APTMS-treated substrate. Figures 3.35(e) and (f) show a loss in the regular order since probably PFS-treated has less affinity for the polystyrene particles because of the hydrophilic-hydrophobic character of PS_2.

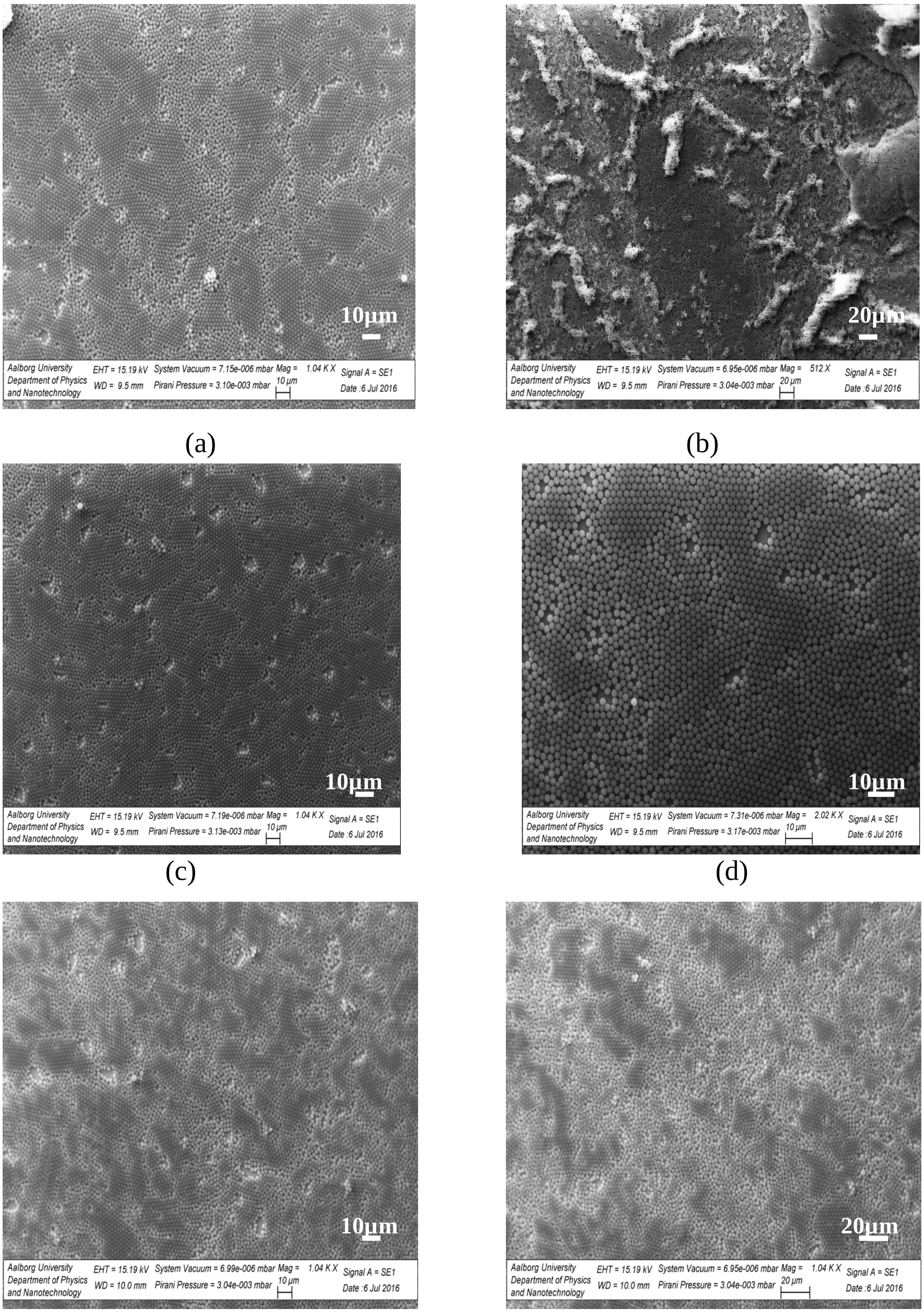

(a) (b)

(c) (d)

(e) (f)

Figure 3.35: *Monolayer morphology of self-assembled polystyrene particles with a diameter of ~2μm initial volume of 206μl solution 2% w/v at surface pressure of 25mN/m (a) on a substrate surface modified with APTMS 1.04K magnification, (b) on a substrate surface modified with APTMS in horizontal lifting method 0.5K magnification, (c) on a hydrophilic substrate 1.04K magnification, (d) close-up of image shown in (c) 2.02K magnification, (e) and (f) on a substrate surface modified with PFS 1.04K magnification*

3.6 Structural characterization and ordering analysis

The structural analysis of 2D colloidal crystals provided a good insight of the quality of the self-assembled film. The long ordered domains as well as the monolayer faults were able to be characterized with analytic methods to investigate the influence of the variations in the interparticle forces, surface properties and evaporation rate. The triangulation analysis provides large areas of hexagonal order since triangles that are considered ordered are colored green, triangles with side deviation below 10% but angular deviation from 60º above 10% are colored yellow, triangles with angular deviation from 60º below 10% but side deviation above 10% are colored blue and triangles colored white are considered disordered. Figure 3.36 shows a really well-ordered area via droplet evaporation supported by the high density of green triangles and the main absence of disordered white triangles. Furthermore the high number of occurrences around the value of 60º in the angle distribution in Figure 3.36(c), and also the most common value of side length around to one particle diameter in Figure 3.36(d) demonstrate the high periodicity of the monolayer assayed. Figure 3.36 (e) illustrates the number of different grains in different colors prevailing the large grains with high hexagonal order. This is confirmed in Figure 3.39(f) by the high number of triangles that build each grain in the analytical analysis and by the tendency of the column bars to stick together close to the y-axis; a sign of well packing and organization.

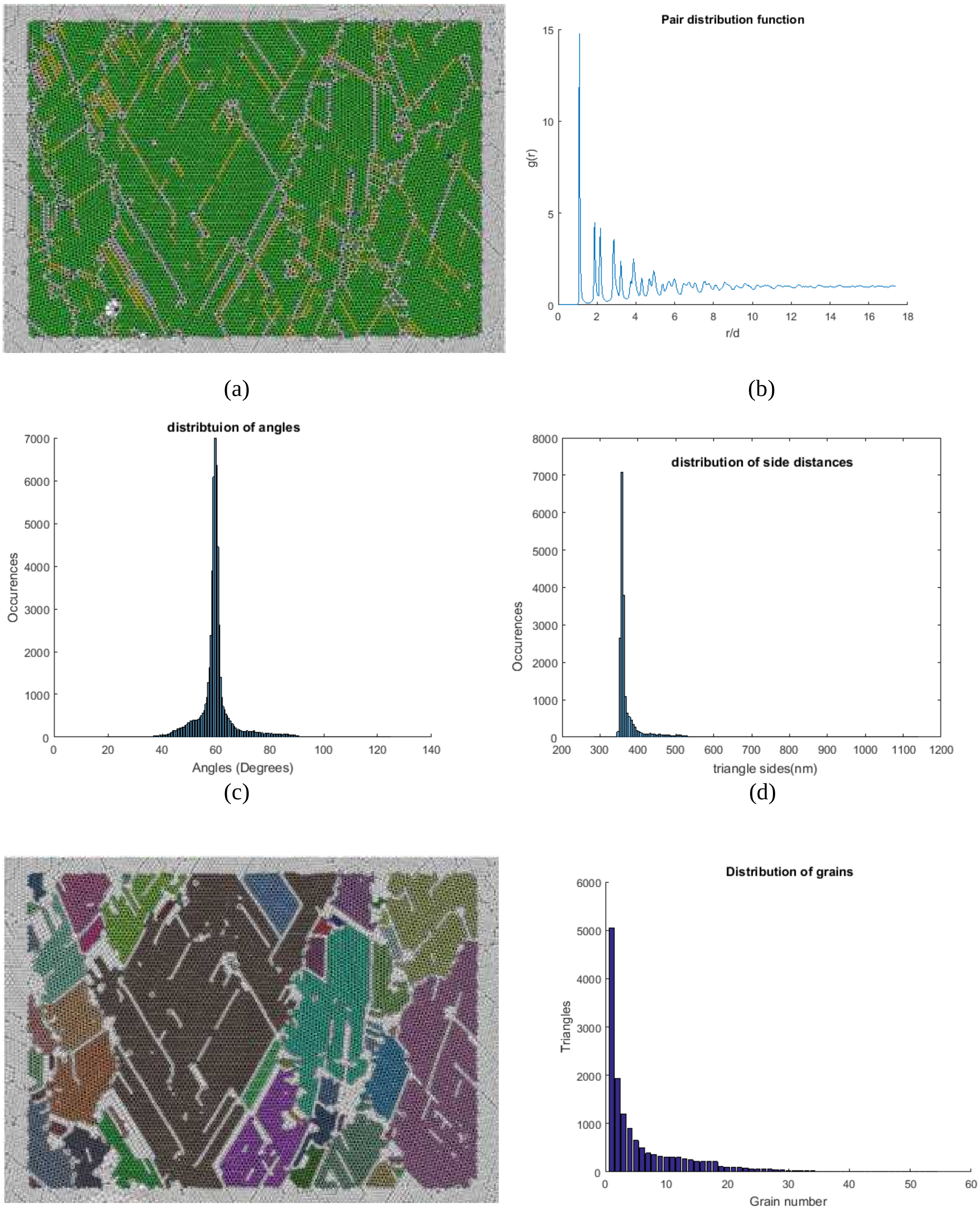

(a) (b)

(c) (d)

(e) (f)

Figure 3.36: *Structural characterization of a self-assembled monolayer via droplet evaporation with particle diameter of ~350 nm 10%w/v DI water and initial volume of 0.5µl on a hydrophilic substrate.2.5K magnification (a) Triangulation, (b)Pair distribution function (c) Distribution of angles, (d) Distribution of side distances,(e) Grain analysis, (f) Distribution of grains*

Figure 3.37 shows a monolayer assembly by the dip-coating method. The deposition substrate was hydrophilic since attempts to use dip-coating for monolayer assembly in substrates with contact angle around 60º or 100º were always unsatisfactory. In Figure 3.37 (a) more boundaries without clear patter appear between ordered areas with a

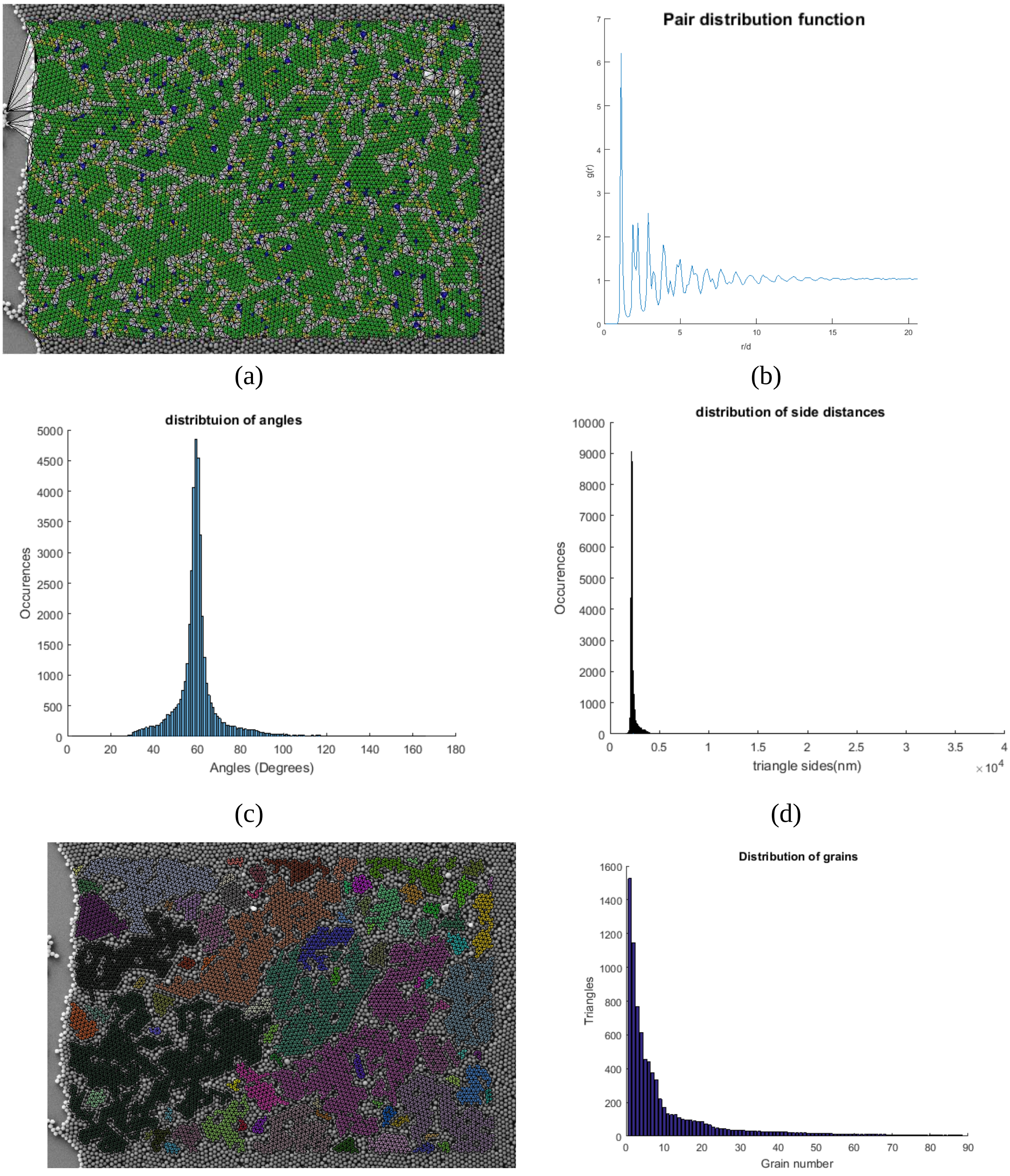

(a) (b)

(c) (d)

(e) (f)

Figure 3.37: *Structural characterization of a self-assembled monolayer via dip-coating with particle diameter of ~350 nm immersed 4min 3%w/v suspension in a volume ratio Ethanol:DI water 1:1 withdrawal speed of 2mm/min 0.5K magnification on a hydrophilic substrate.(a) Triangulation, (b)Pair distribution function (c) Distribution of angles, (d) Distribution of side distances (e)Grain analysis (f) Distribution of grains.*

clear increment in the number of blue triangles. This indicates that the three-angle deviation is kept below the 10% while the triangle sides are getting distorted. Therefore, the scattered blue triangles could imply that the monolayer was unpacking isotropically, although the image still shows a good order parameter. The more disordered monolayer regarding the average angular deviation can be seen in the distribution of angles in Figure 3.37(c) whereas the distribution of sides remains close to the particle diameter. The pair distribution function in Figure 3.37(b) still displays long- range order, however the size of the grains in the monolayer has decreased with the appearance of more number of grains with less triangles as shown in Figure 3.37(f).

Figure 3.38 is a self-assembled monolayer via Langmuir-Blodgett deposition. The triangulation order showed in Figure 3.38(a) presents a less ordered monolayer with an important decrease of highly-packed regions, the smaller domain size and the change in the film structure is reflected in the pair distribution function by showing less range of order and faster decay than the previous cases. The distribution of angles and sides in Figure 3.38(c) and (d) has spread to a larger interval of values resulting in a loss of convergence with general short-range of order. Likewise, the number of grains has raised but the size of the grains has been much reduced and scattered through the monolayer as is depicted in Figure 3.38(e) and (f).

Horizontal transfer drawing up a monolayer from the water /air interface in a solid phase provides better results than the conventional vertical deposition. The order was increased as seen in the denser and more compact green areas in Figure 3.39(a) although the film has many defects and disordered boundaries. The pair distribution function shows larger range of order than in the case of Langmuir but the damping in the function reveals the existence of small domains and worst hexagonal lattice than in Figures 3.37 or 3.36. The number of similar side lengths increases according with the distribution of sides in Figure 3.39 (d) implying that a greater number of equilateral triangles are found in the monolayer. The angular deviation from 60º decreases as shown in Figure 3.39(c) and the size of the grains increases as the number of them decreases. Evidentially, all the characterization parameters improved but the monolayer cannot be considered as a long-range ordered structure.

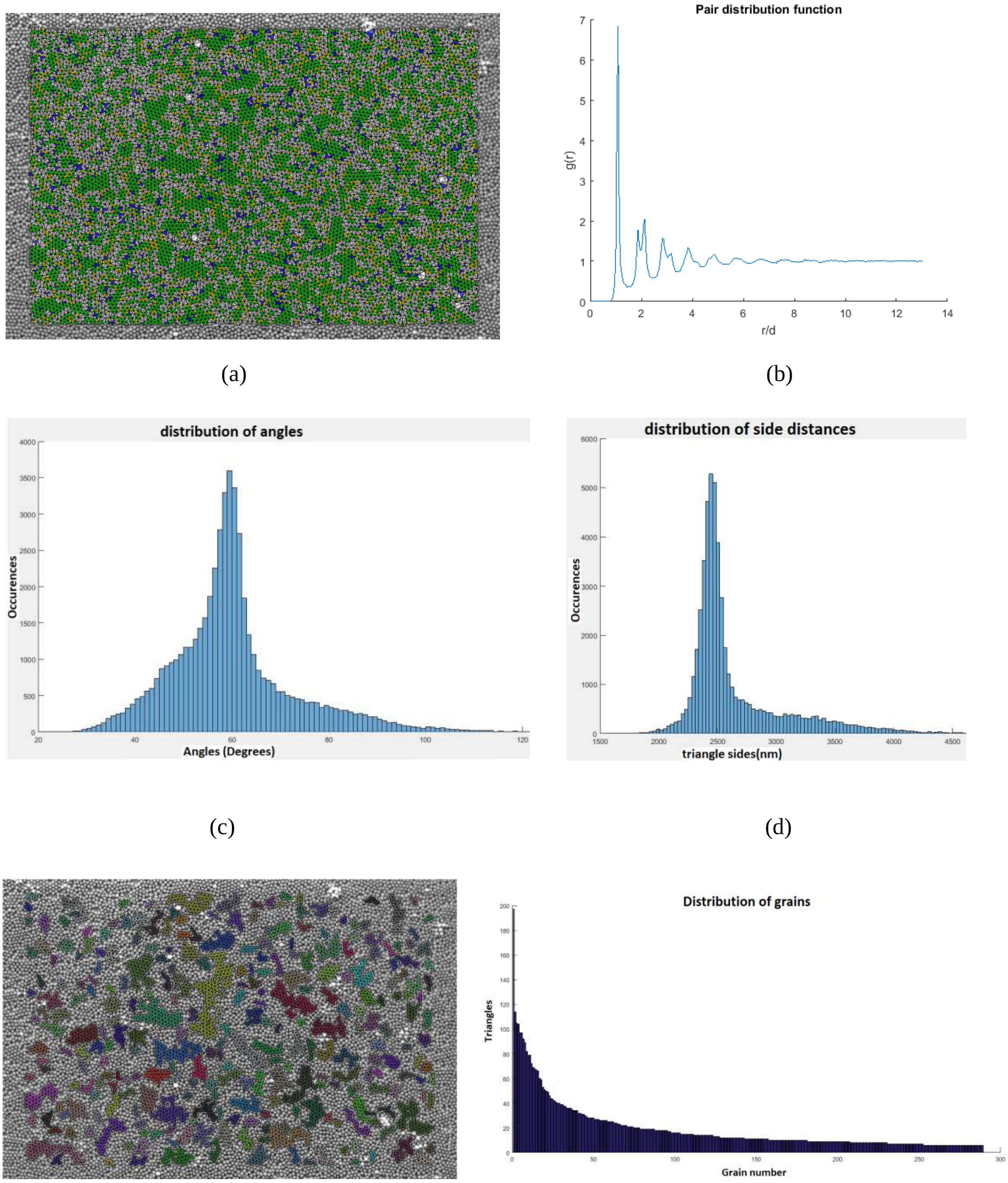

(a) (b)

(c) (d)

(e) (f)

Figure 3.38: *Structural characterization of a self-assembled monolayer via Langmuir-Blodgett with particle diameter of ~2μm initial volume of 206μl EtOH solution 2.5% w/v withdrawal speed 1mm/min at 20mN/m on a substrate surface modified with APTMS 1.05K magnification a) Triangulation, (b) Pair distribution function (c) Distribution of angles, (d) Distribution of side distances (e) Grain analysis (f) Distribution of grains.*

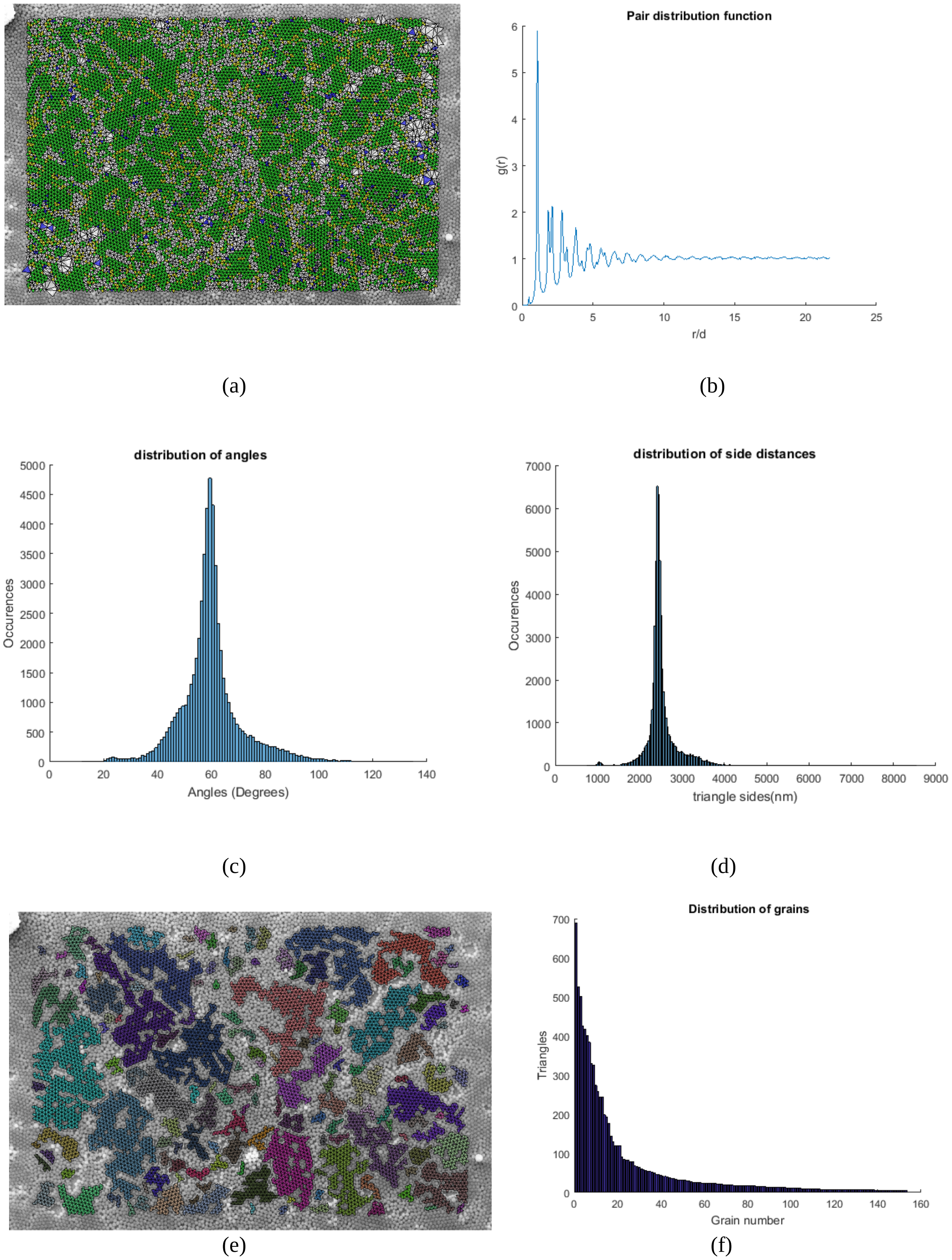

(a) (b)

(c) (d)

(e) (f)

Figure 3.39: *Monolayer self-assembled polystyrene particles via Horizontal method with a diameter of ~2µm initial volume of 206µl solution 2% w/v at surface pressure of 25mN/m on a substrate surface modified with APTMS 1.04K magnification. a) Triangulation, (b) Pair distribution function (c) Distribution of angles, (d) Distribution of side distances (e) Grain analysis (f) Distribution of grains.*

The following table summarizes the ordering analysis considered for different types of substrates, concentrations and monolayer self-assembly techniques. All the characterization parameters are compared to quantify the best results in the fabrication of 2D crystal films.

Droplet evaporation

Region	substrate	Φ (μm)	Ang. dev.(%)	side dev.(%)	Order (%)	Ordered Area (μm^2)	grain area (μm^2)	Largest grain (μm^2)
1	APTMS	2.3	22.3	27.6	0.81	537.4	-	-
2	Hydrophilic	0.35	6.6	5.5	74.8	2077.1	2042.6	699.5
3	Hydrophilic	0.35	5.1	4.4	87.4	1806.2	1800.4	1663.6
4	Hydrophilic	0.35			90.1		1756.2	1736

Dip-coating

Region	substrate	Φ (μm)	Ang. dev.(%)	side dev.(%)	Order (%)	Ordered Area (μm^2)	grain area (μm^2)	Largest grain (μm^2)
1	Hydrophilic	2.3	17.1	14.4	18.8	5814.6	2030.3	110
2	Hydrophilic	2.3	10.2	10.1	60.7	18888.5	18033.1	3282.8

Langmuir-Blodgett

Region	substrate	Φ (μm)	Ang. dev.(%)	side dev.(%)	Order (%)	Ordered Area (μm^2)	grain area (μm^2)	Largest grain (μm^2)
1	APTMS	2.3	14.9	11.5	39.1	18865.5	14280.4	501.1
2	APTMS	2.3	15.9	13.1	32.2	16033.8	10961.5	173.6
3	APTMS	2.3	16.2	13.6	28.4	15432.1	9250.4	168.7
4	APTMS	2.3	17.1	15.1	20.9	11379	4522.4	93.8
5	APTMS	2.3	16.7	15.1	21.3	11569.1	4496.1	84.1
6	APTMS	2.3	16.4	14.4	25.9	12484.5	6533.1	82.4
7	APTMS	2.3	16.2	13.5	29.4	14177.5	8685.4	149.6
8	APTMS	2.3	16.8	14.2	23.1	11761.3	4810.5	84.6
9	APTMS	2.3	16.2	13.2	30.2	15150	8922.8	168.3
10	APTMS	2.3	17.1	17.7	11.5	10275.2	774.1	29.2
11	Hydrophilic	2.3	15.5	12.4	32.8	10113.5	6633.7	306.5
12	Hydrophilic	2.3	14.9	15.2	26.1	7907.9	4541.4	143.2
13	Hydrophilic	2.3	20.8	19.9	1.4	454.2	-	-

Horizontal transfer

Region	substrate	Φ (μm)	Ang. dev.(%)	side dev.(%)	Order (%)	Ordered Area (μm^2)	grain area (μm^2)	Largest grain (μm^2)
1	APTMS	2.3	15	14.6	36.3	18490	14828	655.9
2	APTMS	2.3	12.7	9.7	51.9	26565.5	23907.5	1793.2
3	APTMS	2.3	13.2	11.7	47.6	24301.4	21632.2	1827.7
4	Hydrophilic	2.3	17	16.7	24.7	12692.6	6865	117.1
5	Hydrophilic	2.3	11.8	10.9	55.4	28415.6	26697	7188.1
6	PFS	2.3	21.1	23.1	5.8	2696.7	59.7	24.5
7	PFS	2.3	24.1	29.4	0.89	459.7	-	-
8	PFS	2.3	20.2	21.4	12.7	6503.8	1261.8	47.5
9	PFS	2.3	27.8	37.1	0.16	76.7	-	-

Table 3.1: *Results of the ordering analysis from SEM images*

Table 3.1 provides information about the quality of the 2D colloidal crystals generated through different methods and parameters. Droplet evaporation method displays better results with hydrophilic substrates and lower colloidal concentration. Although the well-ordered grain area is similar in all the regions, less concentrated droplets achieved fewer grains but larger hexagonal areas. The sample analyzed in Region 4 provides one of the largest grains regarding all the methods analyzed. In regard to Dip-coating, a surprising large ordered area was found in a Region 2 which turns to be the second largest grain. However, this result was an exception since the method reproducibility and experimental conditions were difficult to perform. Langmuir-Blodgett technique was extensively studied and APTMS-treated substrates providing better percentage of order and larger ordered areas than hydrophilic substrates probably influenced by the polystyrene particles properties. The best results were obtained at a surface pressure of 25 mN/m and 1mm/min withdrawal speed. Faster withdrawal speed or lower surface pressure provides worst results in the ordered area. A great disparity exists between the total grain area and the largest grain in both types of substrate. The large amount of grains regarding the large size of the grain area could be related to the difficulty of producing highly-packed monolayers in Langmuir-Blodgett method. In the Horizontal transfer both APTMS and Hydrophilic substrates show the best results in this method whereas PFS displays really poor results. Region 2 and Region 5 overcome the 50 % of order and the hydrophilic substrate provides the largest ordered area as well as the largest grain. The distortion between grain area and the largest grain is here reduced in relation with Langmuir-Blodgett suggesting that larger size grains are found as well as larger ordered areas.

The angular deviation is always greater than the side deviation independently of method employed for the colloidal film fabrication. This responds to the triangles properties in relation to the sides and angles. A deviation in one of the angles of the triangle necessarily implies the deviation of another angle. Nevertheless, a variation of the length of one triangle side does not necessary imply the deviation of another one as happens in the isosceles triangles.

4 Discussion

4.1 Monolayer Self-assembly by droplet evaporation.

4.1.1 Silica particles

Silica particles deposited by droplet evaporation on substrates without UV/ozone treatment resulted in the formation of ring-like structures after droplet drying in all cases. The contact angle of approximately 60º pinned the contact line and the particles were dragged together with solvent molecules towards the periphery to maintain the contact line fixed. The ring thickness and particle accumulation in the aggregated state depends on the wetting properties. The particle velocity towards the edge is subjected to equation 1.27 and specially dominated by the parameter λ. This parameter decreases as contact angle increases and the ring growth rate is enhanced accordingly. The faster the particle flow is the more disordered arrangement obtained since the particles stack due to the insufficient time for ordering. The geometry left by the evaporating droplet also depends on the type of solvent. Ethanol was used together with water to decrease the droplet surface tension in a try to avoid ring shape and therefore an effective change in the droplet spherical shape was induced by the modification of water surface tension and the faster evaporation rate of ethanol. However, the particles still accumulate in the edge of the drying lines. Colloidal particles were also studied in a solvent with low ionic strength at pH 9 to assure deprotonation of hydroxyl groups and enhance the electrostatic repulsion. The low ionic concentration does not reduce the Debye length and vdW forces remain at the same range. However, the adhesion forces were still predominant and not order but aggregation was the main particle configuration after droplet drying. According with all the previous results, the wetting properties, i.e. the contact angle, have been demonstrated to have a large influence in the final particle arrangement and in the coffee ring formation.

After UV/ozone treatment, the silicon substrates showed a contact angle of a few degrees with a subsequent increase in hydrophilic properties and an improved wettability. The silica particles were not so densely accumulated in the ring structure with a better distribution inside the droplet area upon solvent evaporation. The nanospheres were found besides the ring formation in some self-assembled monolayer islands, a clear indication of the process improvement, but the ordered arrangement was still really low. The particles tend to aggregate even without showing any domain of order when they are closely packed. This fact is appreciated in Figure 3.9(c) where a certain degree of particle polydispersity can be appreciated and to be suggested as one of the main obstacles for well-ordered monolayers.

Additionally, the increase in hydrophilicity is related to the cleaning process in which the contamination is removed and the number of hydrophilic groups increased. Furthermore, taking into account that the surface of silica particles is plentiful with silanol groups the attraction between the particles and the substrate is expected to rise. Due to the stronger particle-substrate attraction, the particle mobility over the substrate during film drying is hindered leading to a loss of order in the monolayer or to aggregation processes.

The lack of order in self-organized monolayers with silica nanospheres was also supported by F. Burmeister et al., [65] who obtained similar results with particles below 120nm in diameter. They only found stripes of particles organized in a similar number of mono-and multilayers. The difficulty of assembly small nanospheres could be related to the film rupture during the drying process. The small particle diameter only enables the particles to protrude above the water film at the last state of evaporation not providing enough time for capillarity to induce order before the evaporation process is completed.

4.1.2 Polystyrene particles

The monolayer self-assembly by evaporation droplet with polystyrene particles led to the best results among all the methods investigated. It was possible to obtain highly-ordered latex monolayers from particles with different sizes although particles with diameter of ~2µm were more difficult to assembly in large areas. In this case, ring disposition and bilayers were formed together with areas of monolayer arrangement. The monolayer regions were probably formed at the last area of droplet evaporation as shown in Figure 3.12(a) and also between concentric rings (Figure 3.12(c)) indicating that the droplet recedes as the evaporation proceeds. The monolayer area is influenced by the small droplet volume deposited on the hydrophilic substrate in order to prevent the colloidal droplet to be spilt out over the edges of the substrate. Therefore, the fast evaporation rate induced by the small volume causes a large convective effect which becomes the dominating force exceeding in magnitude the lateral capillary force. The particles were then carried together to regions where they aggregate in ring-like shapes or multilayer formations since the lateral capillary force did not have enough time to arrange order. This effect is even more pronounced when the colloidal particles are polydispersed in the deposition droplet since the mechanism by which particles are segregated depending on the size is carried out by the lateral capillary force. At low evaporation rates, particles with bigger size protrude first the water film and consequently self-assembly in ordered domains than can be further used as nuclei for smaller particles crystallization during the thinning of water film. S Rakers et al., [66] used a chamber where the substrate was placed on a Peltier cell to control the temperature and ambient humidity of the whole system. They found that the order is dependent on the evaporation process homogeneity and particularly decisive for polydispersed systems; low temperature and hence low evaporation rate enhanced the particle arrangement. On the contrary, monodispersed particles did not show a strong temperature influence which aggress with the better hexagonal packing in both SEM and AFM images for polystyrene particles of ~350nm.

The improved order in Figure 3.13 and Figure 3.14 showed large domains with hexagonal arrangement although vacancies, dislocations and disordered domains can still be found. Some of those defects in the monolayer arose from the presence of dissimilar size particles, suggesting that part of the imperfections could be avoided by using monodispersed colloidal particles. Furthermore, although the temperature does not have the same influence in monolayer ordering as with larger polystyrene particles, fast evaporation in small droplet volume produces deformation and share stress causing larger extent of line defects (dislocations).

The self-assembled monolayer properties and the extension of order are similar to the results presented by Z. Lu et al., [67] suggesting that the hexagonal arrangement provided by this method improves the monolayer stability through the balanced interparticle interaction between attractive van der Waals forces and repulsive electrostatic forces which mainly stabilizes the monolayer after the inducement of order by the capillary forces.

Nucleation and growth of monolayers through particles deposited in the liquid-air interface of a droplet did not produce any long-range ordering onto APTMS-treated or PFS-treated substrates. The interfacial mechanism requires a fast evaporation to enhance particle dispersion in the liquid-air interface as well as attractive interaction between particles. However the ring-like structure left by the more hydrophilic APTMS-treated substrate and the quasi-concentric rings patterns left on the more hydrophobic PFS-treated one suggest that the particles are not sufficiently hydrophobic to remain in the interface and they sink into the droplet. The deposition mechanism eventually changes and becomes a colloidal droplet driven by the three-phase contact line and liquid convection caused by the non uniform evaporation. The mass distribution in the different structural patterns shows the variation in the deposition kinetics on the hydrophobic substrate. This characteristic pattern evidences a pinning and depinning process where particle accumulation proceeds until the receding contact angle is reached due to droplet volume decrease. Furthermore the larger particle accumulation in the center of the pattern is also produced during drying process of colloidal droplets since the hotter place situated close to the contact line and the colder place on top of the drop generates a flow that tends to carry particles to the drop center. In this way the convective mechanism of radial flow and Marangoni recirculation overcomes the uniform depositions of the DLVO mechanism.

4.2 Monolayer Self-assembly by dip-coating

The coating process of silicon substrates with a self-assembled monolayer gave rise to diverse rate of successful deposition in which the hexagonal close-packed structure was found at different percentage of coverage over the substrate surface. All the samples presented to a greater or lesser extent multilayers and particle accumulation at the bottom of the substrate and loosely-packed islands of monolayer at the top of the substrate. The dip-coating technique is dependent of the concentration and the lifting speed, in Figure 3.18 and 3.19 well-packed hexagonal structures almost show similar properties at lifting speeds of 1mm/min and 2mm/min respectively. Comparable results were obtained with polystyrene of ~350nm diameter with the difference of more pronounced increment of line defects at 2mm/min. However at withdrawal speed of 10mm/min voids and line defects are notably increased in each case together with less organized monolayer and lower substrate coverage rate. This is attributed to the mismatch between withdrawal speed and evaporation rate where the flux of particles towards the substrate generated by the evaporation rate is not enough to preserve the monolayer continuity resulting in scattered stripes and loosely packed regions.

When the polystyrene concentration was reduced in the solution to 0.3% w/v, the monolayer order and particle concentration in the substrate decreased at a withdrawal speed of 1 mm/min as it was also described by Y. Wang et al., [68]. Therefore, when particle concentration is too low, an insufficient upward flow of particles is provided to the substrate resulting in a loss of monolayer uniformity and isolated regions forming scattered small islands. On the contrary, low solution concentration but high withdrawal speed of 90 mm/min increased the surface coverage of particles adhered to the substrate although the well-ordered arrangement was less promoted. This dependency is described by the change from the capillary regime to the viscous drag regime in Landau-Levich model [69]. This regime is enclosed between lifting velocities of 60mm/min-600mm/min and based on the preeminent role of viscous drag forces to transfer the liquid onto the substrate together with a quick drying. The Landau-Levich model increases the film thickness while increasing the withdrawal speed at a power of 2/3 [70] whereas the deposition rate of capillary regime is inversely proportional to the withdrawal speed. The evaporation regime studied was carried out at a low withdrawal speed and the results obtained in particle coverage and monolayer self-assembly fulfill the equation 1.31 for 2D growth of particle array.

The solvent used in the colloidal suspension was always a mixture of water and ethanol in a volume ratio of 1:1 since experimental results provided better surface coverage. When a volume ratio of 4:1 water:ethanol was used, several island of particles were found on the substrate most probably because the high surface tension that gave rise to a thick meniscus with a low evaporation rate and a subsequent low particle flux. On the contrary, when volume ratio of 1:4 water:ethanol was used, disordered packing was found. Although the fast evaporation rate of ethanol produces high particle flux, the low surface tension causes small capillary forces insufficient to compress the particles in a well-ordered monolayer.

The most suitable withdrawal speed was found at 1mm/min, the minimum speed attainable by the equipment. Presumably, even lower lifting speeds would have procured larger densely-packed monolayers as well as the control of the temperature and humidity of the surrounding atmosphere.

4.3 Monolayer Self-assembly by Langmuir-Blodgett

It is well known that the hydrophobic properties play an important role in the assembly of highly-ordered monolayers through Langmuir-Blodgett method. The polystyrene particles were grafted with poly(acrylic acid), a synthetic polymer based on the hydrophilic acrylic acid that may cause the polystyrene particles to sink in the water subphase as probably happened for most of the material loss when PS_{350} was used. However, polystyrene of ~2μm remain in the interface to a great extent. Obviously, this interfacial behavior is presumably provided by a balance between hydrophobic and hydrophilic interactions leading to the conclusion that acrylic acid is less densely grafted on PS_2 than on PS_{350} favoring flotation. The effect of surface pressure on the LB monolayer shows a marked steep π-A isotherm at the solid phase, low compressibility and lower values of Area/particle than theoretically calculated when the monolayer is densely packed. The π-A isotherm shape and phase transitions agrees with other studies in monolayer and multilayer self-assembly of colloidal particles deposited by Langmuir-Blodgett methods [71]. The shift of the isotherm curve towards lower areas per molecule is probably connected with the drag of polystyrene particles into the subphase under the ethanol influence. Water-soluble solvents used as spreading solvents such as ethanol enhance the material solubility and hence the film loss, being the polystyrene solubilization into the bulk phase the main issue during the spreading step. The appearance of the liquid phase in the π-A isotherm of PS_{350} seems to be a consequence of solvent influence in the interface since solvent molecules penetrate the monolayer and remain on the subphase. A. Gericke et al., [72] proposed that ethanol molecules may stay in the hydrophobic surface film or influence the adjacent water molecules. Therefore, ethanol affects the water surface tension by decreasing it and the surface pressure by increasing the molecular concentration in the interface. In this way the transition between gaseous state to solid state could be described by an accumulation of solvent molecules on the water surface together with a considerable loss of polystyrene particles. As the area/particle available is reduced, the surface pressure is constantly increased by solvent molecules repulsion. More and more polystyrene particles remaining on the surface come into contact with an eventual change in the slope that indicates the solid monolayer formation. At this high surface pressure solvent molecules are squeezed out from the monolayer and the film transfer is feasible. However, Figure 3.31 shows the poor film transfer onto the silicon substrate meaning that the steep slope related to the solid phase is a combination of the increase in particle concentration and solvent molecules with a high surface pressure but in a submonolayer arrangement. The low particle coverage suggests that the loss of material could be larger than the supposed experimental value found when the monolayer is densely packed. On the contrary, PS_2 after film transfer during the solid phase shows better coverage, order and packing as seen in Figure 3.26 and Figure 3.28 despite of the material loss. The 2D structure is similar to the particle films formed by S. Reculusa et al., [73] which provided well-packed domains and dense films with particles that exhibited carboxylic groups in their surface. The improved order in the latter figure could be related to more homogeneously spreading of the polystyrene particles in the initial available area from a less concentrated colloidal solution. However, even more diluted solutions (data not shown) brought less surface coverage on the substrate with an increase of material loss, suggesting that a balance between particle dispersion and particle solubilization into the subphase has to be optimized to provide the best self-assembled monolayers. Figure 3.28 shows a well-ordered packed monolayer with hexagonal domains demonstrating that monolayer self-assembly via Langmuir-Blodgett technique could be an effective method for hexagonally closed-packed arrangement. However there are still some defects and empty areas that should be avoided to improve the order and the hexagonal structure continuity.

One of the problems that influence the lack of perfect global order is the barrier compression during film transfer. At small withdrawal speed of 1mm/min the barriers fluctuates around the selected surface pressure for monolayer deposition in order to maintain the surface pressure constant. This continuous pressure variation could lead to monolayer rupture or loss in the hexagonal close-packed order due to an insufficient surface pressure supply. Another important factor that diminishes the order is the polydispersity of the colloidal suspension. AFM images show in more detail that the smaller particles in the self-assembled structures induce disordered patterns in the adjacent particles. The perturbations consist in loss of hexagonal order maintaining the high packing or the appearance of superior imperfections such as defect lines.

Additionally, it is necessary to take into account the steric effect introduced by the acrylic acid grafted on the surface. The air/water interface behaves as a good solvent for the grafted polystyrene and therefore the segments are positioned in a less compact distribution. When two colloidal particles approach each other, the entropic factor between PAA chains is reduced and the osmotic pressure increased leading to longer range repulsion effect. This repulsion effect is added to the fact that acrylic acid-based particles bear negative charge because of the dissociation of COOH groups. The degree of dissociation is low since acrylic acid is a weak acid that possesses low charge at low pH which increases as the pH increases. The relation between similarly charged particles plays a dominant interaction in the self-assembly arrangement and order through the screening of coulomb repulsion. Although the steric effect together with the repulsive effect could have some relation in the appearance of defects and vacancies seen in the monolayer, it is presumably not comparable with the larger influence of fluctuation of barrier compression or particle polydispersity.

The effect of the withdrawal speed clearly influences the monolayer formation. When the lifting speed is low, the particles crystallize in a monolayer in which the final order is more or less densely packed. On the contrary, when particles are transferred onto the substrate at higher velocities, the movable barriers do not match the withdrawal rate and the substrate ends up with lower particle density. Moreover, 2D crystalline structure is split in stripes and island as a result of a not adequate compression provided by the movable barriers.

Wetting behavior of particles in the monolayer at the air/water interface via contact angle measurements were attempted to be quantified by means of Wilhelmy balance in order to find a complementary technique to optical methods. The removal energy for one particle is described as:

$$E_r = \Pi_c A_c \tag{4.1}$$

Where Π_c is the collapsing pressure and A_c is the area per particle at the collapse. The assumption that the removal energy for one particle is equal to the adhesion work allows relating the equation 4.1 with 1.34 and 1.35. Additionally, for a hexagonally packed monolayer and monodispersed colloidal particles, the contact angle can be calculated with the expression proposed by Z. Hórvölgyi et al., [74]:

$$\cos\theta = \pm\left[\left\{(2(3)^{1/2}\Pi_c)/(\pi\gamma_{LA})\right\}^{1/2} - 1\right] \tag{4.2}$$

Where γ_{LA} is the liquid-air interfacial tension and θ is the contact angle between the particle and the interface. The validity of the method requires planar air/water interface, hexagonal particle arrangement and monodispersed particles. However, according with the results obtained, it is not clear that such arrangement during the collapse is achieved. Furthermore, it has been shown that the colloidal particles in the suspension are quite polydispersed with a consequent lack of homogeneity. Therefore the evaluation of the contact angle between the monolayer and the interface could be misleading or erroneous and has not been calculated.

Self-assembled monolayer through Langmuir-Blodgett technique using APTMS-treated substrate provides a range of order close to the previously obtained with hydrophilic substrates but, in both cases, without a continuous and regular hexagonal structure. Substrates functionalized with PFS results in particle agglomeration. The horizontal transfer of a monolayer onto a substrate resulted in better ordering and larger grain size with better hexagonal pattern. This implies that the conventional vertical deposition has a critical step between the compressed monolayer resting on the subphase and the vertical transfer onto the substrate. The deterioration of the monolayer quality during the vertical deposition could be related to the low mobility of polystyrene that hinders the rearrangement due to an excessive friction between particles, i.e., high surface energy. Additionally, when the horizontal transfer was carried out from the top of the film by touching the monolayer with PFS-treated substrate, the deposition was markedly difficult or impossible. Therefore, it could be inferred that the polystyrene particles are not totally hydrophobic and the affinity for this substrate is reduced. On the contrary, due to that hydrophilicity-hydrophobicity particle duality, polystyrene particles show more affinity for APTMS substrate with 60º contact angle than for very hydrophilic substrates.

5 Conclusion

Substrate wetting properties showed a strong influence in self-assembly processes of colloidal monolayers. For large contact angles the convective flow of nanospheres is excessively fast and particles pile on preceding layers in an amorphous deposition causing ring growth or cluster aggregation. The optimal wetting behavior for monolayer self-assembly on silicon substrates is observed for contact angles not exceeding a few degrees. However, self-assembled monolayers of silica nanospheres were unsatisfactory attempted to arrange in a two-dimensional structure as a mask for lithographic nanopatterning. Colloidal silica particles are strongly dominated by adhesion forces that promote the molecular aggregation and weakly influenced by lateral capillary forces between small particles during the evaporation process.

On the contrary self-assembled monolayers of polystyrene particles in droplet evaporation were successfully arranged in highly ordered hexagonal packing with smaller ordered areas in case of polystyrene particles of 2µm diameter, since the higher polydispersity affects the packing order which is considerably dependent on the fast evaporation process.

The coating procedure for continuous fabrication of two-dimensional monolayers by Dip-coating method mainly relies on the synchronization between the withdrawal speed and the evaporation rate. The monolayer structure and its final extension over the substrate are extensively influenced by the solution concentration, solution solvent, immersion time, withdrawal speed and humidity. The most convenient particle flux towards the substrate was found with a solution mixture of ethanol:water in a volume ratio1:1 since larger ratios of ethanol or water produce small capillary forces or low particle flow respectively. Regarding the withdrawal speed, closely-packed arrangement was obtained at the lowest speed provided by the apparatus suggesting that even lower velocities could have extended the monolayer coverage onto the substrate.

Monolayer films of polystyrene colloidal particles prepared by Langmuir-Blodgett method contained hcp crystalline domains together with defects due to a lack of barrier compression. The largest well-ordered domains with the least amount of defects were achieved with PS_2. The π-A isotherm showed a loss of material due to particle solubilization into the bulk phase based on the use of ethanol as spreading solvent and the hydrophilic poly(acrylic acid) grafted on the polystyrene surface. This solubilization phenomenon is one of the main drawbacks for the monolayer formation at the air/water interface being more accused for PS_{350} which also showed ethanol penetration into the monolayer film. The lack of perfect global order in a well-ordered monolayer is highly influenced by the inability of barrier compression to maintain the surface pressure constant during film transfer and to a lesser extent by the stearic effect and electrostatic repulsion introduced by the PAA chains.

Bibliography

[1] J. Dutta and H. Hofmann, “Self-organization of colloidal nanoparticles,” *Encyclopedia of Nanoscience and Nanotechnology*, vol X. pp. 1-23, 2003.

[2] S.M. Yang, S. G. Jang, D.G. Choi, S. Kim and H. K. Yu, “Nanomachining by Colloidal Lithography,” *Small*, vol 2, pp. 458-475, 2006.

[3] P. Colson, C. Henrist and R. Cloots, “Nanosphere Lithography: A Powerful Method for the Controlled Manufacturing of Nanomaterials,” *J. Nanomater*, vol. 203, pp. 1-19, 2013.

[4] S. Okazaki, “Resolution limits of optical lithography,” *Journal of Vacuum Science & Technology B*, vol. 9, pp. 2829–2833, 1991.

[5] G. Gerlach and K.-J. Wolter, *Bio and Nano Packaging Techniques for Electron Devices*. Springer-Verlag Berlin Heidelberg, 2012, ISBN: 978-3-642-28522-6, pp. 269-277

[6] Y. Xia and G. M. Whitesides, “Soft lithography,” *Angewandte Chemie*, vol. 37, pp. 550–575, 1998.

[7] B. D. Gates, Q. Xu, M. Stewart, D. Ryan, C. G. Willson and G. M. Whitesides, “New approaches to nanofabrication: molding, printing, and other techniques,” *Chemical Reviews*, vol. 105, pp. 1171–1196, 2005.

[8] R.Garcia,R.V.Martinez and J.Martinez, “Nano-chemistryand scanning probe nanolithographies,” *Chemical Society Reviews*, vol. 35, pp. 29–38, 2006.

[9] M. Rycenga, P. H. C. Camargo and Younan Xia, “Template-assisted self-assembly: a versatile approach to complex micro- and nanostructures,” *Soft Matter*, vol. 5, pp. 1129-1136, 2009.

[10] D. Bratton, D. Yang, J. Dai, and C. K. Ober, “Recent progress in high resolution lithography,” *Polymers for Advanced Technologies*, vol. 17, no. 2, pp. 94–103, 2006

[11] M. P. Pileni, Y. Lalatonne, D. Ingert, I. Lisiecki, and A. Courty, “Self assemblies of nanocrystals: preparation, collective properties and uses,” *Faraday Discussions*, vol. 125, pp. 251–264, 2004.

[12] J. D Halley and D.A Winkler, "Consistent Concepts of Self-organization and Self-assembly", Wiley Periodicals, Vol. 14, no. 2, pp. 10–1, 2008.

[13] S. Camazine, J.L. Deneubourg, N Franks, G. Theraulaz and E. Bonabeau, *Self-Organization in Biological Systems*. Princeton University Press, 2001, ISBN: 9780691116242.

[14] J. A. Pelesko, *Self assembly: the science of things that put themselves together*. New York, NY: Chapman & Hall/ CRC, 2007, ISBN: 978-1-58488-688-4

[15] G. M. Whitesides and M. Boncheva, "*Beyond molecules: Self-assembly of mesoscopic and macroscopic components*," Proc Natl Acad Sci, vol. 99, no. 8, pp. 4769–4774, 2002.

[16] G.M Whitesides. and B. Grzybowski, "Self-assembly at all scales," *Science,* vol. 295, pp.2418-2421, 2002

[17] T. Yamaguchi, N. Suematsu and H Mahara, "Self-organization of hierarchy: Dissipative-structure assisted self-assembly of metal nanoparticles in polymer matrices," *Nonlin Dyn Polym Syst*, vol.869, pp. 16–27, 2004.

[18] R. Gabai, A. Ismach, and E. Joselevich "Nanofacet Lithography: A New Bottom-Up Approach to Nanopatterning and Nanofabrication by Soft Replication of Spontaneously Faceted Crystal Surfaces," *Adv. Mater.*, vol 19, pp 1325–1330, 2007.

[19] G. Zhang and D. Wang, "Colloidal Lithography—The Art of Nanochemical Patterning," *Chem. Asian J.*, vol. 4, pp. 236 – 245, 2009.

[20] R. W. Whatmore, "Nanotechnology: big prospects for small engineering," *Ingenia*, pp. 28–34, 2001

[21] R.A.L. Jones, *Soft Condensed Matter*. New York, Oxford University Press, 2002, ISBN: 0-19-850589-2

[22] H-J. Butt, K. Graf and M. Kappl, *Physics and Chemistry of Interfaces*. Weinheim, WILEY-VCH Verlag GmbH & Co., 2003, ISBN 3-527-40413-9

[23] J.N. Israelachvili, *Intermolecular and Surface Forces*. Santa Barbara, Elsevier inc., 2011, ISBN: 978-0-12-391927-4.

[24] D. F. Williams and J. C. Berg, "The aggregation of colloidal particles at the air—water interface," *Journal of Colloid and Interface Science*, Vol. 152 ,pp. 218–229, 1992.

[25] D Shaw, *Introduction to Colloid and Surface Chemistry*. Elsevier Science Ltd., 1992 ISBN: 0-7506-1182-0

[26] P. Pieranski, "Two-Dimensional Interfacial Colloidal Crystals," *Phys. Rev. Lett.*, vol 45, pp 569, 1980

[27] Q. Li, U. Jonas, X. S. Zhao and M. Kappl, “The forces at work in colloidal self-assembly: a review on fundamental interactions between colloidal particles,” *Asia-Pac. J. Chem. Eng*. vol. 3, pp. 255–268, 2008.

[28] P. A. Kralchevskyt and K. Nagayama, “Capillary Forces between Colloidal Particles,” Langmuir, vol 10, pp. 23-36, 1994.

[29] P. A. Kralchevsky, V. N. Paunov, I. B. Ivanov and K. Nagayama, “Capillary Meniscus Interaction between Colloidal Particles Attached to a Liquid-Fluid Interface,” *Journal of Colloid and lnterface Science*, vol 151, pp. 79-94, 1992

[30] P.A. Kralchevsky, and N. D. Denkov, “Capillary forces and structuring in layers of colloid particles,” *Current Opinion in Colloid & Interface Science*, vol 6, pp.383- 401, 2001

[31] P.A. Kralchevsky and K. Nagayama, “Capillary interactions between particles bound to interfaces, liquid films and biomembranes,” *Advances in Colloid and Interface Science*, vol. 85, pp. 145-192, 2000.

[32] V. N. Paunov, P. A. Kralchevsky, N. D. Denkov and K. Nagayama, “ Lateral Capillary Forces Between Floating Submillimeter Particles.” *Jorunal of Colloid Interface Science*, vol.157**,** pp. 100-112, 1993.

[33] P.A. Kralchevsky and K. Nagayama, Particles at fluid interfaces and membranes: attachment of colloid particles and proteins to interfaces and formation of two-dimensional arrays. Elsevier, 2001, ISBN: 0-444-50234-3, pp. 321-328.

[34] P.G. de Gennes, “Polymers at an interface,” *Adv. Colloid Interface Sci*., vol.27, pp. 189-209, 1987.

[35] Y.Yu and G Zhang, *Colloidal Lithography*, Updates in Advanced Lithography, InTech, 2013.

[36] U. C. Fischer and H. P. Zingsheim, “Submicroscopic pattern replication with visible light,” *Journal of Vacuum Science & Technology*, vol. 19, no. 4, pp. 881–885, 1981.

[37] H. W. Deckman and J. H. Dunsmuir, “Natural lithography,” *Applied Physics Letters*, vol. 41, no. 4, pp. 377–379, 1982.

[38] J. C. Hulteen and R. P. Van Duyne, “Nanosphere lithography: a materials general fabrication process for periodic particle array surfaces,” *Journal of Vacuum Science and Technology A*, vol. 13, no. 3, pp. 1553–1558, 1995.

[39] X. Ye and L. Qi, “Two-dimensionally patterned nanostructures based on monolayer colloidal crystals: Controllable fabrication, assembly, and applications” *Nano Today*, vol 6, pp. 608—631, 2011.

[40] C. L. Haynes and R. P. Van Duyne, “Nanosphere Lithography: A Versatile Nanofabrication Tool for Studies of Size-Dependent Nanoparticle Optics,” *J. Phys. Chem. B*, vol. 105, pp. 5599-5611, 2001.

[41] N. D Denkov, 0. D Velev, P. A Kralchevsky, I. B Ivanov, H. Yoshimura and K. Nagayama, “Two-dimensional crystallization,” *Nature*, vol 2, pp. 361, 1993.

[42] K. Nagayama, “Two-dimensional self-assembly of colloids in thin liquid films,” *Colloids Surfaces A*, vol 109, pp. 363-374, 1996.

[43] R. D. Deegan, O. Bakajin, T. F. Dupont, G. Huber, S. R. Nagel and T. A. Witten, “ Capillary flow as the cause of ring stains from dried liquid drops,” *Nature*, vol 389, pp. 827-829, 1997.

[44] C.D. Dushkin, H. Yoshimura and K. Nagayama, “Nucleation and growth of two-dimensional colloidal crystals,” *Chemical Physics Letters*, vol. 204, pp. 6455–6460, 1993.

[45] T. Schneller, R. Waser, M. Kosec and D. Payne, *Chemical Solution Deposition of Functional Oxide Thin films*, Springer, 2013, ISBN: 978-3-211-99311-8

[46] A. S. Dimitrov and K.Nagayama, “Continuous Convective Assembling of Fine Particles into Two-Dimensional Arrays on Solid Surfaces,” *Langmuir*, vol. 12, pp. 1303-1311, 1996.

[47] Y.Wang, L. Chen, H. Yang, Q. Guo, W. Zhou and M. Tao, “ Large-area self assembled monolayers of silica microspheres formed by dip coating,” *Materials Science-Poland*, vol. 28, no. 2, pp. 468-478, 2010.

[48] D.K. Martin, *Nanobiotechnology of Biomimetic Membranes*, Springer, 2007, ISBN: 978-0-387-37740-7, pp. 23-74.

[49] Krister Holmberg, *Handbook of Applied surface and Colloid Chemistry*. Wiley, 2001, ISBN: 978-0-471-49083-8, pp. 629-635.

[50] A. P. Girard-Egrot, S. Godoy and L. J. Blum, “Enzyme association with lipidic Langmuir – Blodgett films: Interests and applications in nanobioscience,” *Adv. in Coll. and Interf. Sci*, vol. 116, pp. 205-225, 2005.

[51] Bernard P. Binks, “Particles as surfactants-similarities and differences,” *Curr. Opinion in Colloid & Interface Sci.*, vol. 7, pp.21-41, 2002.

[52] M. Bardosova, M. E. Pemble , I. M. Povey , and R. H. Tredgold, “The Langmuir-Blodgett Approach to Making Colloidal Photonic Crystals from Silica Spheres,” *Adv. Mater.*, vol. 22, pp.3104–3124, 2010.

[53 A. Gil, M. Vaupel, F. Guitiana and D. Möbius, “Stress-free production and effective medium model of colloidal crystals,” *J.Mater. Chem,*, vol.17, pp.2434–2439, 2007.

[54] B. van Duffel,R. H. A. Ras, F. C. De Schryver and R. A. Schoonheydt, “Langmuir–Blodgett deposition and optical diffraction of two-dimensional opal,” *J. Mater. Chem.*, vol.11, p.p. 3333–3336, 2001.

[55] S. C. Rödner, P. Wedin, and L. Bergström, “Effect of Electrolyte and Evaporation Rate on the Structural Features of Dried Silica Monolayer Films,” *Langmuir,* vol.18, p.p. 9327-9333, 2002.

[56] M. Tanemura, T. Ogawa and N. Ogita, “A new algorithm for three-dimensional voronoi tessellation,” *Comput. Phys,* Vol. 51, (2), p.p. 191-207, 1983.

[57] P. H.F. Hansen, S. C. Rödner, and L. Bergström, “Structural Characterization of Dense Colloidal Films Using a Modified Pair Distribution Function and Delaunay Triangulation,” *Langmuir*, vol.17, p.p 4867-4875, 2001.

[58] Materials Digital LibraryPathway:http://matdl.org/matdlwiki/index.php/softmatter: Radial Distribution_Function.

[59] G.Simon, “Investigation of Technical Ways to Generate Uniform Coatings of Microparticles by Convective Evaporation,” MA thesis, Columbia university, 2010.

[60] A. Stalder, T, Melchior, M. Müller , D. Sage, T. Bluc and M. Unser, “Low-bond axisymmetric drop shape analysis for surface tension and contact angle measurements of sessile drops,” *Colloids and Surfaces A: Physicochem. Eng. Aspects,* vol. 364, pp. 72-81, 2010.

[61] Tuan A. H. Nguyen and Anh V. Nguyen,” Transient Volume of Evaporating Sessile Droplets: 2/3, 1/1, or Another Power Law?,” *Langmuir*, vol. 30 (22), p.p. 6544–6547, 2014.

[62] D. Leere, L. Najbjerg, M. Christiansen, M. Jensen and T. Huynh, “Fabrication and characterization of porous alumina membranes used to grow nickel nanowires,” AAU Nanobiotechnology, 3th semester 2015.

[63] S. Mátéfi-Tempfli , M. Mátéfi-Tempfli, L. Piraux, “Characterization of nanopores ordering in anodic alumina,” *Thin Solid Films*, vol. 516, p.p 3735–3740, 2008.

[64] A. C. Johnston-Peck, J. Wang, and J. B. Tracy, “Formation and Grain Analysis of Spin-Cast Magnetic Nanoparticle Monolayers,” *Langmuir*, vol.27 (8), p.p. 5040–5046 2011

[65] F. Burmeister, W. Badowsky, T. Braun, S. Wieprich, J. Boneberg and P. Leiderer “Colloid monolayer lithography-A flexible approach for nanostructuring of surfaces,” *Applied Surface Science*, vol. 144–145, p.p. 461–466, 1999.

[66] S. Rakers, L. F. Chi and H. Fuchs, “Influence of the Evaporation Rate on the Packing Order of Polydisperse Latex Monofilms,” *Langmuir,* vol. 13, p.p. 7121-7124, 1997.

[67] Z. Lu and M. Zhou, “Fabrication of large scale two-dimensional colloidal crystal of polystyrene particles by an interfacial self-ordering process,” *Journal of Colloid and Interface* Science, vol. 361, p.p.429–435, 2011.

[68] Y.Wang, H. Yang, L. Chen, W. Zhou, M. Tao, and Q. Guo, “Solution Processed Large Area Surface Textures Based on Dip Coating,” *Nanotechnology IEEE Conference on*, pp. 771-774, 2008.

[69] L. Landau and B. Levich, “Dragging of a Liquid by a Moving Plate,” *Acta Physicochimica*, vol. 17, no. 42, pp. 42-54, 1942.

[70] D. Grosso, “How to exploit the full potential of the dip-coating process to better control film formation,” *J. Mater. Chem.*, vol. 21, pp.17033-1738, 2011.

[71] M. Szekeres, O. Kamalin, R. A. Schoonheydt, K. Wostyn, K. Clays, A. Persoonsc and Imre Dékány, “Ordering and optical properties of monolayers and multilayers of silica spheres deposited by the Langmuir–Blodgett method,” *J. Mater. Chem.*, vol 12, p.p. 3268–3274, 2002.

[72] A. Gericke, J. Simon-Kutscher and H. Huhnerfuss, “Influence of the Spreading Solvent on the Properties of Monolayers at the Air/Water Interface,” *Langmuir*, vol.9, p.p. 2119-2127, 1993.

[73] S. Reculusa, R. Perrier-Cornet, B. Agricole, V. Héroguez, T. Buffeteau and S. Ravaine, “ Langmuir–Blodgett films of micron-sized organic and inorganic colloids,” *Phys. Chem. Chem. Phys.*, vol. 9, p.p. 6385–6390, 2007.

[74] Z. Horvölgyi, M. Máté, A. Dániel and J. Szalma, “Wetting behaviour of silanized glass microspheres at water-air interfaces: a Wilhelmy film balance study,” *Colloids and Surfaces A: Physicochem. Eng. Aspects*, vol. 156, p.p. 501–507, 1999.

Appendix A

A.1 Nanoparticle tracking Analysis of silica particles

The full report of results regarding average particle size and concentration depending on the measurements and analysis conditions is shown in figure A.1.

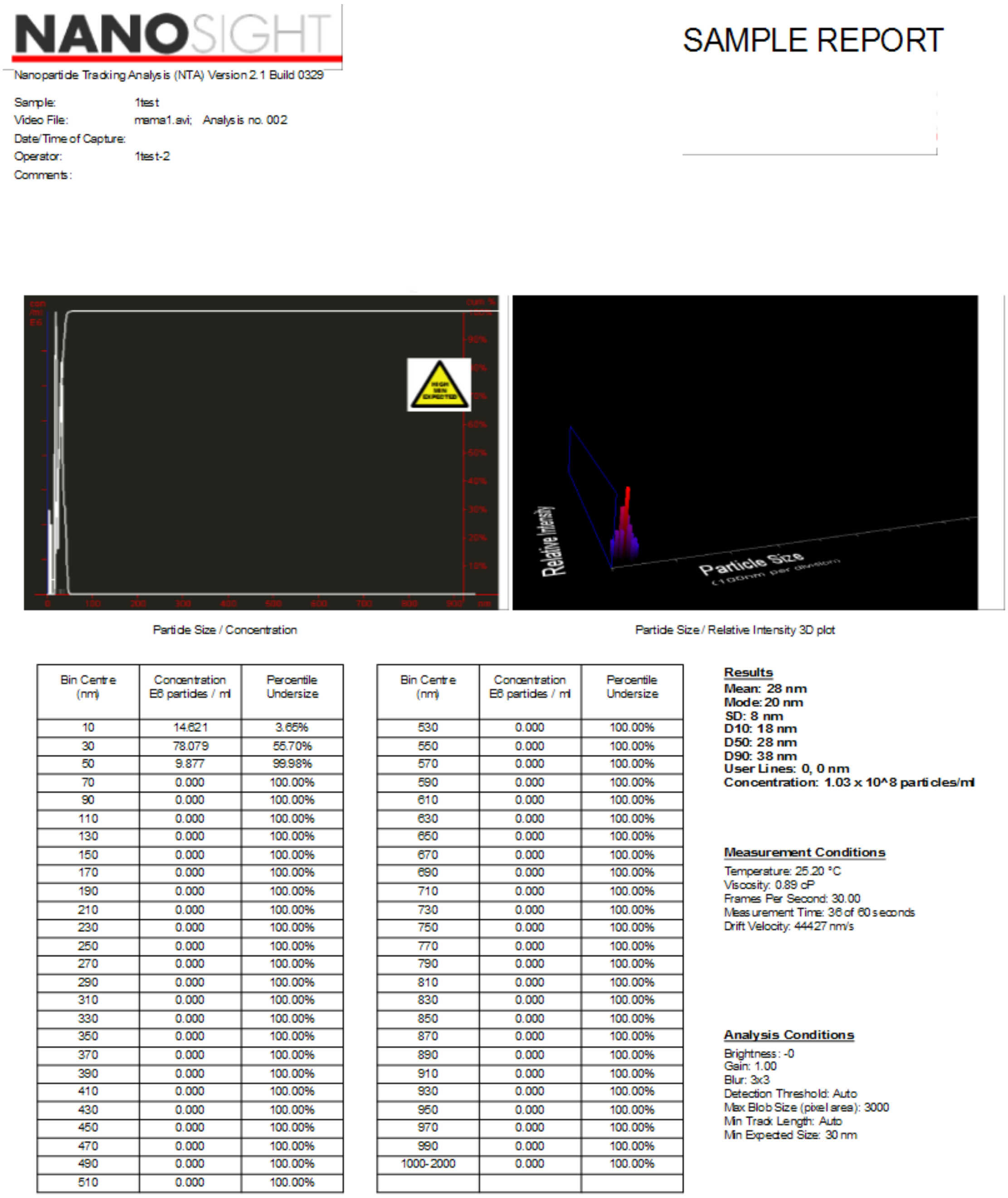

NANOSIGHT

Nanoparticle Tracking Analysis (NTA) Version 2.1 Build 0329

SAMPLE REPORT

Sample: 1test
Video File: mama1.avi; Analysis no. 002
Date/Time of Capture:
Operator: 1test-2
Comments:

Particle Size / Concentration

Particle Size / Relative Intensity 3D plot

Bin Centre (nm)	Concentration E6 particles / ml	Percentile Undersize
10	14.621	3.65%
30	78.079	55.70%
50	9.877	99.98%
70	0.000	100.00%
90	0.000	100.00%
110	0.000	100.00%
130	0.000	100.00%
150	0.000	100.00%
170	0.000	100.00%
190	0.000	100.00%
210	0.000	100.00%
230	0.000	100.00%
250	0.000	100.00%
270	0.000	100.00%
290	0.000	100.00%
310	0.000	100.00%
330	0.000	100.00%
350	0.000	100.00%
370	0.000	100.00%
390	0.000	100.00%
410	0.000	100.00%
430	0.000	100.00%
450	0.000	100.00%
470	0.000	100.00%
490	0.000	100.00%
510	0.000	100.00%

Bin Centre (nm)	Concentration E6 particles / ml	Percentile Undersize
530	0.000	100.00%
550	0.000	100.00%
570	0.000	100.00%
590	0.000	100.00%
610	0.000	100.00%
630	0.000	100.00%
650	0.000	100.00%
670	0.000	100.00%
690	0.000	100.00%
710	0.000	100.00%
730	0.000	100.00%
750	0.000	100.00%
770	0.000	100.00%
790	0.000	100.00%
810	0.000	100.00%
830	0.000	100.00%
850	0.000	100.00%
870	0.000	100.00%
890	0.000	100.00%
910	0.000	100.00%
930	0.000	100.00%
950	0.000	100.00%
970	0.000	100.00%
990	0.000	100.00%
1000-2000	0.000	100.00%

Results

Mean: 28 nm
Mode: 20 nm
SD: 8 nm
D10: 18 nm
D50: 28 nm
D90: 38 nm
User Lines: 0, 0 nm
Concentration: 1.03 x 10^8 particles/ml

Measurement Conditions

Temperature: 25.20 °C
Viscosity: 0.89 cP
Frames Per Second: 30.00
Measurement Time: 36 of 60 seconds
Drift Velocity: 44427 nm/s

Analysis Conditions

Brightness: -0
Gain: 1.00
Blur: 3x3
Detection Threshold: Auto
Max Blob Size (pixel area): 3000
Min Track Length: Auto
Min Expected Size: 30 nm

Figure A.1: *NTA full report of silica particle analysis and size distribution.*

A.2 Nanoparticle size analysis by ImageJ

Statistical analysis of particle diameter is based on the number of particles recognized and collected by ImageJ software from the image provided. All particles with their corresponding diameter and occupied area are listed in table A.1 and table A.2.

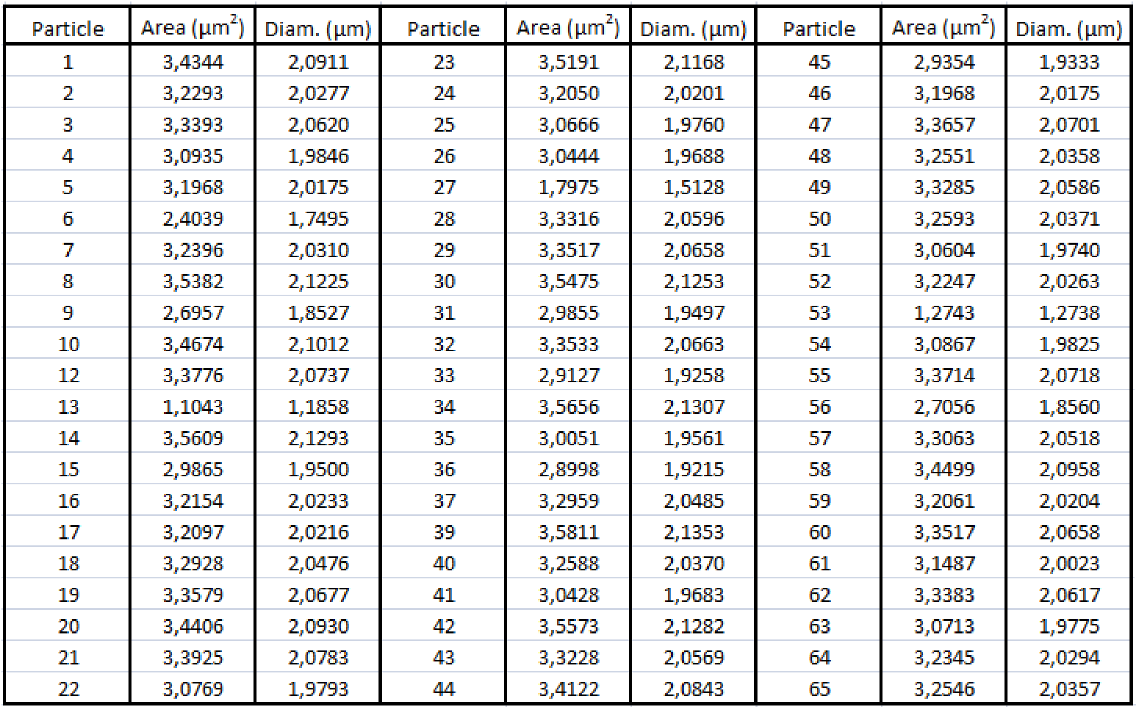

Particle	Area (μm^2)	Diam. (μm)	Particle	Area (μm^2)	Diam. (μm)	Particle	Area (μm^2)	Diam. (μm)
1	3,4344	2,0911	23	3,5191	2,1168	45	2,9354	1,9333
2	3,2293	2,0277	24	3,2050	2,0201	46	3,1968	2,0175
3	3,3393	2,0620	25	3,0666	1,9760	47	3,3657	2,0701
4	3,0935	1,9846	26	3,0444	1,9688	48	3,2551	2,0358
5	3,1968	2,0175	27	1,7975	1,5128	49	3,3285	2,0586
6	2,4039	1,7495	28	3,3316	2,0596	50	3,2593	2,0371
7	3,2396	2,0310	29	3,3517	2,0658	51	3,0604	1,9740
8	3,5382	2,1225	30	3,5475	2,1253	52	3,2247	2,0263
9	2,6957	1,8527	31	2,9855	1,9497	53	1,2743	1,2738
10	3,4674	2,1012	32	3,3533	2,0663	54	3,0867	1,9825
12	3,3776	2,0737	33	2,9127	1,9258	55	3,3714	2,0718
13	1,1043	1,1858	34	3,5656	2,1307	56	2,7056	1,8560
14	3,5609	2,1293	35	3,0051	1,9561	57	3,3063	2,0518
15	2,9865	1,9500	36	2,8998	1,9215	58	3,4499	2,0958
16	3,2154	2,0233	37	3,2959	2,0485	59	3,2061	2,0204
17	3,2097	2,0216	39	3,5811	2,1353	60	3,3517	2,0658
18	3,2928	2,0476	40	3,2588	2,0370	61	3,1487	2,0023
19	3,3579	2,0677	41	3,0428	1,9683	62	3,3383	2,0617
20	3,4406	2,0930	42	3,5573	2,1282	63	3,0713	1,9775
21	3,3925	2,0783	43	3,3228	2,0569	64	3,2345	2,0294
22	3,0769	1,9793	44	3,4122	2,0843	65	3,2546	2,0357

Table A.1: *Number of polystyrene particles with a diameter of approximately 2μm collected by ImageJ and the subsequent area and diameter analysis.*

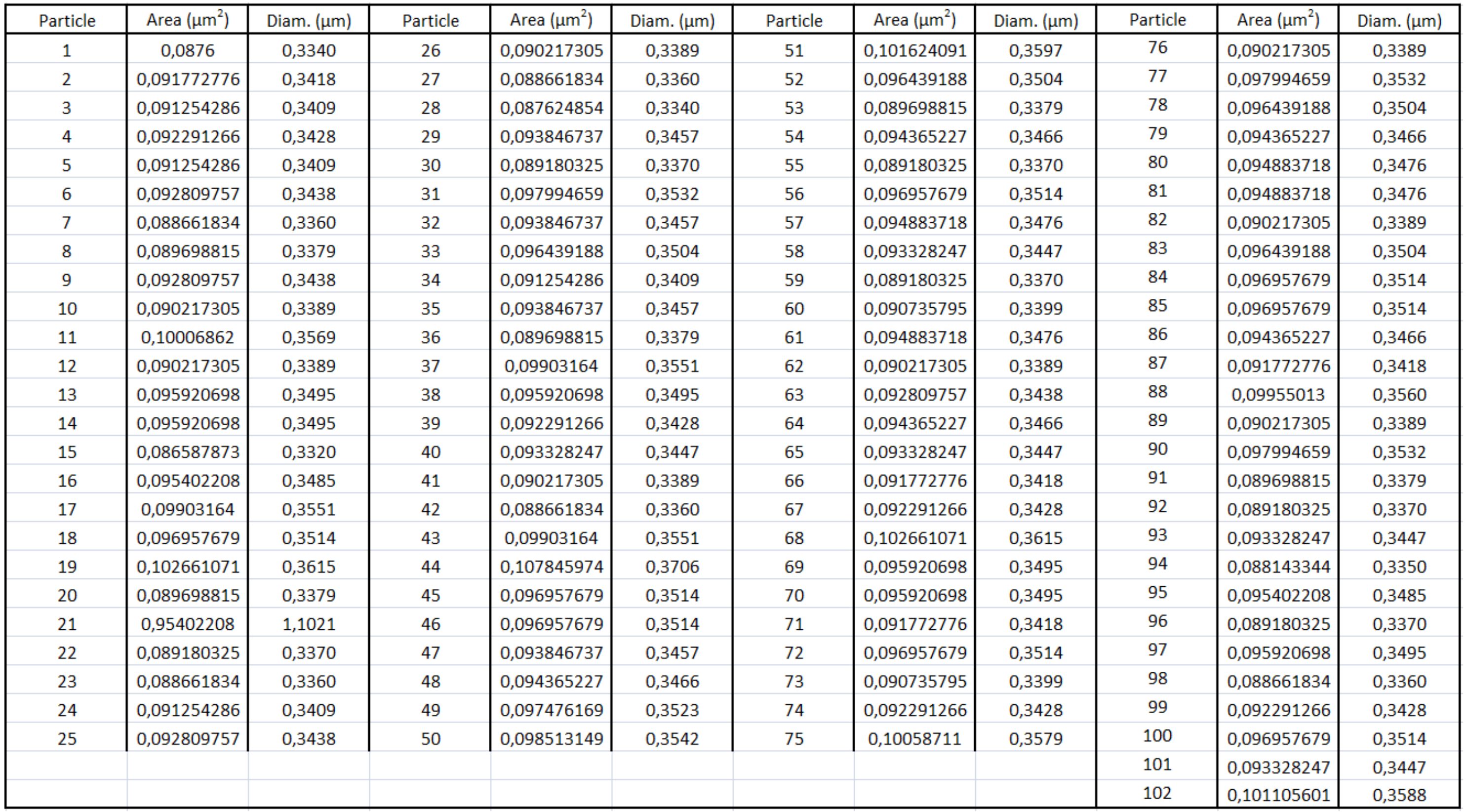

Particle	Area (μm^2)	Diam. (µm)	Particle	Area (μm^2)	Diam. (µm)	Particle	Area (μm^2)	Diam. (µm)	Particle	Area (μm^2)	Diam. (µm)
1	0,0876	0,3340	26	0,090217305	0,3389	51	0,101624091	0,3597	76	0,090217305	0,3389
2	0,091772776	0,3418	27	0,088661834	0,3360	52	0,096439188	0,3504	77	0,097994659	0,3532
3	0,091254286	0,3409	28	0,087624854	0,3340	53	0,089698815	0,3379	78	0,096439188	0,3504
4	0,092291266	0,3428	29	0,093846737	0,3457	54	0,094365227	0,3466	79	0,094365227	0,3466
5	0,091254286	0,3409	30	0,089180325	0,3370	55	0,089180325	0,3370	80	0,094883718	0,3476
6	0,092809757	0,3438	31	0,097994659	0,3532	56	0,096957679	0,3514	81	0,094883718	0,3476
7	0,088661834	0,3360	32	0,093846737	0,3457	57	0,094883718	0,3476	82	0,090217305	0,3389
8	0,089698815	0,3379	33	0,096439188	0,3504	58	0,093328247	0,3447	83	0,096439188	0,3504
9	0,092809757	0,3438	34	0,091254286	0,3409	59	0,089180325	0,3370	84	0,096957679	0,3514
10	0,090217305	0,3389	35	0,093846737	0,3457	60	0,090735795	0,3399	85	0,096957679	0,3514
11	0,10006862	0,3569	36	0,089698815	0,3379	61	0,094883718	0,3476	86	0,094365227	0,3466
12	0,090217305	0,3389	37	0,09903164	0,3551	62	0,090217305	0,3389	87	0,091772776	0,3418
13	0,095920698	0,3495	38	0,095920698	0,3495	63	0,092809757	0,3438	88	0,09955013	0,3560
14	0,095920698	0,3495	39	0,092291266	0,3428	64	0,094365227	0,3466	89	0,090217305	0,3389
15	0,086587873	0,3320	40	0,093328247	0,3447	65	0,093328247	0,3447	90	0,097994659	0,3532
16	0,095402208	0,3485	41	0,090217305	0,3389	66	0,091772776	0,3418	91	0,089698815	0,3379
17	0,09903164	0,3551	42	0,088661834	0,3360	67	0,092291266	0,3428	92	0,089180325	0,3370
18	0,096957679	0,3514	43	0,09903164	0,3551	68	0,102661071	0,3615	93	0,093328247	0,3447
19	0,102661071	0,3615	44	0,107845974	0,3706	69	0,095920698	0,3495	94	0,088143344	0,3350
20	0,089698815	0,3379	45	0,096957679	0,3514	70	0,095920698	0,3495	95	0,095402208	0,3485
21	0,95402208	1,1021	46	0,096957679	0,3514	71	0,091772776	0,3418	96	0,089180325	0,3370
22	0,089180325	0,3370	47	0,093846737	0,3457	72	0,096957679	0,3514	97	0,095920698	0,3495
23	0,088661834	0,3360	48	0,094365227	0,3466	73	0,090735795	0,3399	98	0,088661834	0,3360
24	0,091254286	0,3409	49	0,097476169	0,3523	74	0,092291266	0,3428	99	0,092291266	0,3428
25	0,092809757	0,3438	50	0,098513149	0,3542	75	0,10058711	0,3579	100	0,096957679	0,3514
									101	0,093328247	0,3447
									102	0,101105601	0,3588

Table A.2: *Number of polystyrene particles with a diameter of approximately 350nm collected by ImageJ and the subsequent area and diameter analysis.*

Appendix B

B.1 MATLAB scripts for characterization and analysis

All MATLAB scripts used for the monolayer analysis and characterization have been included in this section keeping the MATLAB edition format to facilitate the reading and interpretation. The codes are shown with comments to clarify how the successive lines work within the functions.

B.1.1 Hexa analysis-Main function: Delaunay triangulation

```
function [DT, real_sides, real_angles, deviation] =  ...
hexa_analysis(image_name,centers,ROI_factor,max_dev,conversion_factor)
%% Inputs:
% image_name is the filename of the analyzed image typed between single
% quotes,e.g,'example.tif'

% centers is the matrix with the X and Y coordinates of the particles.

% ROI_factor modifies the area of inerest in the image to be analyzed.
% Allowed values between 0-100. (0 = 0% of the image, 100 = 100% of the
% image,normally around 80 or 90 to avoid large triangulation close to the
% edges)

% max_dev is the maximum deviation from the average triangle side and angle
% to consider a triangle well-ordered. Values between 0-100,(0 = 0%
% deviation and 100 = 100% deviation, normally around 10).

% conversion factor in nanometers/pixel is the relationship between pixels
% and the metric scale.

%% Outputs:
% Delaunay tessellation (dt)

% A matrix of sides in which each row represents one triangle with the 3
% sides, the 3 side deviations(%)and the accumulated side deviation(%).

% A matrix of angles in which each row represents one triangle with the 3
% angles,the 3 angular deviations(%)and the accumulated angular deviation(%)

% matrix with the mean angular deviation(%),the mean side deviation(%),
% the well ordered area occupied(%),the average side in nanometers, the
% total ordered area in um and the total area analyzed in the image in um.

%%
% Delaunay Triangulation based on the particle centers.
DT = delaunayTriangulation(centers);
```

```
% Display the triangulation as a plot with numbered triangles:
figure
imshow(image_name)
hold on
triplot(DT);
ic = incenter(DT);
numtri = size(DT,1);
trilabels = arrayfun(@(x) {sprintf('T%d', x)}, (1:numtri)');
Htl = text(ic(:,1), ic(:,2), trilabels, 'FontWeight', ...
'bold', 'HorizontalAlignment', 'center', 'Color', ...
'blue');
hold off
set(gca,'visible','off')

% Get image dimensions to select the analysis area and discard points out
% of ROI
image = imread(image_name);
X = size(image, 2);
Y = size(image, 1);

% In each row of ConnectList there are 3 vertex IDs that define a triangle:
ConnectList = DT.ConnectivityList;

% Each row is the center coordinates of 1 particle (vertex):
centers = DT.Points;

% Create sides and angles to hold the 3 side lengths and the 3 angles of
% each triangle respectively. The i-th row of sides and angles is the i-th
%triangle:
sides = zeros(size(ConnectList));
angles = zeros(size(ConnectList));

% side_sum is the total sum of all triangle sides in the ROI and count the
% total number of triangle sides:
side_sum = 0;
count = 0;

% Total area occupied by all triangles and total area occupied by
% well-ordered triangles:
total_area = 0;
ordered_area = 0;

% Matrix of two vertices per row represented by coordinates X and Y whose
% distance has already been calculated:
vert_count = [0 0 0 0];

% Transparency parameter:
trans = 0.55;

% Selection of allowed triangles within the region of interest:
figure
imshow(image_name);
hold on
title('All allowed triangles')
for i = 1:length(ConnectList);

    % State variable changes if two points in the i-th triangle are
    % not within the allowed square ROI:
```

```
state = [0, 0, 0];

% Define the vertices (X,Y) of the triangle:
a = centers(ConnectList(i,1),:);
b = centers(ConnectList(i,2),:);
c = centers(ConnectList(i,3),:);

% Calculate the distance between two vertices by calling euc_distance.m:
side1 = euc_distance(a, b);
side2 = euc_distance(a, c);
side3 = euc_distance(b, c);

% if two vertices of the triangle are out of the limits of ROI, (by
% calling within_ROI.m),state variable changes to 1:
if within_ROI(X, Y,ROI_factor,a) == 1 &&...
   within_ROI(X, Y,ROI_factor,b)  == 1;
    state(1) = 1;
end
if within_ROI(X, Y,ROI_factor,a) == 1 &&...
   within_ROI(X, Y,ROI_factor,c) == 1;
    state(2) = 1;
end
if within_ROI(X, Y,ROI_factor,b) == 1 &&...
   within_ROI(X, Y,ROI_factor,c) == 1;
    state(3) = 1;
end
if state == [0, 0, 0];

    % Create coloured triangle plot to identify allowed triangles:
    h = fill([a(1) b(1) c(1)], [a(2), b(2), c(2)], 'r');
    alpha(h, trans)

    % Add the i-th allowed triangle defined by the sides to the sides'
    % matrix:
    sides(i, :) =[side1,side2,side3];

    % All triangle sides will be successively added in side_sum if and
    % only if the pair of vertices that define the side has not been
    % counted before and therefore they are not stored in vert_count
    % vector:

    if ismember([a b], vert_count, 'rows') == 0 ...
            && ismember([b a], vert_count, 'rows') == 0;
        side_sum = side_sum + side1;
        vert_count = [vert_count; a b];
        count = count + 1;
    end
    if ismember([a c], vert_count, 'rows') == 0 ...
            && ismember([c a], vert_count, 'rows') == 0;
        side_sum = side_sum + side2;
        vert_count = [vert_count; a c];
        count = count + 1;
    end
    if ismember([b c], vert_count, 'rows') == 0 ...
            && ismember([c b], vert_count, 'rows') == 0;
        side_sum = side_sum + side3;
        vert_count = [vert_count; b c];
        count = count + 1;
    end
    % Calculate the area of the allowed triangle by calling
```

```
        % triangle_area.m:
        total_area = total_area + triangle_area(side1, ...
            side2, side3);

        % Calculate the average side in pixels and nanometers from all the
        % allowed triangles:
        average_side = side_sum/count;
        average_side_nm = (side_sum*conversion_factor)/count;

        % Determine the angles of the allowed triangles by calling
        % two_point_vector.m and vector_angle.m to be allocated in the
        % matrix angles where i-th row corresponds with the 3 angles of the
        % i-th triangle:

        % Angle A:
        AB = two_point_vector(a, b);
        AC = two_point_vector(a, c);
        angles(i,1) = [vector_angle(AC, AB, side1, side2)];

        % Angle B:
        BC = two_point_vector(b, c);
        BA = two_point_vector(b, a);
        angles(i,2) = [vector_angle(BC, BA, side3, side1)];

        % Angle C:
        CA = two_point_vector(c, a);
        CB = two_point_vector(c, b);
        angles(i,3) = [vector_angle(CA, CB, side2, side3)];

    % If two vertices of a triangle are out of the ROI, the triangle is
    % not allowed and eliminated by overwriting a zeros row on the vertex
    % IDs of the i-th triangle. A zeros row is also introduced in sides and
    % angles matrices to maintain the procedure integrity:
    else
        ConnectList(i,:) = [0 0 0];
        sides(i,:) = [0 0 0];
        angles(i,:) = [0 0 0];
    end
end
hold off

% Create a list to remove the zeros rows:
remove = [];
for i = 1:length(ConnectList);
    if ConnectList(i,:) == [0 0 0];
        remove = [remove, i];
    end
end

% Remove disallowed triangles from ConnectList, sides and angles matrices:
real_ConnectList = removerows(ConnectList, remove);
real_sides = removerows(sides, remove);
real_angles = removerows(angles, remove);

%% All triangle sides are added to the side_list list. The side deviation
% in percentage is calculated over the average side length and stored in
% the matrix side_dev where each row represents a triangle with the 3 side
% deviations.The triangle_sum_dev_list is a list with the total accumulated
% deviation of each triangle in percentage:
side_list = [];
```

```
side_dev = zeros(size(real_sides));
triangle_sum_dev_list = [];

for i = 1:length(real_sides);
    triangle_sum_dev = 0;
    for j = 1:3;
        side_list = [side_list, real_sides(i, j)];
        side_dev(i, j) = (1/(3*average_side))*abs((real_sides(i, j)...
                          -average_side))*100;
        triangle_sum_dev = triangle_sum_dev + side_dev(i, j);
    end
    triangle_sum_dev_list = [triangle_sum_dev_list; triangle_sum_dev];
end

% real_sides is a matrix in which each row represents 1 triangle with
% the 3 sides, the 3 side deviations and the total accumulated deviation:
real_sides = [real_sides, side_dev, triangle_sum_dev_list];

% Mean side in nanometers:
mean_in_nm = mean(side_list)*conversion_factor;

%% All triangle angles are added to the ang_list list. The angular deviation
% in percentage is calculated over the deviation from 60 degrees and stored
% in the matrix ang_dev where each row represents a triangle with the 3
% angular deviations. The ang_sum_dev_list is a list with the total
% accumulated deviation of each triangle in percentage:
ang_list = [];
ang_dev = zeros(size(real_angles));
ang_sum_dev_list = [];

for i = 1:length(real_sides);
    ang_sum_dev = 0;
    for j = 1:3;
        ang_list = [ang_list, real_angles(i, j);];
        ang_dev(i, j) = ((1/180)*abs(real_angles(i, j) - (60))*100);
        ang_sum_dev = ang_sum_dev + ang_dev(i, j);
    end
    ang_sum_dev_list = [ang_sum_dev_list; ang_sum_dev];
end

% real_angles is a matrix in which each row represents 1 triangle with
% the 3 angles, the 3 angular deviations from 60º and the total accumulated
% angular deviation:
real_angles = [real_angles, ang_dev, ang_sum_dev_list];

%% Triangles are filled with different colors depending on the maximum
% deviation criteria introduced in percentage by the user (max_dev):

figure
imshow(image_name);
hold on
title('Triangulation: ordered(colored), non-orderedtriangles (white)')

for i = 1:length(real_ConnectList);

    % Define the vertices of triangle:
    a = centers(real_ConnectList(i,1),:);
    b = centers(real_ConnectList(i,2),:);
    c = centers(real_ConnectList(i,3),:);
```

```
    % Triangles with both total angular deviation and total side deviation
    % less than the max_dev are colored green and the ordered area
    % calculated by calling triangle_area.m:
    if real_angles(i, 7) < max_dev && real_sides(i, 7) < max_dev;
        h = fill([a(1) b(1) c(1)], [a(2), b(2), c(2)], 'g');
        alpha(h, trans);
        ordered_area = ordered_area + triangle_area(real_sides(i, 1), ...
            real_sides(i, 2), real_sides(i, 3));

    % Triangles with only angular deviation less than max_dev are colored
    % blue:
    elseif real_angles(i, 7) < max_dev;
        h = fill([a(1) b(1) c(1)], [a(2), b(2), c(2)], 'b');
        alpha(h, trans);

    % Triangles with only side deviation less than max_dev are colored
    % yellow:
    elseif real_sides(i, 7) < max_dev;
        h = fill([a(1) b(1) c(1)], [a(2), b(2), c(2)], 'y');
        alpha(h, trans);

    % Triangles not satisfying any condition are colored white:
    else
        h = fill([a(1) b(1) c(1)], [a(2), b(2), c(2)], 'w');
        alpha(h, trans);
    end
end
hold off

% Calculate the mean angular deviation:
mean_ang_dev = mean(ang_sum_dev_list);

% Calculate the mean side deviation:
mean_side_dev = mean(triangle_sum_dev_list);

% Calculate the triangular degree of order (total area occupied by the green
% triangles divided by the total area occupied by all the triangles):
triangular_ordering = ordered_area/total_area*100;



% Create a variable that returns the deviation parameters and the ordered
%area in percentage and the average triangle side in nanometers:
ordered_area_um = ordered_area*(conversion_factor/1000)^2;
total_area_um=total_area*(conversion_factor/1000)^2;
deviation = [mean_ang_dev, mean_side_dev,triangular_ordering,...
            average_side_nm,ordered_area_um,total_area_um];

% Histograms of sides and angles.
figure
hold on
histogram(side_list*conversion_factor)
title('Distribution of side distances')
xlabel('triangle sides(nm)')
ylabel('Occurences')
hold off

figure
hold on
```

```
histogram(ang_list)
title('Distribtuion of angles')
xlabel('Angles (Degrees)')
ylabel('Occurences')
hold off
end
```

B.1.2 euc distance: Distance between two points

```
function[d] = euc_distance(a, b)
% Takes two points as input and returns the euclidean distance between them:
d = abs(sqrt((a(1)-b(1)).^2+((a(2)-b(2)).^2)));
end
```

B.1.3 Two point vector: Creates a vector

```
function [v] = two_point_vector(a, b)
% Creates a vector between two 2 points a and b from a to b:
v = [b(1)-a(1), b(2)-a(2)];
end
```

B.1.4 Triangle area: Calculates the triangle area

```
function[A] = triangle_area(a, b, c)
% Takes the 3 sides of a triangle as input and returns the area of the
% triangle.

% Heron's Formula:
s = (a + b + c)/2;
A = sqrt(s*(s-a)*(s-b)*(s-c));
end
```

B.1.5 Vector angle: Calculates the angle between two vectors

```
function [ang] = vector_angle(A, B, distA, distB)
% Calculates the angle between two vectors A and B knowing their modulus

% Calculates the unit vectors:
unitA = A/distA;
unitB = B/distB;

% Calculates the angle in degrees:
ang = acosd((unitA(1)*unitB(1)+unitA(2)*unitB(2)));
end
```

B.1.6 Within ROI: If the point is within the region of interest

```
function [state] = within_ROI(X, Y,ROI_factor, coords)
state=0;

% lower changes the size of the ROI.
lower = (100-ROI_factor)/200;
higher = 1 - lower;
```

```
% Check whether the x and y coordinates of the input point are within
% the region of interest:
if (coords(1) < X*lower || coords(1) > X*higher || coords(2) < Y*lower || ...
        coords(2) > Y*higher);
    state = 1;

end
```

B.1.7 Pair-Main function: Pair distribution function

```
function g=pair(centers,finalr,interval,diameter)
%% Inputs:
% centers is a matrix with the X and Y coordinates of the particles.
% finalr is the final radius selected for the ring area
% interval is the thickness of the ring area
% diameter is the average particle diameter for the radial distance
% normalization in pixels

%% Outputs:
% A matrix g in which the first column represents all radii scrutinized,
% the second column the normalized pair distribution function, the third
% column the number of particles at a certain radial distance and the fourth
% column the ring area of each radial distance.

% Maximum and minimum values of all particles coordinates in the image:
    maxX = max(centers(:,1));
    maxY = max(centers(:,2));
    minX = min(centers(:,1));
    minY = min(centers(:,2));

% Maximum radius allowed:
maxr= min(((maxX-minX)/2),((maxY-minY)/2));

% validate the maximum radius selected:

  if maxr < finalr
        error ('The maximum allowed final radius is %d ', maxr);
  end
 % num is the total number of particles:
    [num,junk] = size(centers);

 % Total area of interest and average particle density:
    totalarea = (maxX-minX)*(maxY-minY);
    dens = num/totalarea;

    r = zeros(num,1);

    % Each particle in the image is selected and the distance between the
    % rest of particles calculated. The i-th row of R represents the i-th
    % particle with the corresponding distances formed with the rest of
    % particles:
    for m=1:num
        for n=1:num
            R(m,n)=norm(centers(m,:)-centers(n,:));
        end
    end

    g = zeros(100,4);
    iter = ceil(finalr/interval);
```

```
    for i = 1:iter
        radius = i*interval;
        inn = radius-interval;
        count=0;
        ringarea = 0;
        for m=1:num
            % Check if the ring area centered in the i-th particle is out
            % of bonds:
            if ((centers(m,1)-radius < minX) | (centers(m,1)+radius > maxX))
                continue
            elseif ((centers(m,2)-radius < minY) | ...
                    (centers(m,2)+radius > maxY))
                continue
            else
                % If the particle is accepted, the ring area is accumulated
                % to take into account the total particle normalization in
                % the pair distribution function:
                ringarea = ringarea + pi*radius^2 - pi*inn^2;
            end

            % Calculate the number of particles inside the specific ring
            % area around the i-th particle:
            r = R(m,:);
            lessth = r<radius;
            greaterth = lessth.*r>inn;

            % Number of particles in the ring area:
            count = count+sum(greaterth);
        end

        % Matrix with the different radius, pair distribution function,
        % number of particles in each ring area and total ring area:
        g(i,1) = radius/diameter;
        g(i,2) = count/(ringarea*dens);
        g(i,3) = count;
        g(i,4) = ringarea;
    end
figure
hold on
plot(g(:,1),g(:,2));
title('Pair distribution function')
xlabel('r/d')
ylabel('g(r)')
hold off
end
```

B.1.8 Grain analysis-Main function: Triangulation and sizing of grains

```
function [grain_final,triangular_ordering] =  ...
grain_analysis(image_name,centers,ROI_factor,max_dev,conversion_factor)
%% Inputs:
% image_name is the filename of the analyzed image typed between single
% quotes,e.g,'example.tif'

% centers is the matrix with the X and Y coordinates of the particles.

% ROI_factor modifies the area of interest in the image to be analyzed.
```

```
% Allowed values between 0-100. (0 = 0% of the image, 100 = 100% of the
% image,normally around 80 or 90 to avoid large triangulation close to the
% edges)

% max_dev is the maximum deviation from the average triangle side and angle
% to consider a triangle well-ordered. Values between 0-100,(0 = 0%
% deviation and 100 = 100% deviation, normally around 10).

% conversion factor in nanometers/pixel is the relationship between pixels
% and the metric scale.

%% Outputs:
% A matrix of grains in which each row represents a grain with the number
% of triangles, the area occupied by each grain in pixels, the area occupied
%  by each grain in micrometers, the percentage rate of grain area occupied
% regarding the total ordered area and the percentage rate of grain area
% occupied regarding the total analyzed area

% the percentage rate of ordered area regarding the total area analyzed

%%
% Delaunay Triangulation based on the particle centers.
DT = delaunayTriangulation(centers);



% Get image dimensions to select the analysis area and discard points out
% of ROI
image = imread(image_name);
X = size(image, 2);
Y = size(image, 1);

% In each row of ConnectList there are 3 vertex IDs that define a triangle:
ConnectList = DT.ConnectivityList;

% Each row is the center coordinates of 1 particle (vertex):
centers = DT.Points;

% Create sides and angles to hold the 3 side lengths and the 3 angles of
% each triangle respectively. The i-th row of sides and angles is the i-th
% triangle:
sides = zeros(size(ConnectList));
angles = zeros(size(ConnectList));

% side_sum is the total sum of all triangle sides in the ROI and count the
% total number of triangle sides:
side_sum = 0;
count = 0;

% Total area occupied by all triangles and total area occupied by
% well-ordered triangles:
total_area = 0;
ordered_area = 0;

% Matrix of two vertices per row represented by coordinates X and Y whose
% distance has already been calculated:
vert_count = [0 0 0 0];

% Selection of allowed triangles within the region of interest:
```

```
for i = 1:length(ConnectList);

    % State variable changes if two points in the i-th triangle are
    % not within the allowed square ROI:
    state = [0, 0, 0];

    % Define the vertices (X,Y) of the triangle:
    a = centers(ConnectList(i,1),:);
    b = centers(ConnectList(i,2),:);
    c = centers(ConnectList(i,3),:);

    % Calculate the distance between two vertices by calling euc_distance.m:
    side1 = euc_distance(a, b);
    side2 = euc_distance(a, c);
    side3 = euc_distance(b, c);

    % if two vertices of the triangle are out of the limits of ROI, (by
    % calling within_ROI.m),state variable changes to 1:
    if within_ROI(X, Y,ROI_factor,a) == 1 &&...
       within_ROI(X, Y,ROI_factor,b)  == 1;
        state(1) = 1;
    end
    if within_ROI(X, Y,ROI_factor,a) == 1 &&...
       within_ROI(X, Y,ROI_factor,c) == 1;
        state(2) = 1;
    end
    if within_ROI(X, Y,ROI_factor,b) == 1 &&...
       within_ROI(X, Y,ROI_factor,c) == 1;
        state(3) = 1;
    end
    if state == [0, 0, 0];

        % Add the i-th allowed triangle defined by the sides to the sides'
        % matrix:
        sides(i, :) =[side1,side2,side3];

        % All triangle sides will be successively added in side_sum if and
        % only if the pair of vertices that define the side has not been
        % counted before and therefore they are not stored in vert_count
        % vector:

        if ismember([a b], vert_count, 'rows') == 0 ...
                && ismember([b a], vert_count, 'rows') == 0;
            side_sum = side_sum + side1;
            vert_count = [vert_count; a b];
            count = count + 1;
        end
        if ismember([a c], vert_count, 'rows') == 0 ...
                && ismember([c a], vert_count, 'rows') == 0;
            side_sum = side_sum + side2;
            vert_count = [vert_count; a c];
            count = count + 1;
        end
        if ismember([b c], vert_count, 'rows') == 0 ...
                && ismember([c b], vert_count, 'rows') == 0;
            side_sum = side_sum + side3;
            vert_count = [vert_count; b c];
            count = count + 1;
        end
```

```
        % Calculate the area of the allowed triangle by calling
        % triangle_area.m:
        total_area = total_area + triangle_area(side1, ...
            side2, side3);

        % Calculate the average side in pixels and nanometers from all the
        % allowed triangles:
        average_side = side_sum/count;

        % Determine the angles of the allowed triangles by calling
        % two_point_vector.m and vector_angle.m to be allocated in the
        % matrix angles where i-th row corresponds with the 3 angles of the
        % i-th triangle:

        % Angle A:
        AB = two_point_vector(a, b);
        AC = two_point_vector(a, c);
        angles(i,1) = [vector_angle(AC, AB, side1, side2)];

        % Angle B:
        BC = two_point_vector(b, c);
        BA = two_point_vector(b, a);
        angles(i,2) = [vector_angle(BC, BA, side3, side1)];

        % Angle C:
        CA = two_point_vector(c, a);
        CB = two_point_vector(c, b);
        angles(i,3) = [vector_angle(CA, CB, side2, side3)];

    % If two vertices of a triangle are out of the ROI, the triangle is
    % not allowed and eliminated by overwriting a zeros row on the vertex
    % IDs of the i-th triangle. A zeros row is also introduced in sides and
    % angles matrices to maintain the procedure integrity:
    else
        ConnectList(i,:) = [0 0 0];
        sides(i,:) = [0 0 0];
        angles(i,:) = [0 0 0];
    end
end

% Create a list to remove the zeros rows:
remove = [];
for i = 1:length(ConnectList);
    if ConnectList(i,:) == [0 0 0];
        remove = [remove, i];
    end
end

% Remove disallowed triangles from ConnectList, sides and angles matrices:
real_ConnectList = removerows(ConnectList, remove);
real_sides = removerows(sides, remove);
real_angles = removerows(angles, remove);

%% All triangle sides are added to the side_list list. The side deviation in
% percentage is calculated over the average side length and stored in the
% matrix side_dev where each row represents a triangle with the 3 side
% deviations.The triangle_sum_dev_list is a list with the total accumulated
% deviation of each triangle in percentage:
side_list = [];
side_dev = zeros(size(real_sides));
```

```
triangle_sum_dev_list = [];

for i = 1:length(real_sides);
    triangle_sum_dev = 0;
    for j = 1:3;
        side_list = [side_list, real_sides(i, j)];
        side_dev(i, j) = (1/(3*average_side))...
                        *abs((real_sides(i, j)-average_side))*100;
        triangle_sum_dev = triangle_sum_dev + side_dev(i, j);
    end
    triangle_sum_dev_list = [triangle_sum_dev_list; triangle_sum_dev];
end

% real_sides is a matrix in which each row represents 1 triangle with
% the 3 sides, the 3 side deviations and the total accumulated deviation:
real_sides = [real_sides, side_dev, triangle_sum_dev_list];

%% All triangle angles are added to the ang_list list. The angular deviation
% in percentage is calculated over the deviation from 60 degrees and stored
% in the matrix ang_dev where each row represents a triangle with the 3
% angular deviations. The ang_sum_dev_list is a list with the total
% accumulated deviation of each triangle in percentage:
ang_list = [];
ang_dev = zeros(size(real_angles));
ang_sum_dev_list = [];

for i = 1:length(real_sides);
    ang_sum_dev = 0;
    for j = 1:3;
        ang_list = [ang_list, real_angles(i, j);];
        ang_dev(i, j) = ((1/180)*abs(real_angles(i, j) - (60))*100);
        ang_sum_dev = ang_sum_dev + ang_dev(i, j);
    end
    ang_sum_dev_list = [ang_sum_dev_list; ang_sum_dev];
end

% real_angles is a matrix in which each row represents 1 triangle with
% the 3 angles, the 3 angular deviations from 60º and the total accumulated
% angular deviation:
real_angles = [real_angles, ang_dev, ang_sum_dev_list];

grains=[];
boundaries=[];
for i = 1:length(real_ConnectList);

    % Define the vertices of triangle:
    a = centers(real_ConnectList(i,1),:);
    b = centers(real_ConnectList(i,2),:);
    c = centers(real_ConnectList(i,3),:);

    % Triangles with both total angular deviation and total side deviation
    % less than the max_dev are stored in the matrix grains and the ordered
    % area calculated by calling triangle_area.m
    % Each row of grains defines a triangle by the three vertices. The first
    % two columns are the coordinates of the first vertex, the second and
    % third columns the coordinates of the second vertex and the last two
    % columns the last vertex of the triangle:
    if real_angles(i, 7) < max_dev && real_sides(i, 7) < max_dev;
        grains =[grains;a,b,c];
```

```
        ordered_area = ordered_area + triangle_area(real_sides(i, 1), ...
            real_sides(i, 2), real_sides(i, 3));

    % Triangles no matching the deviation criteria are stored in the matrix
    % boundaries:
    else
        boundaries =[boundaries;a,b,c];
    end
end
% Sort and plot the ordered triangles in different grains  by calling
% sorting_analysis.m:

grain_final = sorting_analysis(grains,image_name,...
                               conversion_factor,total_area);


% Calculate the triangular degree of order (total area occupied by the
% ordered triangles divided by the total area occupied by all the triangles):
triangular_ordering = ordered_area/total_area*100;
end
```

B.1.9 Sorting analysis: Classifies triangles in different grains

```
function [grain_final] = sorting_analysis(grains,image_name,...
                        conversion_factor,total_area)
figure
imshow(image_name);
hold on
title('All grains')
% Transparency parameter:
trans=0.55;

triaux=grains;
grain_list=[];
grain_final=[];
[row1,~]=size(triaux);

% Total number of ordered triangles:
triang_total=row1;

% Triangles are stored in different grains:
while row1~=0

    % Select the first triangle from triaux, add it to grain_list and delete
    % it in triaux:
    [row2,~]=size(grain_list);
    if row2==0
        ver1 = triaux(1,1:2);
        ver2 = triaux(1,3:4);
        ver3 = triaux(1,5:6);
        grain_list=[ver1 ver2 ver3];
        triaux=removerows(triaux,1);
        listcount=1;
    end

    % The grain growth proceeds if the next triangle analyzed in triaux
```

```
 % shares one side with the triangle selected from grain_list:
     ver1 = grain_list(listcount,1:2);
     ver2 = grain_list(listcount,3:4);
     ver3 = grain_list(listcount,5:6);
     e=0;
     remove=[];
     [row3,~]= size(triaux);
     for j=1:row3

         veraux1 = triaux(j,1:2);
         veraux2 = triaux(j,3:4);
         veraux3 = triaux(j,5:6);

         iden=0;
         if ver1 == veraux1 | ver1 == veraux2 | ver1 == veraux3
             iden=iden+1;
         end
         if ver2 == veraux1 | ver2 == veraux2 | ver2 == veraux3
             iden=iden+1;
         end
         if ver3 == veraux1 | ver3 == veraux2 | ver3 == veraux3
             iden=iden+1;
         end

         % if the triangle analyzed shares one side with the    triangle
         % from grain_list, the triangle is added to grain_list and
         % deleted from triaux:
         if iden ==2
             grain_list=[grain_list; veraux1,veraux2,veraux3];
             remove=[remove,j];
             e=e+1;
         end

         if e==3
            break
         end
     end
     listcount=listcount+1
     triaux=removerows(triaux,remove);
     [row1,~]=size(triaux);
     [row4,~]=size(grain_list);

% The algorithm continues selecting one by one the next triangles stored
% in grain_list, comparing them with the remaining triangles in triaux
% and adding more triangles to grain_list until there are no more
% triangles fulfilling the criteria in the i-th grain.
 if listcount > row4 | row1==0
     grain_area=0;

     % Only grains with at least 6 triangles are accepted as true grains:
     if row4>5;
         map=rand(1,3);

         for i=1:row4
          a = grain_list(i,1:2);
          b = grain_list(i,3:4);
          c = grain_list(i,5:6);
          side1 = euc_distance(a, b);
          side2 = euc_distance(a, c);
          side3 = euc_distance(b, c);
```

```
                %Area occupied by the whole grain:
                grain_area = grain_area + triangle_area(side1,side2, side3);
                % Triangles are filled with different colors depending on the
                % grain that they belong to:

                h = fill([a(1) b(1) c(1)], [a(2), b(2), c(2)], map);
                alpha(h, trans);
               end
               grain_area_um = grain_area*(conversion_factor/1000)^2;
               % Each row of grain_final represents one grain:
               grain_final = [grain_final; row4, grain_area,...
               grain_area_um,(row4/triang_total*100),grain_area/total_area*100];

           end
           grain_list=[];

       end
       % The algorithm continues looking for more grains until there is no more
       % triangles in triaux.
   end
   hold off

   figure
   hold on
   list=sort(grain_final(:,1),'descend');
   bar(list)
   title(' Distribution of grains')
   xlabel('Grain number')
   ylabel('Triangles')
   hold off
   figure
   set(gca,'visible','off')
   hold on
   pie(list)
   hold off
   end
```

B.1.10 grain-Main function: Generates a color-coded orientation map

```
function [alpha,transaa] = grain(image_name,cutoffdist)

% The following code computes the different grains present in a monolayer
% by calculating the relative orientation of individual nanoparticles
% regarding its coordination number. A color-coded orientation map is
% generated.

%% Inputs:
% image_name is the filename of the analyzed image typed between single
% quotes,e.g,'example.tif'. The image is a binary black-and-white image in
% which black color represents the particles and white color the background

% cutoffdist is the radius (in pixels) that from the central particle
% defines a circular region where the nearest neighbors are found and the
% angles around calculated. Usually, the radius is the minimum distance
% between the first and the second peak in the pair distribution
% function. In our case ~20.

%% Outputs:
```

```
% A matrix of angles in which each row represents one particle and the
% columns the nearest neighbors defined by the angles individually formed
% with the surrounded particle.

% A matrix of angles with the final averaged relative particle orientation
% of each particle



%% Determining coordinates of all particles
original = imread(image_name);
comporiginal = imcomplement(original);

% Label distinctively the pixels belonging to each particle:
L = bwlabel(comporiginal);

% Get centers and radii of the particles:
stats = regionprops(L , 'Centroid');
centroids = cat(1 , stats.Centroid);
xcoords(: , 1) = centroids (: , 1);
ycoords(: , 1) = centroids (: , 2);

% t is the total number of particles
t = size(xcoords,1);
alpha = zeros(t,6);

% Select the particles that fulfill the condition around each central
% particle and store in alpha matrix the angles calculated from the allowed
% neighbors with the central particle:

for c=1:t
    jamz = 1;
    for i=1:t
        if ((((xcoords(i,1)-xcoords(c,1))^2+(ycoords(i,1)-ycoords(c,1)...
        )^2)^.5) >0) && ((((xcoords(i,1)-xcoords(c,1))^2+...
        (ycoords(i,1)-ycoords(c,1))^2)^.5) <= cutoffdist)

        alpha (c,jamz) = (180/pi) * (atan ((ycoords(i,1)-...
        ycoords(c,1))/ (xcoords(i,1)- xcoords(c,1))));
        jamz = jamz + 1;
        end
    end
end

jj = size (alpha, 2);

% Normalize relative angles into a 60 degree interval (-30º-30º)in the
% matrix alphap:
alphap = zeros (t,jj);
for c=1:t
    for i=1:jj
        if alpha (c,i) > -30 && alpha (c,i) <= 30;
        alphap (c,i) = alpha (c,i);
        elseif alpha (c,i) > 30 && alpha (c,i) <= 90;
        alphap (c,i) = alpha (c,i) - 60;
        elseif alpha (c,i) < -30 && alpha (c,i) >= -90;
        alphap (c,i) = alpha (c,i) + 60;
        end
    end
```

```
end

% Find the row and column indices of all zero values in alphap:
[row0,col0] = find(alphap == 0);

% Arrange rows in order from the lowest to the highest row index where one
% or more zeros are present:
row00 = unique (row0);

% column vector that provides the number of zeros that exists in each row
% starting with the lowest row index that contains zero(s) to the highest
% row index:
counted=hist(row0(:),row00)';

% Total number of rows that contains zero(s).
teto = size (row00,1);

% Find the row and column indices of all nonzero values in alphap:
[rows,cols] = find(alphap ~= 0);

% Total number of nonzero angles in alphap.
dfd = size(rows,1);

% Create variables same length as the number of particles. The i-th row of
% totalangle will be the addition of all the angles surrounding the i-th
% particle. The i-th row of cuountz will count the number of angles added in
% the i-th row of totalangle:
totalangle=zeros(t,1);
countz=zeros(t,1);

% Calculate the average orientation of the i-th particle by adding all the
% nonzero angles kept in the i-th row and dividing by the number of angles
% added:
for j = 1:t
    for i=1:dfd
        if rows(i,1) == j;
        totalangle(j,1) = alphap(rows(i,1), cols(i,1)) + ...
        totalangle(j,1);
        countz(j,1) = countz(j,1) +1;
        end
    end
end

% Create a variable to hold the average angle:
averageangle = zeros(t,1);

for j = 1:t
averageangle(j,1) = totalangle(j,1) / countz(j,1);
end

% Round the averageangle values to nearest integer:
raverageangle = round(averageangle);

% In case of any value of raverageangle is a NaN, ind will be an array
% containing the linear indices corresponding to the NaN position
% for replacing it with a zero value:
ind = find(isnan(raverageangle));
raverageangle(ind)=0;
```

```
% 30 is added to all the averaged angles stored in raverageangle to set an
% angle interval between 0º-60º. 1 is finally added to get the final
% angle interval between 1º-61º so each angle coincides with a proper
% color in the colormap c:

for i=1:t
transaa(i,1) = raverageangle(i,1) + 31 ;
end

c=colormap(jet(61));

% RGB = label2rgb(L) converts a label matrix, L, returned by bwlabel into
% an RGB color image for the purpose of visualizing the labeled regions.
% [0 0 0] value for zero-labeled elements (black color for background)
% jet(1) defines the colormap map to be used in the RGB image.
% Shuffle assigns colormap colors to label matrix regions without
% numerical order:

RGB = label2rgb(L == 1, jet(1), [0 0 0], 'shuffle');
for i = 1:t
    % for all the pixels labeled i belonging to the i particle ,label2rgb
    % assigns the value stored in transaa(i),a number between 1 and 61, to
    % the color of the particle by passing the coordinates of that number
    % to the colormap c, c(transaa(i),:)

RGB =RGB + label2rgb(L == i, c(transaa(i),:), [0 0 0], 'shuffle');
end

%teto was the total number of rows with zero(s) in their columns
for i = 1:teto
    % if the subtraction between the number of columns in alpha(jj) and the
    % number of zeros in the i-th row is not equal to 6, the particle is
    % considered a boundary and colored in white ([1 1 1]):
    if jj - counted(i) ~= 6
    RGB =RGB + label2rgb(L == row00(i), [1 1 1], [0 0 0], 'shuffle');
    end
end
imshow (RGB);
colorbar;
caxis([0 60]);

end
```